

ABSTRACT

Title of Dissertation: DESIGN AND IMPLEMENTATION OF
MICROFLUIDIC SYSTEMS FOR
BACTERIAL BIOFILM MONITORING AND
MANIPULATION

Mariana Tsacoumis Meyer, Doctor of
Philosophy, 2014

Directed By: Professor Reza Ghodssi, Department of
Electrical and Computer Engineering, Institute
for Systems Research

Bacterial biofilms – pathogenic matrices formed through bacterial communication and subsequent extracellular matrix secretion – characterize the majority of clinical bacterial infections. Biofilms exhibit increased resistance to conventional antibiotics, necessitating development of alternative treatments. Standard microbiological methods for studying biofilms often rely on *in vitro* systems with involved instrumentation for biofilm quantification, or destroy the biofilm in the process of characterization. Additionally, biofilm formation is sensitive to many growth parameters, and can exhibit a large degree of variability between repeated experiments. This dissertation presents the development of systems designed to address these challenges through integration of

continuous biofilm monitoring in a microfluidic platform, and through creation of a microfluidic platform for multiple assays performed on one biofilm formed in a single channel. The microsystems developed in this work provide building blocks for developing controlled, high throughput testbeds for development and evaluation of drugs targeting bacterial biofilms.

The first platform developed relied on optical density monitoring as a means for evaluating biofilm formation. This method was noninvasive, as it used an external light source and array of photodiodes to evaluate biofilms by the amount of light transmitted through the microfluidic channel where they were grown. The optical density biofilm measurement method and microfluidic platform were used to evaluate the dependence of biofilm formation on quorum sensing, an autoinducer-mediated intercellular communication process. This system was also used in the first demonstration of biofilm inhibition and reduction by two different autoinducer-2 analogs.

The second microfluidic system developed addressed the challenge of variability in biofilm formation. Biofilms formed in a single microfluidic channel were partitioned by hydraulically actuated valves into three separate segments, which were then treated as representatives of the original biofilm in further experiments. A novel photoresist passivation process was developed in order to create the multi-depth channels needed to accommodate both valve actuation and biofilm formation. Biofilms grown in the device were uniform throughout, providing reliable experimental controls within the system. Biofilm partitioning was demonstrated by exposing three segments of one biofilm to varying detergent concentrations.

**DESIGN AND IMPLEMENTATION OF MICROFLUIDIC SYSTEMS FOR
BACTERIAL BIOFILM MONITORING AND MANIPULATION**

By

Mariana Tsacoumis Meyer

Dissertation submitted to the Faculty of the Graduate School of the
University of Maryland, College Park, in partial fulfillment
of the requirements for the degree of
Doctor of Philosophy
2014

Advisory Committee:

Professor Reza Ghodssi, Chair

Professor William Bentley

Professor Keith Herold

Professor Herman Sintim

Professor Ian White

© Copyright by
Mariana Tsacoumis Meyer
2014

Dedication

To my unconditionally loving husband Harry, whose mellowness never ceases to amaze
me.

Acknowledgments

First, I would like to acknowledge my advisor Prof. Reza Ghodssi for his guidance and support throughout this work. I would like to thank my committee members, Prof. William Bentley, Prof. Keith Herold, Prof. Herman Sintim, and Prof. Ian White. Additionally, none of this research would have been possible without the funding provided by the Robert W. Deutsch Foundation and the National Science Foundation.

I have been fortunate in being able to work with many supportive collaborators. I especially thank Dr. Rohan Fernandes, Dr. Varnika Roy, Dr. Stephan Koev, and Dr. Peter Dykstra for their assistance and guidance from the beginning of my Ph.D. work. I would also like to thank all the past and present members of the MEMS Sensors and Actuators Laboratory for support in many ways that have shaped who I am today. I especially thank Young Wook Kim, Thomas Winkler, Sowmya Subramanian, and Dr. Markus Gnerlich, who all not only reviewed this manuscript but also supported this work through thoughtful discussion and guidance. I additionally thank all my collaborators in the Maryland Biochip Collaborative for fostering an atmosphere of interdisciplinary exploration. I especially extend my thanks to Prof. Bentley and the students in his laboratory, where I have been generously welcomed from Day 1. I greatly appreciate the support of the Maryland NanoCenter and its FabLab, in addition to the support provided by Amy Beaven and the University of Maryland Imaging Core Facility.

Finally I would like to thank my parents, my sister Christina, and of course my husband Harry, for supporting me through literal blood, sweat, and tears.

Table of Contents

Dedication	ii
Acknowledgments	iii
Table of Contents	iv
List of Tables	vii
List of Figures	viii
1 Introduction	1
1.1 Background and Motivation	1
1.2 Summary of Accomplishments	2
1.2.1 Development of optical density monitoring of biofilms formed in microfluidics	2
1.2.2 Use of microfluidics and optical monitoring to evaluate quorum sensing inhibitors	3
1.2.3 Development of a valved microfluidic system for biofilm sectioning	4
1.3 Literature Review	5
1.3.1 Bacterial Biofilm Characteristics	5
1.3.2 Alternative Biofilm Treatments	15
1.3.3 Macroscale Evaluation of Biofilms	18
1.3.4 Microfluidics	25
1.3.5 Microsystems for Biofilm Growth and Characterization	27
1.4 Structure of Dissertation	30
2 Monitoring of Biofilm Formation in Microfluidics via Optical Density	31
2.1 First Generation Device	31
2.1.1 Platform Overview	32
2.1.2 Platform Fabrication, Assembly, and Interfacing	34
2.1.3 Experimental Methods	39
2.1.4 Results and Discussion	42
2.1.5 Conclusion	58
2.2 Second Generation Device	59
2.2.1 Platform Design	60
2.2.2 Results and Discussion	62
2.2.3 Conclusion	64
2.3 Chapter Summary	64
3 Evaluating Effects of Quorum Sensing Inhibitors on Biofilm Formation	66
3.1 Evaluation of Quorum Sensing Inhibitors using Microfluidic Platform with Optical Monitoring	66

3.1.1	Methods.....	67
3.1.2	Results and Discussion	72
3.1.3	Conclusion	84
3.2	Effect of Quorum Sensing Inhibitors on Persister Cells.....	86
3.2.1	Methods.....	86
3.2.2	Results and Discussion	88
3.3	Chapter Summary	90
4	Development of Multi-depth Microfluidics for Controlled Biofilm Studies.....	92
4.1	Design	92
4.1.1	Overview.....	92
4.1.2	Design Consideration: Channel Depth and Shear Stress on Biofilms	95
4.1.3	Design Considerations: Depletion of Oxygen and Nutrients Along Channel	97
4.2	Fabrication	104
4.2.1	Overview.....	104
4.2.2	Fluidic Mold Fabrication	106
4.2.3	Hydraulic Control Mold Fabrication	114
4.2.4	PDMS Layer Fabrication and Bonding.....	115
4.3	Device Preparation and Testing.....	119
4.3.1	Device Preparation.....	119
4.3.2	Operation: Biofilm Growth.....	120
4.3.3	Operation: Biofilm Segmentation	120
4.3.4	Staining, Confocal Microscopy, Image Analysis	121
4.4	Results and Discussion	121
4.4.1	Fabrication of Multiple Channel Profiles	121
4.4.2	Valve Functionality.....	123
4.4.3	Biofilm Uniformity	126
4.4.4	Biofilm Segmentation	129
4.5	Chapter Summary	133
5	Conclusion	135
5.1	Summary	135
5.2	Future Work	137
5.3	Conclusion	140
Appendix A:	Masks Used.....	142
Mask #1.....		142

Mask #2.....	143
Mask #3.....	144
Mask #4.....	145
Mask #5.....	146
Appendix B: Circuit Diagrams	147
Photodiode Measurement.....	147
LED Circuit.....	148
Appendix C: Matlab Code	149
Basic OD Measurement	149
Data Fitting	152
6 References.....	154

List of Tables

Table 1.1. Summary of highlights from published work utilizing microfluidic platforms for biofilm studies.	28
Table 2.1. Table of <i>p</i> -values obtained through Student's <i>t</i> -test for comparison of optical density change magnitude and for comparison of percent difference in optical density change between <i>E. coli</i> biofilm groups.	50
Table 2.2. Table of <i>p</i> -values obtained through Student's <i>t</i> -test for comparison of thickness between <i>E. coli</i> biofilm groups.	52
Table 4.1. Parameters used for COMSOL simulation of oxygen transport.	102
Table 4.2. Process flow of the PDMS molding and assembly process.	106
Table 4.3. Parameters varied in AZ 9260 hardbake characterization, including temperature, time, and whether the chip was covered during the bake. Corresponding photographs were obtained after the hardbake and after immersing the chip in SU-8 developer for 5 minutes. The red box highlights parameters used in further process development.	109
Table 4.4. Table of processing steps and parameters used for AZ 9260 lithography, rounding, and hardbaking.	110
Table 4.5. UV-ozone curing parameters and corresponding images of AZ 9260 structures after the hardbake (before UV-ozone exposure) and after testing stability by exposure to SU-8 developer. UV-ozone exposure was performed in multiple steps to prevent overheating and bubbling of the resist; chips were exposed to 1 minute of UV-ozone, then allowed to cool for 1 minute.	111
Table 4.6. Chart depicting different squares on different test chips after deposition of the Al ₂ O ₃ layer, and after immersing the chip in SU-8 developer for the time interval specified in the top row. (a) Chips with 45 nm of Al ₂ O ₃ passivation; (b) Chips with 95 nm of Al ₂ O ₃ passivation.	112
Table 4.7. Table of processing steps and parameters used for KMPR 1050 lithography on top of patterned and passivated AZ9260.	113
Table 4.8. Table of processing steps and parameters used for KMPR 1050 lithography to create hydraulic control channels.	115
Table 4.9. Process flow of the final PDMS molding and assembly process.	118
Table 4.10. Summary of treatments applied to biofilm sections in each device, describing how positioning of treatments was varied between the two devices tested. Section I denotes the section closest to the inlet, and III denotes the section closest to the outlet.	131

List of Figures

Figure 1.1. Diagram of the biofilm growth cycle, from bacterial adhesion to the substrate, formation of microcolonies, development of a mature structure, and detachment. Reproduced from [18].	6
Figure 1.2. Diagram representing a common mathematical biofilm model accounting for interrelated processes in a biofilm reactor. Reproduced from [33].	9
Figure 1.3. Illustration of antibiotic resistance mechanisms in biofilms, indicating several contributors that individually reduce the impact of antibiotics on a biofilm. Reproduced from [4].	10
Figure 1.4. Schematic of behaviors switched on by QS and accumulation of autoinducer molecules in the extracellular environment. Reproduced from [59].	13
Figure 1.5. Illustration of aspects of bacterial biofilm formation and growth influenced by QS. Reproduced from [64].	14
Figure 1.6. Schematic of Modified Robbins Device, indicating fluidic connections and plugs upon which biofilms grow. Reproduced from [11].	19
Figure 1.7. Cross-sectional diagram (top) and top view (bottom) of a Calgary Biofilm Device. The diagram illustrates the space allowance for growth media flow between the pegs and the bottom of the device. As seen in top-down view, the pegs are arrayed in a 12x8 array compatible with a 96-well plate. Reproduced from [8].	20
Figure 1.8. Images of a <i>Bacillus subtilis</i> biofilm obtained using A) Confocal microscopy C) Field emission SEM, similar to standard SEM apart from the use of a field emitter instead of a thermionic emitter in order to minimize distortion and obtain higher resolution B) ESEM performed at a chamber pressure of 4 Torr D) ESEM performed at 5 Torr. Reproduced from [96].	23
Figure 1.9. Schematic of biofilm flow cell reactor used by Bakke et al. Biofilms were formed in parallel rectangular tubes (1.0x3.0x300 mm), formed by inserting a water-filled capillary into a larger square tube in order to create a large surface area for biofilm formation. Optical density at 420 nm was measured between points A and D using a fiber optic probe. Reproduced from [14].	25
Figure 2.1. Schematic of PDMS microfluidic channel integrated with optical source and detector for optical density measurement of biofilms within the channel. The LED provided incoherent light, which scatters off the surface of and within the biofilm. Light that is transmitted through the pinhole in the chrome represents a combination of light that does not interact with the biofilm and light scattered from the biofilm. Overall, less light sensed by the photodiode implies a greater amount of biofilm either impeding transmission or scattering light away from the pinhole. Note: not to scale.	33
Figure 2.2. Schematic of microfluidic flow cell in which biofilms were formed. The width, length, and depth of the straight microfluidic channel used in these studies were 500 μm , 2 cm, and 100 μm , respectively, A syringe pump operating in withdrawal mode provided flow throughout the channel of suspended bacteria, growth media, or fluorescent dye from a reservoir.	36

Figure 2.3. a) Photograph of assembled microfluidic device with fluidic connections b) Photograph of microfluidic device (inset) integrated with fluidic components, and positioned over photodiodes and under LEDs.	36
Figure 2.4. Schematic of multiplexer integration with photodiode measurement. A digital counter generated by LabVIEW controls the multiplexer state, and determines which photodiode signal is reflected in the multiplexer output. Both the multiplexer output and the state of the counter over time are exported to MATLAB, where the photodiode outputs are separated.	38
Figure 2.5. Measured changes in optical density of known bacterial suspensions using microfluidic platform with photodiodes. The photodiode output is linearly correlated to turbidity measured with a spectrophotometer.	42
Figure 2.6. Raw optical density change measurements corresponding to the output of the two photodiodes positioned under one microfluidic channel. ‘Window 1’ is closest to the channel inlet. Data correspond to two separate <i>E. coli</i> W3110 experiments. a) Outputs differ along the length of the channel, as seen difference in photodiode outputs between 5 and 12 hours; the greatest difference between outputs is 31%. b) Outputs show almost identical behavior with less than a 10% difference between measurement locations.	44
Figure 2.7. Data corresponding to <i>E. coli</i> W3110 and MDAI2 biofilms formed in two microfluidic platforms. a) Raw optical density change measurements, illustrating unpredictable “spikes” in observed optical density b) Data from (a) smoothed using quadratic fits (Appendix C).	45
Figure 2.8. Rinsing of <i>E. coli</i> W3110 and MDAI2 biofilms measured by the change in optical density. Data indicate the role of quorum sensing in physical robustness of biofilms.	46
Figure 2.9. Compiled data for the change from baseline optical density for each type of <i>E. coli</i> biofilm formed. $n = 3$ for each data point, presented as the average of all trials. Error bars correspond to one standard deviation of the trials.	49
Figure 2.10. Compiled data for the percent difference from wild-type (W3110) biofilms for MDAI2 biofilms (blue circles) and for MDAI2 biofilms grown with AI-2 (red squares). Error bars represent one standard deviation of the averaged data.	50
Figure 2.11. Compiled morphological data, including a) average thickness, and b) nondimensional roughness coefficient, for each type of biofilm formed. $n = 3$ for each data point, presented as the average of all trials. Error bars represent one standard deviation of the averaged data.	52
Figure 2.12. Least-squares regression fit of biofilm thickness (t) versus change in optical density (OD), compiled for all biofilms at all timepoints observed. $R^2 = 0.90198$	57
Figure 2.13. Schematic of the CCD-based microfluidic biofilm observation platform. A printed circuit board (PCB) served as a foundation for circuitry and electrical connections. An array of microfluidic channels patterned in PDMS was placed on top of a transparent substrate and aligned to the underlying CCD array. The platform depicted here also included electrodes patterned on the transparent substrate for applying an electric field to biofilms during growth. Modified from [133].	61

Figure 2.14. Schematic of experimental setup for CCD-based microfluidic biofilm observation platform. The CCD array, microfluidic channel, and samples to be introduced into the channel were contained in a 37 °C incubator. A syringe pump operating in withdrawal mode created sample flow in the microfluidic channels. External power supplies and function generators enabled actuation of the CCD sensors, while a DAQ card and PC were used to obtain and analyze optical density measurements. Reproduced from [126]..... 61

Figure 2.15. Demonstration of spatiotemporal optical density monitoring in the CCD-based microfluidic biofilm observation platform using flow of optically dense droplets in transparent mineral oil. (a) Average change in optical density within one microfluidic chamber of the CCD-based biofilm measurement platform during droplet flow. (b) Spatiotemporal detection of droplet flow within the same microfluidic channel. Reproduced from [126]..... 63

Figure 2.16. Surface reconstruction of biofilm surface morphology showing (a) stationary biofilm and (b) biofilm drifting through the channel with time. The surface reconstruction as created using the spatiotemporal data from optical density measurement using the CCD-based biofilm measurement system. This particular plot is from a biofilm sample treated with an electric field. Reproduced from [126]..... 64

Figure 3.1. Analysis of optical density curves and fits using *E. coli* biofilm growth data (a) Normalized change in optical density; raw data (dotted line) was normalized with the change in optical density at 48 hours set to be 1. The curve was fit (solid line) using a Churchill model. (b) Adjusted curve fit, using a fit to data averaged every 6 hours (squares). The curves have also been adjusted to reflect a zero change in optical density at the beginning of growth. 72

Figure 3.2. Analysis of 48 hour *E. coli* biofilm thickness and architecture in response to isobutyl-DPD. a) Thickness and biomass of biofilm analyzed by COMSTAT (average of four different points). b–d) Representative Imaris 3D surface reconstructions of the biofilm with b) LB only, c) LB+40 μM isobutyl-DPD, d) LB+100 μM isobutyl-DPD. Images were selected from locations with average thicknesses and biomasses closest to the average of all points analyzed. 73

Figure 3.3. Analysis of effect of combinatorial approach analog and gentamicin on preformed *E. coli* biofilm thickness and architecture. a) Thickness and biomass of biofilm analyzed by COMSTAT (average of five different points in the channel). b–e) Representative Imaris 3D surface reconstructions of the biofilm with b) LB only, c) LB+5 μg/mL gentamicin, d) LB+40 μM isobutyl-DPD+5 μg/mL gentamicin, e) LB+100 μM isobutyl-DPD+5 μg/mL gentamicin. Images were selected from locations with average thicknesses and biomasses closest to the average of all points analyzed. 76

Figure 3.4. Analysis of effect of combinatorial approach analog and gentamicin on preformed *P. aeruginosa* biofilm thickness and architecture. a) Thickness and biomass of biofilm analyzed by COMSTAT (average of five different points in the channel). b–e) Representative Imaris 3D surface reconstructions of the biofilm with b) LB only, c) LB+5 μg/mL gentamicin, d) LB+100 μM phenyl-DPD, e) LB+100 μM phenyl-DPD +5 μg/mL gentamicin. Images were selected from locations with average thicknesses and biomasses closest to the average of all points analyzed. 78

Figure 3.5. Comparison of Live/Dead percentages in confocal images presented in Figures 3.2-3.4, reflecting the effect of continuous *E. coli* biofilm exposure to isobutyl-DPD (Figure 3.2), and exposure of preformed *E. coli* (Figure 3.3) and *P. aeruginosa* (Figure 3.4) biofilms to gentamicin and isobutyl-DPD or phenyl-DPD. Each bar represents one imaged location within the channel. Results were expected to show a decrease in unviable cells with addition of DPD analogs, indicative of a weaker extracellular matrix; as shown, actual results obtained were inconclusive. 81

Figure 3.6. Analysis of effect of combinatorial approach on optical density and thickness using analog and gentamicin on *E. coli* (a, b) and *P. aeruginosa* (c, d) biofilms preformed for 48 hours. a) Normalized change in optical density of *E. coli* biofilms; raw data (dotted lines) were normalized with the change in optical density at 48 hours set to unity. Curves were fitted (solid lines) using a Churchill model [135]. b) Thickness and biomass of *E. coli* biofilm analyzed by COMSTAT (average of two points in the channel). c) Normalized change in optical density of *P. aeruginosa* biofilms; raw data (dotted lines) were normalized and fitted (solid lines) using a Churchill model. d) Thickness and biomass of *P. aeruginosa* biofilm analyzed by COMSTAT (average of two points in the channel)..... 83

Figure 3.7. Box-and-whiskers plot of the control group (LB) in Figure 3.6c, demonstrating the temporal variability observed through optical density monitoring. Each square represents the optical data averaged between two windows and averaged over 6 hour time windows centered at each point (endpoints are averaged over 3 hours). Middle horizontal lines represent the median, and top and bottom horizontal lines represent ± 1 standard deviation of the data. Minimum and maximum points within the data sets are denoted by an “x”..... 84

Figure 3.8. Results from persister cell formation experiments. In both (a) and (b), the first column was untreated, representing a control in which many colonies are expected; similarly, the third column was treated only with isobutyl-DPD, which does not cause cell death. The second column and fourth columns respectively represent generation of persister cells via treatment with a high concentration of antibiotic and the addition of analog to this treatment. Groups 1 and 2 are replicates. (a) Data from counting colonies formed after plating treated suspensions. (b) Data obtained via FACS..... 88

Figure 3.9. Data from Figure 3.8, where each bar is an average of Group 1 and Group 2 as presented in Figure 1. (a) and (b) correspond to the data from Figure 3.8a and 3.8b respectively. As the data are the average of two data points, standard deviations are not presented. 89

Figure 4.1. a) Schematic of device operation during biofilm growth, with side channels blocked by closed valves (solid black squares) b) Device operation during biofilm sectioning, with side channels open and central channel trisected by two closed valves c) Side-view schematic of open push-up valve integrated with two-depth channel d) Side-view schematic of closed push-up hydraulic valve with pressure applied to the liquid-filled control channel to close the valve. 94

Figure 4.2. Three-dimensional representation of the assembled platform in the biofilm growth configuration (corresponding to Figure 4.1a). Pressure applied to Control Channel #2 closes the corresponding valve and prevents flow into the side channel. The

valve regulated by an unpressurized Control Channel #1 remains open, allowing biofilm growth in the central channel where there is flow.	95
Figure 4.3. Conceptual model of oxygen transport in microfluidic biofilm reactor. This simplified model includes valve-less geometry and does not account for effects on changes in oxygen transport and reaction rates due to biofilm growth.	98
Figure 4.4. Detail of oxygen concentration within growth media near the channel inlet from steady state COMSOL simulation of oxygen transport in the microfluidic system. The simulation was based on the conceptual model of Figure 4.3 and used the parameters in Table 4.1.	103
Figure 4.5. Mask layout for PDMS molds. Pink channels denote the top, biofilm-containing layer, and green channels denote the bottom, hydraulic control layer. Valve locations are indicated by black squares at the intersections of the pink and green channels. Drawn to scale.	105
Figure 4.6. Photograph of PDMS molded with the 2-depth AZ 9260/KMPR mold. Brown squares of cracked AZ 9260, indicated by the arrow, delaminated off the wafer and became stuck in the channels in the PDMS. The AZ 9260 residues could not be removed from the PDMS without severely damaging the microfluidic channel.	107
Figure 4.7. Cross-sectional schematics and corresponding photographs of fluidic mold fabrication: a) patterning of AZ 9260 positive resist, b) resist rounding and hardbake, c) passivation with ALD Al ₂ O ₃ , and d) KMPR 1050 patterning.	114
Figure 4.8. a) Contact profilometry scan of mold at valve region, verifying the presence of the desired profiles. In the measured region, the rounded AZ 9260 section had a peak height of 36 μm, and the KMPR 1050 channels had a depth of approximately 97 μm. b) SEM image of multi-depth structure created from two photoresists. Note the large difference in aspect ratios minimizes the appearance of curvature in the shallow section. c) Photograph of multi-depth mold.	122
Figure 4.9. Photographs (left column) of the device taken at different stages over a several-hour testing period, and diagrams (right column) illustrating flow patterns and valve configurations, where solid black squares indicate closed valves. a) Filling the hydraulic control channels with red-dyed water, leaving the fluidic channels empty. b) Actuating one set of valves and creating flow through the center channel in the fluidic layer. c) Reversing valve orientation and rinsing out two of the three new channels with undyed DI water. d) Creating different flows in each of the three segmented channels.	125
Figure 4.10. Photographs of assembled devices with green water filling actuated control channels. a) Device in biofilm growth orientation, with side channels blocked by closed valves. Photograph corresponds to Figure 4.1a. b) Device in biofilm sectioning orientation, with side channels open and central channel sectioned by closed valves. Photograph corresponds to Figure 4.1b.	126
Figure 4.11. Surface reconstruction of confocal microscopy of 60-hour <i>E. coli</i> BL21 pGFP biofilm within the microfluidic channel. Bacteria showed only green fluorescence; red areas are residual red food coloring absorbed into PDMS or the air-colored water interface in the control channel. The red food coloring is visible due to its intrinsic low-level fluorescence. a) Top view b) Angled view from side, c) Schematic representation	

of confocal images in the context of the layered PDMS channels. Hydraulic control channel is depicted as completely filled with red-dyed water, whereas during confocal microscopy the water receded toward the open fluidic ports, leaving behind fluorescent residue. 127

Figure 4.12. a) Schematic of device operation during biofilm growth, with side channels blocked by closed valves. Confocal microscopy images were obtained at the center of each of the three sections indicated (I, II, and III) b) Average biofilm thicknesses measured at imaged locations in the three devices tested. Locations were positioned in the center of each section, with Section I closest to the inlet, and III closest to the outlet. Dashed lines indicate averaged thickness across imaged locations for each device. c-e) Surface rendered confocal microscopy images from Device 3, Sections c) I, d) II, and e) III. Thicknesses were 17.0, 15.6, and 16.2 μm respectively. 128

Figure 4.13. a) Schematic of device operation during biofilm segmentation, with the central channel trisected by two closed valves. Confocal microscopy images were obtained at the center of each of the three sections indicated (I, II, and III) b) Average biofilm thicknesses measured at the imaged locations in the two tested devices with different SDS exposure levels. c-e) Surface rendered confocal microscopy images of *E. coli* biofilms in Device 1 with c) no treatment (control) d) exposure to 0.1% SDS, and e) exposure to 0.2% SDS. Biofilm thicknesses were 24.9, 7.9, and 0.3 μm respectively. 131

Figure 5.1. Schematics of valved device for biofilm segmentation integrated with a diffusive gradient mixer for generating multiple concentrations of a solution, e.g. antibiotic or AI-2 analog, on-chip. a) Device configuration during biofilm growth, with side channels and gradient mixer blocked by closed valves (solid black squares) b) Device operation during biofilm sectioning and exposure of biofilm sections to different concentrations of drugs, with side channels open and central channel trisected by two closed valves. 139

1 Introduction

1.1 Background and Motivation

Bacterial biofilms characterize a large number of clinical infections. One estimate suggests that 65% of all bacterial infections involve a biofilm [1]. Biofilms impede phagocytosis as well as penetration of leukocytes into their structure [2, 3], reducing the efficacy of host immune mechanisms. Within biofilms, high rates of mutation and horizontal exchange of genetic material promote selection of antibiotic tolerance mechanisms [2, 4] – cells associated with a biofilm are 10-1000 times more resistant to antimicrobial agents than free-floating bacteria [5]. Unfortunately, biofilms occur in the majority of clinical infections, commonly forming on catheters, prosthetic joints, respiratory tract surfaces, and teeth [6].

While the detailed study of biofilms has existed for decades [7], much remains unknown. In the pursuit of understanding bacterial biofilms, a number of *in vitro* models have been developed not only for understanding biofilm biology, but also for evaluating biofilm response to environmental challenges such as exposure to antimicrobials [8-11]. However, just as each clinically observed infection is unique, biofilms grown *in vitro* also show variability within and between platforms [12, 13]. This variability precludes reliable comparison of biofilms under experimental conditions to biofilms under control conditions.

Standard microbiological methods for evaluating biofilms often rely on *in vitro* systems with involved biofilm quantification instrumentation, or destroy the biofilm itself during characterization. Therefore, there is a need to develop compact systems that can noninvasively quantify biofilm properties. Microfluidic sensing platforms are an ideal

solution for addressing the need for more rigorous study of physiologically relevant bacterial biofilms. Microfluidic systems provide several advantages including inexpensive fabrication, highly parallel throughput, and small size. While microfluidics are readily compatible with noninvasive, integrated sensing technologies, biofilms formed in microfluidics are still most commonly evaluated using external instrumentation such as confocal microscopy.

This dissertation presents the systematic development of microfluidic systems for biofilm applications. It is anticipated that the microfluidic biofilm model and testing methodology established in this dissertation will lay the foundation for on-chip development of clinically effective biofilm therapies.

1.2 Summary of Accomplishments

As described above, a number of tools exist for biofilm evaluation, each with its own set of advantages and disadvantages. This dissertation pursues the development of tailored microfluidics for biofilm applications. These microfluidic systems provide continuous feedback and a controllable microenvironment for highly parallel studies, and also address biofilm variability.

1.2.1 Development of optical density monitoring of biofilms formed in microfluidics

First, a microfluidic platform and methodology were developed for forming and observing bacterial biofilms in microfluidics. As indicated above, microscale flow systems are capable of providing a fluidic and chemical microenvironment that may be tailored to the application. In this work, a microfluidic channel serving as a biofilm reactor was integrated with external commercial off-the-shelf optical components to

provide continuous optical density measurements. While optical density had been used previously to monitor biofilms formed in a macroscale flow cell [14], it had never been used to evaluate biofilms formed in microfluidics prior to this work.

The microfluidic biofilm reactor and sensing technique were used to continuously and non-invasively observe the dependence of *Escherichia coli* biofilm formation on bacterial intercellular signaling, or quorum sensing. The effect of quorum sensing on biofilms was evaluated by comparing changes in optical density of biofilms formed by wild type *E. coli*, and biofilms formed by *E. coli* incapable of synthesizing native signaling molecules known as autoinducers. Additionally, the effect of adding a set concentration of autoinducer to autoinducer-null biofilms was investigated. As optical density is not a standard biofilm metric, results were confirmed by evaluating morphological properties of the biofilms using confocal microscopy. Statistical analysis was applied to assess the significance and repeatability of observed optical and morphological differences in the biofilms formed.

1.2.2 Use of microfluidics and optical monitoring to evaluate quorum sensing inhibitors

While the developed growth and measurement system described above in Section 1.2.1 was used to confirm the dependence of *E. coli* biofilm formation on bacterial communication, similar studies have been performed in other formats [15-17]. The second major accomplishment of this dissertation was the use of the microfluidic system for optical biofilm measurement to evaluate new autoinducer analogs that inhibit bacterial intercellular communication.

The microfluidic platform was used to show that these autoinducer analogs not only prevent biofilm formation by *E. coli* and *Pseudomonas aeruginosa*, but can aid in clearance of preexisting biofilms when applied with a traditional antibiotic. The capability of continuous optical density measurement confirmed that biofilm clearance was continuous and was initiated upon application of the treatment.

1.2.3 Development of a valved microfluidic system for biofilm sectioning

The microfluidic devices used in the above studies did provide for efficient biofilm testing by nature of the small volumes of autoinducer or autoinducer analog required for microscale biofilm studies. However, biofilm variability was still observed between experiments. For the purpose of drug development, control groups must produce an output with minimal variability to which the experimental groups can be compared. The third major accomplishment presented in this dissertation is the design, fabrication, and testing of a microfluidic device not only enabling concurrent studies on the same chip, but also allowing for multiple experiments to be performed on the same biofilm, eliminating variation between biofilms due to device-to-device or experiment-to-experiment variability.

The device created in this work uses hydraulically actuated valves incorporated in the microfluidic device. In realizing microchannels with multiple depths to accommodate valve actuation and biofilm growth, a novel mold fabrication technique was developed using sequentially patterned photoresist separated and passivated by conformal coatings using atomic layer deposition (ALD). The capabilities of the resulting platform were demonstrated through trisecting mature biofilms using the integrated valves and exposing the three segments to different treatments on the same platform.

1.3 Literature Review

The following section presents additional background information and a review of literature as applicable to this dissertation. First, a discussion of bacterial biofilms is presented in order to provide more detail as to their intrinsic properties, with a focus on factors contributing to the severity of biofilm-associated infections. While biofilms are formed by many species of bacteria, emphasis is placed on *E. coli* and *P. aeruginosa* biofilms throughout this discussion; due to my collaborators' experience with these clinically relevant species as well as the large body of research surrounding them, *E. coli* and *P. aeruginosa* were used throughout this research as models of biofilm formation. Second, alternative biofilm eradication methods that minimize the use of traditional antibiotics are reviewed. Next, traditional methods for studying biofilms and their response to antimicrobial treatments are discussed. The subsequent section reviews advantages presented by microfluidic systems and relevant microsystems technologies. Finally, a summary of biofilm studies performed in microfluidics is presented in order to emphasize the novelty of the main accomplishments presented in this dissertation.

1.3.1 Bacterial Biofilm Characteristics

1.3.1.1 Biofilm Formation and Growth

Biofilm formation is initiated by attachment of planktonic bacteria to surfaces in their environment. The adhesion, initially tenuous, is strengthened by genetic pathways promoting the secretion of an extracellular matrix, which encourages both adhesion to the substrate as well as cohesion between cells to form microcolonies, as shown in Figure 1.1. The matrix stabilizes the developing biofilm and allows for proliferation of bacteria within the biofilm structure, while at the same time protecting the biofilm from attack by

host defense mechanisms. Cells or entire fragments of a mature biofilm often slough off, traveling through the host and potentially spreading the infection to a different location.

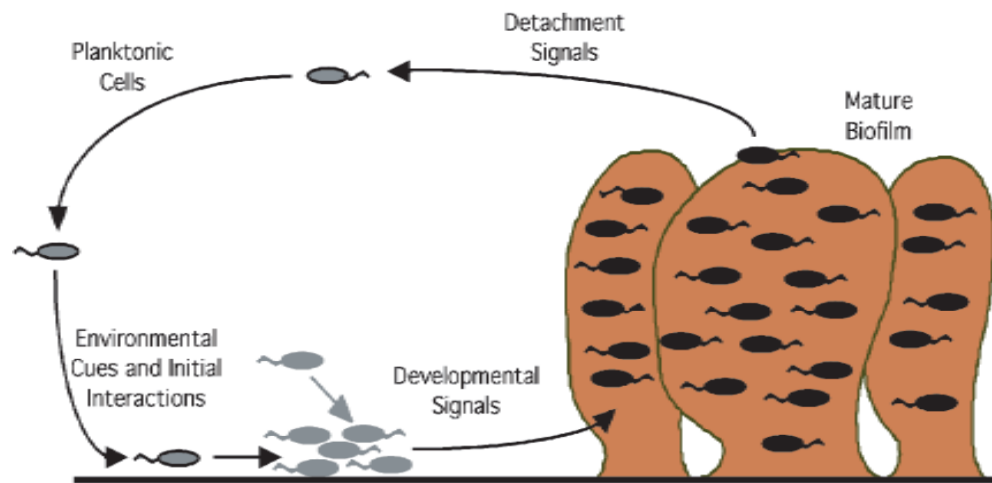


Figure 1.1. Diagram of the biofilm growth cycle, from bacterial adhesion to the substrate, formation of microcolonies, development of a mature structure, and detachment. Reproduced from [18].

Bacterial adhesion is the first stage of biofilm formation, and represents the onset of infection. Over the growth progression, biofilm cohesion and adhesion to the substrate are thought to be general indications of the maturity and strength of the biofilm. Interestingly, even within a species, environmental conditions can affect the degree of adhesion [18]. Pratt and Kolter demonstrated that *E. coli* K-12 grown in Lysogeny broth (LB) or in minimal media supplemented with casamino acids is capable of forming biofilms on abiotic surfaces, but is unable to initiate biofilm formation in unaltered minimal media [19]. In contrast, *E. coli* O157:H7 biofilms grown in low nutrient media have been shown to form more quickly and have more extracellular matrix than biofilms grown in media with high nutrient concentrations [20].

A number of studies have indicated that motility is essential for biofilm initiation and survival [18, 21]. First, motility can aid in bringing cells to the substratum, as in the flagellar-mediated swimming of *E. coli* and *P. aeruginosa* necessary to convey bacteria

close enough to the surface to initiate adhesion events. In *E. coli*, deletion or mutation of genes responsible for synthesis and functioning of flagella and type-I pili have yielded less biofilm-associated biomass as compared to wild type biofilms [15, 19]. Similarly in *P. aeruginosa*, dysfunctional flagella prevent biofilm formation [22]. Motility also mediates the aggregation of individual cells on the substratum into microcolonies. Mutation of type-IV pili and associated twitching motility in *P. aeruginosa* has been demonstrated to inhibit formation of microcolonies and structured biofilms [22]. However in *E. coli*, microcolony formation is largely mediated by flagella [19]. During the transition from separate microcolonies to a mature biofilm, adhesion to the substrate and cohesion within the biofilm remain critical for maintenance and maturation of the biofilm, as biofilm adhesion increases with growth time and with biofilm thickness [23].

The cohesiveness of a biofilm and its ability to retain its structure are partially determined by the composition of the extracellular matrix. This matrix is heterogeneous in nature and typically consists of a variety of biopolymers, known collectively as extracellular polymeric substance (EPS). EPS is typically composed of different types of polysaccharides, proteins, and DNA fragments existing in a hydrated network, enveloping the constituent bacteria [24]. While the exact composition of *E. coli* biofilms varies between reports, the most common major components include cellulose, β -1,6-*N*-acetyl-D-glucosamine polymer (PGA), and colanic acid [25]. *P. aeruginosa* biofilms typically contain alginate, Pel (a glucose-rich polysaccharide encoded by the *pel* operon), and Psl (a mannose, glucose, and rhamnose-rich polysaccharide encoded by the *psl* operon) [26].

One challenge to biofilm research is the sensitive and variable nature not only of bacterial growth, but also of biofilm development itself [27]. Typically, wide spreads in biological data are narrowed by repeating an experiment multiple times, as increasing the sample size increases the likelihood of obtaining data representative of the population. Compounding the variability within one set of experiments is the variability observed between studies; as Beloin and Ghigo noted in a review [28], three different analyses of *E. coli* gene expression in biofilms found only two genes in common [29-31]. While more studies and standardization of methods between laboratories will clarify trends between biofilm models, it may be the case that no two biofilms can be compared.

1.3.1.2 Transport Within Biofilms and Between their Environments

As a biofilm grows, the thickness increases as bacteria divide and secrete more EPS. The thickness and overall morphology of the biofilm are dependent on the physical and chemical environment. Metabolic activity within the biofilm is dependent on the diffusion of nutrients, waste products, and other metabolites throughout the structure; this diffusion is in turn reliant on the biofilm structure and the environmental hydrodynamic properties, such as shear stress imposed on the biofilm. Conversely, the biofilm itself interacts with the local environment, chemically altering concentration gradients and physically altering flow profiles; the morphological properties of the biofilm are thus developed through feedback between the bacteria and the environment. A number of mathematical models of biofilm formation have been developed [32-34], and typically involve accounting for accumulation rates and transfer of cells, nutrients, oxygen, and metabolites within a biofilm reactor, as summarized in Figure 1.2.

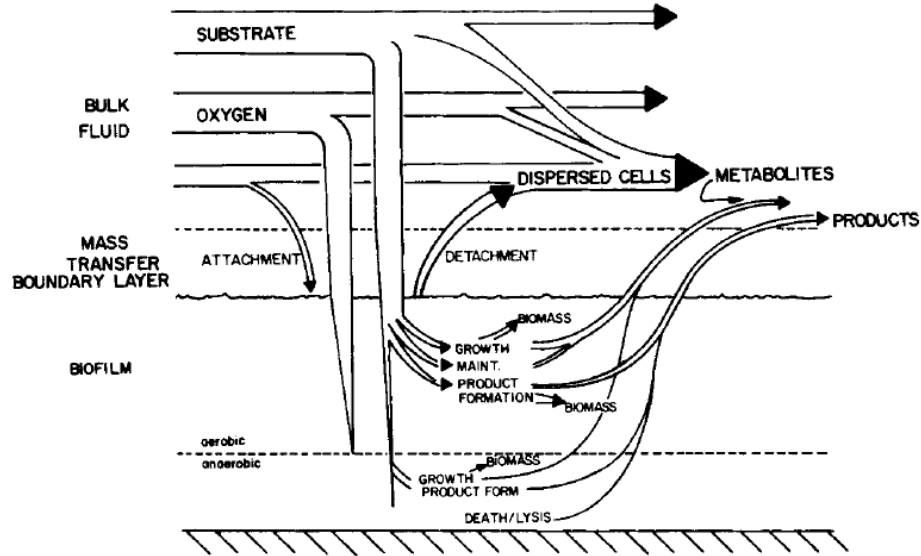


Figure 1.2. Diagram representing a common mathematical biofilm model accounting for interrelated processes in a biofilm reactor. Reproduced from [33].

Changes in biomass, corresponding to the biofilm thickness, rely on metabolic growth rates dependent on substrate and oxygen availability; these may be modeled using Monod kinetics combined with species conservation in the system, summarized by

$$\frac{\delta \rho_i}{\delta t} + \frac{\delta n_{iz}}{\delta z} = r_i,$$

where ρ_i is the mass concentration of species i , n_{iz} is the mass flux of species i in the z -direction (normal to the substrate), and r_i is the rate of production of i [32].

In addition to dynamics associated with bacterial growth, division, and death, the fluidic environment influences the biofilm by creating convective flux of molecules into and away from the biofilm. Additionally, flow over the biofilm imposes shear forces that can delaminate cells or segments of biofilm. The shear stress in a flow cell is a function of flow rate, growth media viscosity, chamber dimensions, biofilm thickness and roughness, over time. Biofilms formed under large amounts of shear stress, which may be created in a flow cell reactor or *in vivo* in arterial vasculature, are often thinner and

more densely packed than undisturbed biofilms [15, 32, 35]. Rochex et al. showed that shear stress affects the composition, diversity, and maturation rate of biofilms [36]. Additionally, Chen et al. showed that the degree of adhesion, evaluated using micromanipulation, is also dependent on the shear rate at which the biofilm is formed [37]. Therefore, when evaluating a biofilm and its response to stimuli, the chemical and physical environment in which it was formed must be considered.

1.3.1.3 Chemical Sensitivity and Antibiotic Resistance

Bacterial biofilms exhibit elevated resistance to antibiotic treatment, compared to bacterial suspensions. There are a number of hypotheses and research investigations concerning what mechanisms enable biofilm resistance and tolerance of antibiotics [4, 38]. Figure 1.3 illustrates four of these mechanisms.

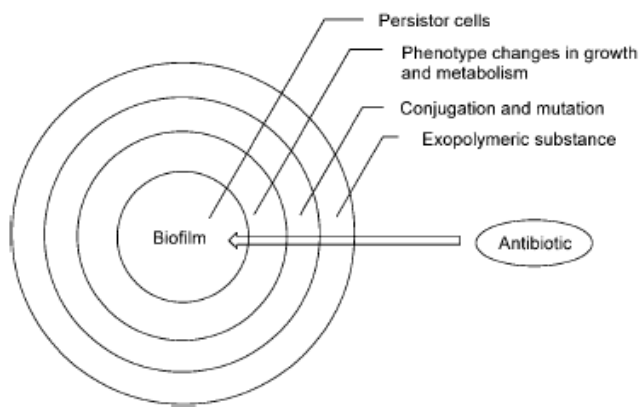


Figure 1.3. Illustration of antibiotic resistance mechanisms in biofilms, indicating several contributors that individually reduce the impact of antibiotics on a biofilm. Reproduced from [4].

First, the EPS itself can reduce the potency of antibiotics applied to biofilms. Antibiotics that interact with the EPS are often prevented from completely penetrating thick biofilm layers [39-41]. For example, a major component of the *P. aeruginosa* EPS, alginate, is anionic, and can bind cationic antimicrobial agents and retard their diffusion into the biofilm [42]. However, other studies have shown that slow diffusion of

antibiotics through the EPS might not be a function of the EPS composition, but rather of other factors secreted by the constituent bacteria [43] or of the type of antibiotic and bacterial species [44]. For instance, while tetracycline penetrates completely into *E. coli* biofilms [45], it does not completely eliminate the biofilm, supporting multiple mechanisms of antibiotic resistance that encompass a range of antibiotics and growth conditions. Altered chemical environments within the biofilm, for example by accumulation of acidic waste products [46], are also hypothesized to interfere with antibiotic activity [47, 48] and promote resistance.

Second, high rates of conjugation have been observed within biofilms, and are largely a function of the large number of contact points between cells in a biofilm [49, 50]. Horizontal gene transfer often promotes biofilm survival, as genes coding for behaviors such as antibiotic or metal resistance are often carried on plasmids that can be transferred between cells [51]. Interestingly, Ghigo showed that conjugative plasmids themselves encourage biofilm formation, and suggested that conjugative pili connections between cells can initiate adhesion events between cells, and thereby contribute to biofilm cohesion [52].

Third, the chemical environment within biofilms is believed to promote antibiotic tolerance by altering bacterial rates of metabolism and growth, thereby removing antibiotic targets. There is evidence of hypoxic conditions deep within biofilms, shown by the upregulation of genes associated with oxygen limitation. For example, Schembri et al. observed increased expression in *E. coli* biofilms of the *cydAB* and *b2297-hybAC* gene clusters, shown to be induced in oxygen-limited environments [31]. As seen in experiments with planktonic cultures, lack of nutrients or oxygen will lower rates of

metabolism and growth; bacteria in biofilms have also been shown to have slower growth rates than bacteria in suspension [44]. Targets of antibiotics are typically processes vital to actively growing bacteria, such as metabolism or cell wall production. Removal of these targets in slow-growing bacteria in biofilms is thought to contribute to antibiotic tolerance of biofilms.

Differences in nutrient concentrations and anaerobic niches within the biofilms can lead to persister cells. Persister cells are cells which have entered a dormant, inactive stage that are often compared to spores, and can persist even in prolonged exposure to elevated antibiotic concentrations. Similar to the slow-growing cells within the biofilm, the antibiotic tolerance of persisters is thought to be at least partially due to the removal of antibiotic targets due to their dormant state. Under favorable conditions, persisters can revert to live cells and reseed biofilm formation [53, 54].

In addition to antibiotics, biofilms also exhibit resistance to treatment with chemical agents such as sodium dodecyl sulfate (SDS), a hydrophobic agent that serves as a detergent. Biofilm resistance to SDS treatment can be used as a metric to evaluate biofilm stability [55-57]. As an example, this technique was used by Davies et al., who observed that biofilms formed by *P. aeruginosa* with a mutation hypothesized to weaken the ECM were removed from the growth chamber after exposure to SDS more easily than wild type biofilms [56].

1.3.1.4 Bacterial Quorum Sensing and Biofilms

Many types of bacteria communicate with each other biochemically in a behavior known as quorum sensing (QS). Quorum sensing molecules, or autoinducers, are synthesized and secreted into the extracellular environment. Bacteria are capable of

detecting the surrounding concentration of autoinducers either by nonspecific uptake of the molecules or through autoinducer binding to a receptor, which both in turn will create a population-dependent, intracellular cascade regulating a number of genes associated with QS [58], as illustrated in Figure 1.4. Numerous genes are thought to be regulated by QS activity; many of these genes control phenotypes associated with bacterial pathogenicity, including the secretion of toxins and the formation of biofilms [58, 59].

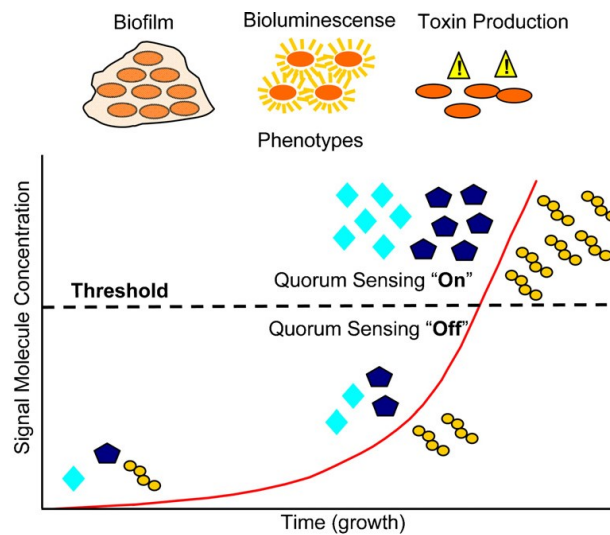


Figure 1.4. Schematic of behaviors switched on by QS and accumulation of autoinducer molecules in the extracellular environment. Reproduced from [59].

While QS systems vary between different types of bacteria, particularly between Gram positive and negative bacteria, the second class of autoinducer, AI-2, is referred to as “universal” since its synthase, LuxS, is found in more than 70 bacterial species [60]. Strains that are believed to use AI-2 for intercellular communication include *Vibrio harveyi*, *Salmonella typhimurium*, and *E. coli* [61]. In *E. coli*, AI-2 is synthesized in a multistep process, using the enzymes Pfs and LuxS to convert S-adenosyl-L-homocysteine (SAH) to 4,5-dihydroxy-2,3-pentanedione (DPD). DPD is cyclized and undergoes further restructuring to yield AI-2, which is then secreted. AI-2 has been

shown to be imported into cells both through interactions with the AI-2 transporter encoded by the *lsrACDB* operon, and also through non-specific uptake [62]. Intracellularly, the molecule is phosphorylated by LsrK, after which it interacts with the repressor LsrR, allowing for transcription of the *lsr* operon, including genes regulating AI-2 uptake and processing [63].

QS is of particular interest as it controls a number of processes contributing to the formation of biofilms by a bacterial community. Figure 1.5 illustrates several contributors to biofilms that have been linked to QS.

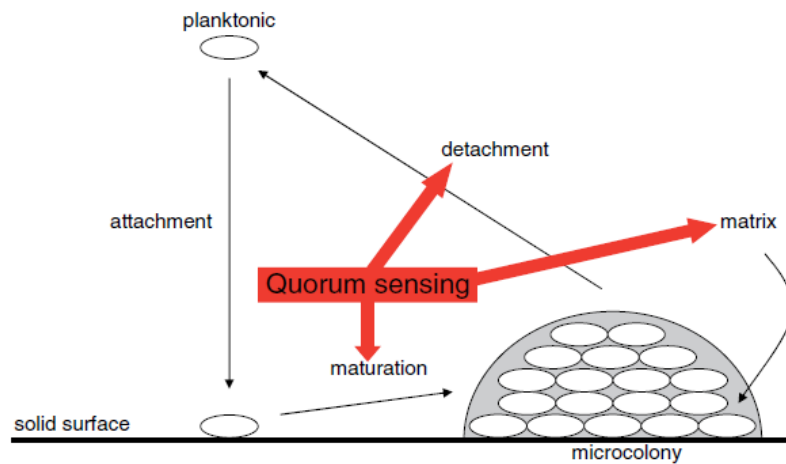


Figure 1.5. Illustration of aspects of bacterial biofilm formation and growth influenced by QS. Reproduced from [64].

P. aeruginosa uses QS extensively to modulate both biofilm formation and maturation, using acyl-homoserine lactone (AHL) molecules in autoinducer-1 (AI-1) signaling. It has been shown that *P. aeruginosa* deficient in producing AHLs formed thinner biofilms that were more sensitive to detergents compared to wild-type biofilms [56]. Also, AHLs were found at higher concentrations in *P. aeruginosa* biofilms than in planktonic cultures [65]. In *E. coli* biofilms, addition of AI-2 was shown to increase biofilm mass 30-fold [15]. *E. coli* strains lacking the AI-2 signaling regulators *lsrK* and

lsrR have been observed to form thinner biofilms than wild type *E. coli* [16]. AI-2 has also been linked to *E. coli* motility [15, 25] and EPS synthesis [17], discussed in Section 1.3.1.1 as major contributors to biofilm formation. While *P. aeruginosa* primarily uses the AI-1 QS system for communication and does not synthesize AI-2, gene expression in this species can still be regulated by extracellular AI-2 produced by surrounding microflora [66]. These genes include virulence genes, such as rhamnolipid production and exotoxin genes, implying that AI-2 is capable of altering *P. aeruginosa* gene expression and pathogenicity [66]. Interestingly, QS does not appear to have a significant impact on the formation of persister cells, an additional contributor to chronic biofilm infections. Unpublished studies mentioned in a review by Lewis refer to experiments evaluating the effect of AI-2 on the incidence of persister cells [54]. These experiments were performed by adding spent media with high concentrations of AI-2 to a new culture of bacteria, which was treated with a large dose of antibiotic. No increase or decrease in persister cell incidence was observed [54].

While QS is a major contributor to infection severity, QS itself is not essential to bacterial growth and survival. As a result, inhibition of QS has been pursued as an alternative antibacterial treatment [67-69], whereby phenomena such as biofilm formation and toxin secretion could be circumvented. QS inhibition will be discussed later in this chapter in Section 1.3.2.4.

1.3.2 Alternative Biofilm Treatments

Considering both the rise of multi-drug resistant bacteria and the increased antibiotic tolerance of bacteria in a biofilm, the need for an alternative treatment approach is evident [4]. While a number of nontraditional methods for preventing or eliminating

bacterial biofilms are being pursued by the scientific community at large, two approaches currently under study by my colleagues and collaborators are presented below.

1.3.2.1 Bioelectric Effect

Exposure of a biofilm to an electric field applied in conjunction with antibiotics has been observed to enhance the normal biocidal activity of antibiotics in a phenomenon termed the “bioelectric effect” [70, 71]. Researchers have proposed a number of hypotheses for the mechanism of augmented bacterial killing by the bioelectric effect. The applied electric field may enhance the penetration of antibiotics into the EPS, either by applying electrophoretic force to antibiotic molecules or by increasing cell membrane permeability similar to electroporation [72, 73]. With a weakened first line of defense, biofilms can more readily be treated with antibiotics. Additionally, oxidants may be electrochemically generated upon application of the electric field and can impede normal antibiotic activity [71, 72, 74]. Stoodley et al. also postulated that the biofilm may expand and contract depending on the polarity of an applied alternating current electric field, and thereby enhance convective transport of antibiotics into the biofilm [72].

Studies of the bioelectric effect throughout literature implemented either an AC or a DC electric field, but never a combination of the two. Within my research group, Kim et al. demonstrated the enhanced efficacy of biofilm inhibition by the bioelectric effect by combining alternating and direct current (AC and DC) electric fields [75, 76]. By using different modes of electrical energy applied, the applied voltage at which inhibition was observed was reduced below the limit for water electrolysis (0.82 V). This presents a significant advantage, as much of the body of work on the bioelectric effect relies on applying voltages above this threshold, potentially generating gas within the solution.

While hydrolysis may contribute to bacterial biofilm killing by the bioelectric effect, the products can damage surrounding microflora or host cells near the biofilm and applied electric field.

1.3.2.2 *Quorum Sensing Inhibition*

Quorum sensing is thought to be an ideal drug target for the development of new antimicrobials, as it does not influence cell growth or viability, as discussed in Section 1.3.1.4. Consequently, there have been many studies on QS inhibitors with the hypothesis that development of resistance to this treatment will either not occur or be delayed. Much work has been performed developing analogs of AHL molecules [68, 69]. The effects of these analogs on both QS and biofilm formation have been evaluated and verified [77, 78]. Importantly, small molecule inhibitors of AI-1-based QS were shown to work synergistically with antibiotics in clearing biofilms formed *in vivo* [79, 80].

As AI-2 is involved in QS in over 70 species of bacteria, AI-2 signaling inhibitor development, as reviewed by Guo et al. [67], has the potential for widespread scientific and clinical utility. There has been recent development of different AI-2 analogs shown to be effective QS inhibitors [81-84]. C-1 alkyl analogs of AI-2, including isobutyl-DPD, were developed and shown by my collaborators to be highly effective broad species QS inhibitors in *E. coli*, *S. typhimurium* and *V. harveyi* [83, 84]. Isobutyl-DPD is phosphorylated by LsrK in *E. coli* and inhibits QS-related *lsr* expression in the presence of the repressor of the circuit LsrR [84]. Additionally, Gamby et al. showed that a different C-1 alkyl analog, phenyl-DPD, inhibits QS-dependent production of pyocyanin in *P. aeruginosa* [85]. While AI-2 analogs able to inhibit QS in several types of bacteria

have been developed, prior to the work performed in this dissertation there were no detailed studies of how these analogs affect bacterial biofilms.

1.3.3 Macroscale Evaluation of Biofilms

1.3.3.1 Biofilm Reactors

In developing biofilm science and investigating new ways to eliminate biofilms, researchers employ a variety of formats for growing biofilms and for evaluating their characteristics. Microwell plates are one of the most common formats for growing static biofilms. Microwell plate readers are staples in molecular biology and microbiology laboratories, and can typically measure optical absorbance, fluorescence, luminescence, and even scattered light. Advanced robotic systems for filling and mixing reagents in microwells exist to streamline the laboratory workflow and minimize time invested by the researcher.

As opposed to static biofilm reactors, growing biofilms under flow provides a continuous supply of nutrients to the biofilm in addition to aiding in continuous removal of planktonic cells, separate from the biofilm, from the system. Flow cells can be purchased commercially, purchased from research groups, or can be custom-machined in plastic such as polystyrene. [9, 86]. They typically have one inlet, one outlet, and one main channel throughout which biofilms are formed. Many of the flow cells have a transparent floor made from a slide or coverslip, and are designed to be mounted on a microscope stage for imaging during growth. Such a configuration allows for continuous monitoring of biofilm physiology, or of genetic expression visible via fluorescent protein expression. However, if chemical sensitivity is to be evaluated, the entire biofilm must

be exposed to the treatment due to the typical reactor configuration, requiring comparison of separately grown biofilms in order to evaluate control and experimental groups.

The modified Robbins device is similar to standard flow cells in that a constant flow of growth media is provided. However, the device contains multiple specimen plugs on which biofilms can be grown, as shown in Figure 1.6 [11]. After biofilm formation, the plugs can be removed and placed in antibiotic solutions to test for antibiotic susceptibility, or sonicated to remove the biofilm cells and determine the viable cell content. While biofilms are grown in parallel, their analysis remains serial in this configuration.

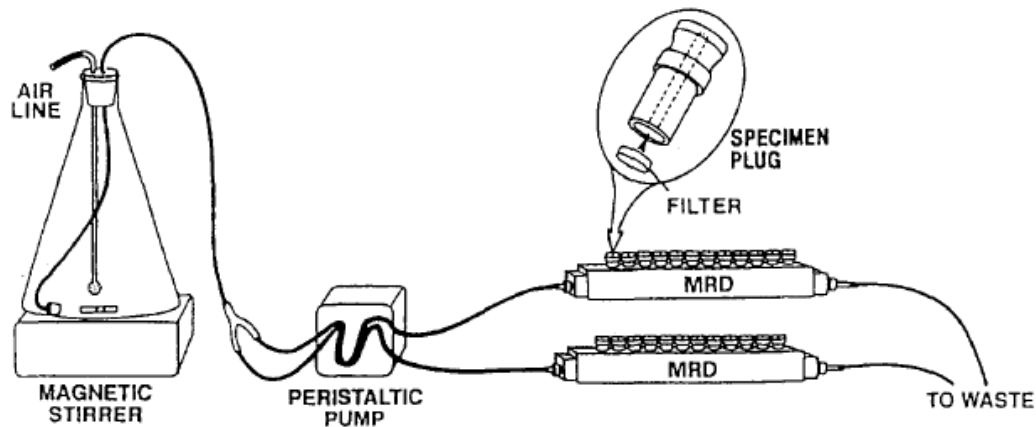


Figure 1.6. Schematic of Modified Robbins Device, indicating fluidic connections and plugs upon which biofilms grow. Reproduced from [11].

The Calgary Biofilm Device [8] combines the high-throughput biofilm formation provided by a microwell plate with the application of consistent shear stress provided by the modified Robbins device. The reaction vessel has two components, illustrated in Figure 1.7. Pegs on the lid can be positioned in the channels of the bottom component, and are sized to fit also within the wells of a 96-well plate. The bottom of the device directs flow (created by placing the device on a rocking table) around the pegs so that biofilms growing on the pegs experience a consistent amount of shear force. Biofilms on

individual pegs can be removed as in the Robbins device, and analyzed for viable cell content. Alternatively, the lid can be inserted in a microwell plate filled with varying concentrations of antibiotics, and biofilms on individual pins tested for antibiotic susceptibility in parallel. In order to image the biofilms, however, pins must be broken off the lid and manipulated so that the biofilms can be imaged using confocal or scanning electron microscopy. After evaluating the biofilm, there is no potential for reinstating biofilm formation on the same pin.

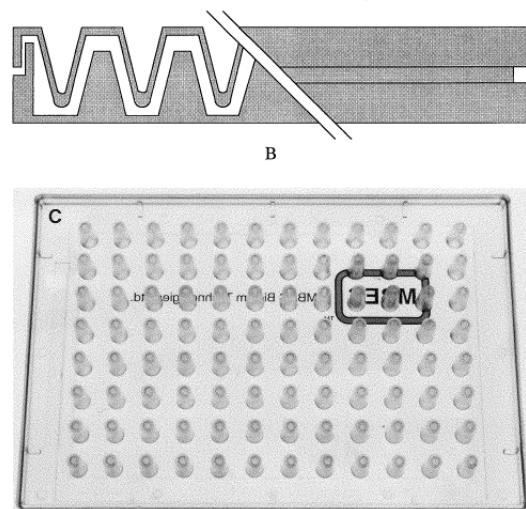


Figure 1.7. Cross-sectional diagram (top) and top view (bottom) of a Calgary Biofilm Device. The diagram illustrates the space allowance for growth media flow between the pegs and the bottom of the device. As seen in top-down view, the pegs are arrayed in a 12x8 array compatible with a 96-well plate. Reproduced from [8].

1.3.3.2 End-point Measurement Methods

One of the most commonly used techniques for biofilm quantification is crystal violet staining [87-89]. Crystal violet is applied to a biofilm, where it binds to negatively charged exopolysaccharides and molecules on bacterial cell surfaces. After rinsing excess dye from the biofilm, the bound stain is solubilized and is then quantified via the optical absorbance of crystal violet at 590 nm. While this staining method is a standard biofilm metric, it can produce variable results as the stain penetration into the biofilm or degree of binding to the cell wall can be variable. This can be addressed by removing the

biofilm from the reactor surface and thoroughly mixing it with the stain, sacrificing morphological information at the same time.

As high resolution microscopic methods become more widely available, biofilms are commonly evaluated using confocal microscopy and scanning electron microscopy (SEM) [32, 90-93]. Confocal microscopy provides insight into the structures formed by fluorescent cells. Fluorescence can be obtained by using a cell line modified to express a fluorescent protein either constitutively or upon the application of a stimulus. However, the insertion of such plasmids can affect other aspects of the bacterial phenotype, potentially creating a biofilm that does not reflect what might be formed by the wild type strain of bacteria. For example, three different strains of *E. coli* engineered for constitutive expression of green fluorescent protein (GFP) all exhibited decreased sensitivity to β -lactam antibiotics, but showed increased sensitivity to other antibiotics including tetracycline, ciprofloxacin, and vancomycin [94]. Alternatively, the biofilm can be fluorescently stained using a number of stains, often available in commercial kits such as the Filmtracer™ LIVE/DEAD® Biofilm Viability Kit (Invitrogen Corp.). Provided a fluorescently stained biofilm, confocal microscopy will generate images at different heights throughout the biofilm. The series of images can be used to generate three dimensional representations of biofilm structures using software such as Imaris (Bitplane, Inc.) or Volocity (PerkinElmer, Inc.). Quantitative information can be obtained through image analysis, often performed using COMSTAT, the software developed by Heydorn et al. to aid in standardization of biofilm quantification techniques [12, 95]. This software provides morphological data, such as average thickness,

substratum coverage, biomass, and roughness, all of which can be used to characterize biofilms.

SEM provides more detailed information than confocal microscopy by virtue of its high resolution. This technique can be used to evaluate the quality of the extracellular matrix and its interaction with cells within the biofilm [92, 93, 96]. Traditional SEM techniques involve supercritical drying and coating of the biofilm with metal for electron microscopy in a high vacuum environment, dehydrating the biofilm in the process and preventing further growth. ESEM allows imaging of the biofilm in a hydrated state, providing information more representative of the biofilm in its natural state. Electron microscopy is typically implemented as an endpoint measurement technique. Factors contributing to the inability to use ESEM throughout growth include the performance of imaging at low temperatures close to freezing and the need to have the surface of the biofilm interact with the electron beam, preventing imaging through an enclosed biofilm reactor. A comparison of images obtained using confocal microscopy, SEM, and environmental SEM (ESEM) is shown in Figure 1.8.

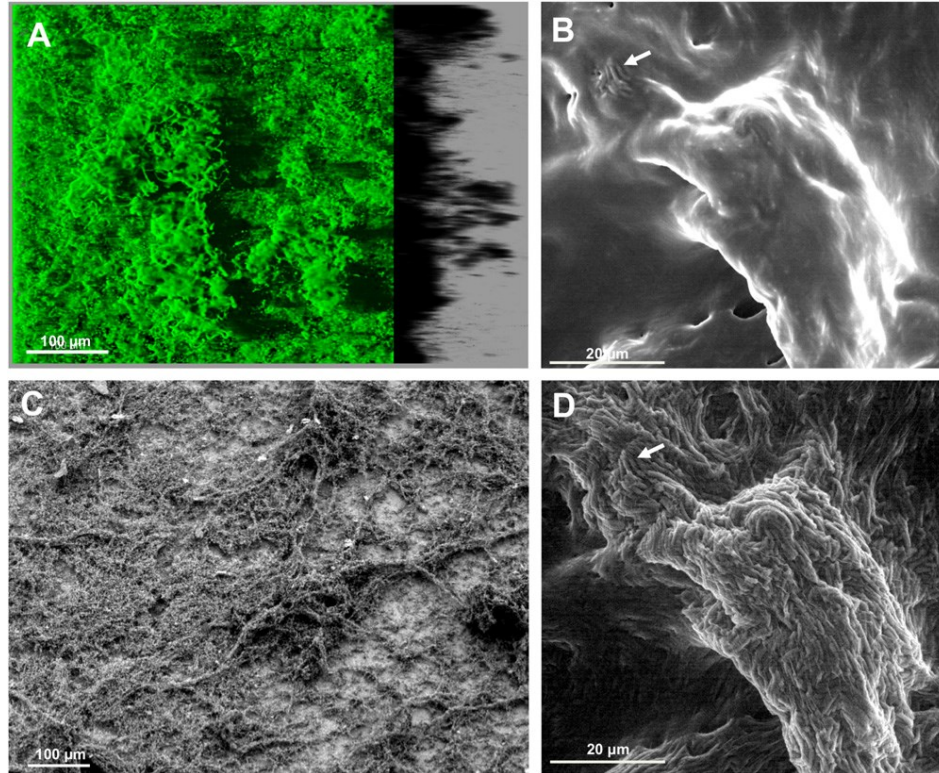


Figure 1.8. Images of a *Bacillus subtilis* biofilm obtained using A) Confocal microscopy C) Field emission SEM, similar to standard SEM apart from the use of a field emitter instead of a thermionic emitter in order to minimize distortion and obtain higher resolution B) ESEM performed at a chamber pressure of 4 Torr D) ESEM performed at 5 Torr. Reproduced from [96].

Biofilms may also be analyzed for chemical content using destructive processes to prepare samples for quantification of total protein content, total organic carbon content, and microarray analysis [14, 15, 90]. While these techniques provide multiple types of information about biofilms, they are all end point measurements, as the biofilm is destroyed in the analysis process. Therefore, in order to obtain information corresponding to biofilms at different points in growth, several experiments must be performed.

1.3.3.3 Noninvasive Measurement Methods

As evident in the biofilm reactors presented above, one challenge in studying biofilms is observing biofilm properties in a non-destructive manner. While not as

commonly used as the endpoint techniques described above, a number of methods which can be used on unlabeled biofilms at any point during growth have been developed; a review of such techniques has been presented by Janknecht and Melo [97]. One such method to evaluate biofilms is via their electrical properties, as the cells and EPS within biofilms serve as a dielectric material and thereby provide the biofilm an electrical impedance that can vary with time or with structure and composition of the biofilm. The electrical signature of a biofilm can be assessed using methods such as electrochemical impedance spectroscopy or capacitive measurement techniques [97-100].

Fiber optic sensors have also been used to evaluate biofilm growth noninvasively [97]. The amount of biofilm may be quantified by the observed turbidity in the biofilm reactor; this can be implemented as a differential measurement, with one turbidity measurement obtained at the biofilm, and one measurement at a point with no biofilm due to water jets physically removing biofilm from that location [101]. Alternatively, Tamachkiarow and Flemming evaluated the biofilm formed at one location in a brewery water pipeline by using a fiber optic probe to measure light scattered from a separate source, and monitoring the change over time [102].

Using a similar principle as the fiber optic device of Tamachkiarow and Flemming, Bakke et al. performed a detailed study investigating biofilm optical density as a unique property by which biofilms may be characterized. *P. aeruginosa* biofilms were formed in macroscale flow cells in the configuration shown in Figure 1.9. Growth media was introduced into two parallel rectangular tubes to simultaneously grow biofilms over the surfaces of both tubes. The optical density at 420 nm at selected points in time

was measured between points A and D as shown in Figure 1.9 using a fiber optic probe [14].

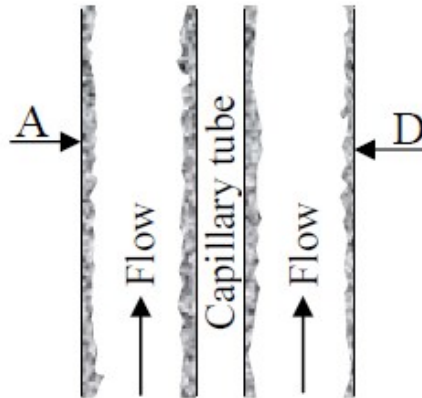


Figure 1.9. Schematic of biofilm flow cell reactor used by Bakke et al. Biofilms were formed in parallel rectangular tubes (1.0x3.0x300 mm), formed by inserting a water-filled capillary into a larger square tube in order to create a large surface area for biofilm formation. Optical density at 420 nm was measured between points A and D using a fiber optic probe. Reproduced from [14].

The change in biofilm optical density from the baseline was compared to the change in optical thickness; while the two were not directly correlated, it was shown that as the biofilm grows, optical density increases. The optical changes observed were hypothesized to be due to light scattered by cells within the biofilm, similar to turbidity measurements performed on bacterial suspensions in a spectrophotometer. While the implementation of the flow cell precludes continuous optical measurements, this work demonstrated the viability of biofilm monitoring via optical absorbance. The principle of detection may be applied to microscale systems integrated with inexpensive optical components (i.e. a light source and a photodetector) capable of continuous optical sensing.

1.3.4 Microfluidics

Microscale systems are able to address many of the disadvantages to the previously described macroscale biofilm models and measurement techniques. The use

of microfluidics in particular allows for greater control of the fluidic environment and incorporation of microfabricated sensors or micropatterned growth substrates [103, 104]. Additionally, larger platforms such as microwell plates require large sample sizes, often on the order of tens of microliters, while microfluidic systems may use reagent volumes on the order of nanoliters. While large samples of bacteria are simple to obtain, as they are a self-renewing resource, it is often difficult or expensive to obtain large volumes of reagents such as antibodies or drugs under development. Several microfluidic methods have been employed in biological applications such as electrophoresis, on chip PCR, and cell-free protein synthesis [105, 106].

While the simplest microfluidic systems, single channels or chambers, are miniatures of existing macroscale platforms such as microwell plates or flow cells, complex fluid handling architectures can be integrated with arrays of channels or chambers in the epitome of a “lab on a chip”. On-chip pumps can provide tunable flow of solutions throughout a device without the need for an external pump. Integrated valves can direct this flow to designated locations on demand. There are many configurations of valves, such as implementation of external pins or solenoids [107, 108] to compress a fluidic channel embedded in the flexible silicone polydimethylsiloxane (PDMS). Integrating valves into PDMS itself and using a pressurized gas [108-111] to control the valve orientation is a popular valving scheme used in much of today’s microfluidic work. These types of integrated valves are convenient for imaging the contents of the microfluidic channels, since using only an in-plane gas line to actuate the valves maintains an open line of sight for optimal characterization of channel contents via microscopy.

A unique feature of microfluidics is their ability to be integrated with sensors by virtue of compatible fabrication technologies. A multitude of microfabricated sensing systems have been developed for biological applications using a variety of transduction mechanisms. For example, impedimetric and capacitive sensors can measure changes in electrical properties imposed by deposition of molecules or cells on the surface of a microfabricated sensor [100]. Surface acoustic wave (SAW) sensors use a piezoelectric material to generate surface acoustic waves whose resonance properties change with mass deposition on the sensor [112, 113]. Cantilevers with surface functionalization layers will display altered mechanical properties, such as bending or resonance change, upon analyte binding to the surface. The change in mechanical properties can be measured a variety of ways, such as with integrated piezoresistors [114] or with external interferometric readout [115]. These sensors, by nature of being batch microfabricated, offer the benefits of being small, inexpensive, and easily integrated with many other types of sensors to create a multimodal sensing platform. Microscale sensing provides the added benefit of being as sensitive as macroscale methods, while maintaining fast response times.

1.3.5 Microsystems for Biofilm Growth and Characterization

While studies of biofilms and of microfluidics have existed for decades, recently the two fields have merged and spawned research providing new insight on the mechanical properties of biofilms [116, 117], roles of intercellular communication [32, 111, 118-120], and development of antibiotic resistance [121] among other topics [122, 123]. Highlights of published work from this body of research are summarized below in Table 1.1.

Table 1.1. Summary of highlights from published work utilizing microfluidic platforms for biofilm studies.

Authors	Cross-Sectional Dimensions of Growth Reactor (width x height)	Biofilm-Forming Strain/s	Growth Media	Flow Rate/s	Evaluation Method	Notes
Janakiraman et al. [32]	600 μm x 250 μm	<i>P. aeruginosa</i> PA14	M63 minimal media	2.3,7.4, 21 nL/s	Confocal microscopy	Flow rate variation, correlation to mathematical model
Richter et al. [104]	~1.5 mm x 20 μm	(Fungi) <i>Candida albicans</i> , <i>Pichia pastoris</i>	Malt extract boullion, Worth broth	0.12 $\mu\text{L}/\text{min}$	Impedance spectroscopy	Grew fungal biofilms in microfluidic device with integrated electrodes for continuous, online measurement
Kim et al. [111]	600 μm x 200 μm	<i>E. coli</i> EHEC	LB	2 $\mu\text{L}/\text{s}$	Confocal microscopy	Integrated mixer for generation of biofilm inhibitor concentrations
Mosier et al. [117]	2.45mm x 100 μm	<i>P. aeruginosa</i> PAO1	M9 + glucose + CAA	2 $\mu\text{L}/\text{min}$	Atomic force microscopy (AFM), confocal microscopy	Used open microfluidic channel for AFM measurement during biofilm growth
Hong et al. [120]	600 μm x 150 μm	<i>E. coli hha</i> ,	M9, LB+glucose	2 $\mu\text{L}/\text{s}$, pulsed flow	Confocal microscopy	Introduced engineered <i>E. coli hha</i> “dispenser” cells into established <i>E. coli hha</i> “colonizer” cell biofilm
Kim et al. [121]	300 μm x 40 μm	<i>P. aeruginosa</i> PAO1 pMRP9-1	LB	0.1 $\mu\text{L}/\text{min}$	Fluorescence microscopy (non-confocal)	Generated antibiotic gradient to determine minimum biofilm eradication concentration
Skolimowski et al. [123]	300 μm x 150 μm	<i>P. aeruginosa</i> PAO1	Fastidious anaerobe broth (FAB) + sodium citrate	10 $\mu\text{L}/\text{min}$	Confocal microscopy	Exposed biofilm to oxygen gradient while measuring oxygen concentration
Kim et al. [124]	1200 μm (diameter of well) x 100 μm	<i>E. coli</i> BW 25113	Dulbecco’s modified Eagle medium (DMEM)	(static)	Confocal microscopy	Co-culture of commensal bacterial biofilm with epithelial cells; observed interaction with <i>E. coli</i> EHEC injected from separate port controlled by valve actuation

The majority of these studies utilized direct measurement of biofilm thickness and morphology using microscopy and image analysis, but did not demonstrate real-time monitoring of bacterial biofilm characteristics. One study, by Richter et al., employed a microfluidic platform with integrated electrodes for impedance spectroscopy to evaluate fungal biofilm formation [104]. However, this method has not expanded to the

community of bacterial biofilm researchers. Some of the studies leveraged properties of microfluidics to create environments more difficult to obtain with traditional reactors. Diffusive mixers have been incorporated within microfluidic platforms for biofilm formation so that two solutions, such as growth media and an antibiotic, may be injected and mixed to either one [121] or several desired concentrations [111, 120]. Kim et al. used controllable PDMS structures to isolate, then integrate cultures of epithelial cells and bacteria [124]. The same group also used integrated PDMS valves to control seeding of a device with bacteria introduced from a port separate from the port for growth media introduction [111, 120, 124].

Once the biofilm has formed in a microfluidic device, variability between devices still exists, as with macroscale biofilms [12, 125]. As a result, many studies performed on biofilm formation are conducted as demonstrations and rarely report more than three repetitions of an experiment. One method of addressing device-to-device variation is performing multiple experiments simultaneously on parallel biofilms grown in separate channels of the same device [111, 120]. Although some work has investigated the reproducibility of biofilm morphology in flow conditions [12] and the correlation between biofilm optical density and carbon content [14], these investigations have been performed on biofilms formed in macroscale reactors. While there is no variability difference between micro- and macroscale reactors at the cellular and molecular level of biofilm formation, microscale confinement alters the surrounding fluid dynamics and yields biofilms with compositions, morphologies, and variabilities that cannot be compared to those of biofilms in macroscale reactors. There have been no reported

investigations of either morphology or optical density reproducibility in microfluidic biofilm reactors prior to the work performed in this dissertation.

1.4 Structure of Dissertation

The preceding chapter presented the motivation behind the work performed in this dissertation, along with background information to establish the context of the research work. The following three chapters each address one of the three major accomplishments presented in Section 1.2. Chapter 2 presents the development of a microfluidic platform featuring continuous optical measurement of biofilm growth, and a discussion of biofilm reproducibility and data analysis. Chapter 3 covers the application of this platform toward evaluating inhibitory effects on biofilms by a new class of quorum sensing inhibitors. Chapter 4 presents the design, fabrication, and experimental demonstration of a microfluidic device designed not only to multiplex biofilm experiments, but also to address variation between biofilm experiments. Chapter 5 summarizes the work of the dissertation, and concludes with a discussion of future studies that can be performed as continuations or offshoots of the presented work.

2 Monitoring of Biofilm Formation in Microfluidics via Optical Density

This chapter covers the use of optical density monitoring as a means of evaluating bacterial biofilms formed in microfluidics. The development of the first microfluidic platform with optical density biofilm monitoring is described, including the device fabrication, biofilm growth, and data analysis. Also included is a brief description of activities that have emerged from this preliminary development, namely work performed by Mr. Matthew Mosteller. The development of the first-generation device has also been published in the Journal of Micromechanics and Microengineering [118], and the second-generation device development has been reported in the Master's thesis of Matthew Mosteller [126].

2.1 First Generation Device

The biofilm optical measurement platform presented below is the first demonstration of measuring optical density of biofilms formed in a microfluidic environment. Biofilm optical density was continuously and non-invasively measured with a simplified experimental setup using off-the-shelf electrical components. Biofilm optical properties were corroborated with biofilm morphological properties quantified using confocal microscopy and image analysis. The platform was used to investigate the dependence of *Escherichia coli* biofilm formation on quorum sensing. This investigation was achieved by comparing optical and morphological data between wild-type *E. coli* and *E. coli* incapable of quorum sensing molecule synthesis. The repeatability of biofilms formed in the platform using the developed methodology was also evaluated, toward the end of using the system as a reliable drug evaluation platform.

2.1.1 Platform Overview

As discussed in Section 1.3.4, microfluidics provide a number of advantages for biofilm research. Batch fabrication and the ease of operating simultaneous experiments allow for high throughput studies. The small volume serves as a tightly controllable microenvironment, and minimizes the amounts of reagents required for assays.

While a number of measurement techniques are available for integration within microfluidics, optical density was used for biofilm evaluation in this work. Optical density monitoring requires no labeling of bacteria with DNA-binding fluorophores or constitutive expression of GFP, preserving the viability and phenotype of the biofilm. Additionally, it can be performed in a continuous manner so that the real-time response of biofilms to stimuli can be observed. Bakke et al. showed that as a biofilm grows, its optical density increases due to the increased amount of light scattered by the biofilm structure and constituent bacteria [14]. The change in optical density from the baseline biofilm condition (ΔOD) over time can be defined as

$$\Delta OD(t) = -\log_{10}(I(t)/I_0), \quad (1.1)$$

where $I(t)$ is the transmitted light intensity measured by the photodiode at a selected time t , and I_0 is the baseline intensity measured after inoculation of the channel at the beginning of biofilm growth.

The microfluidic platform for optical density measurement of biofilms consisted of a micropatterned base providing measurement windows, a molded PDMS microfluidic channel, photodiodes placed under measurement windows, and light emitting diodes (LEDs) providing incident light. A cross-sectional schematic of the device indicating the optical implications is shown in Figure 2.1.

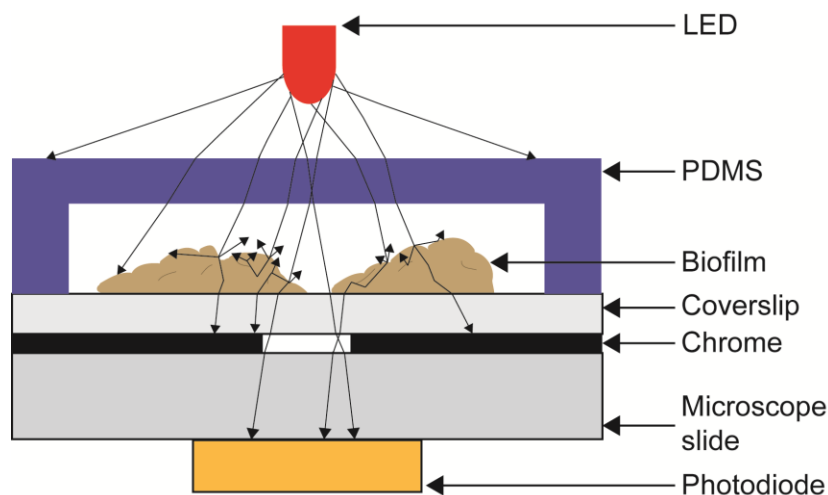


Figure 2.1. Schematic of PDMS microfluidic channel integrated with optical source and detector for optical density measurement of biofilms within the channel. The LED provided incoherent light, which scatters off the surface of and within the biofilm. Light that is transmitted through the pinhole in the chrome represents a combination of light that does not interact with the biofilm and light scattered from the biofilm. Overall, less light sensed by the photodiode implies a greater amount of biofilm either impeding transmission or scattering light away from the pinhole. Note: not to scale.

As illustrated in Figure 2.1, LEDs flooded the device with incoherent light, illuminating the biofilm directly above patterned pinholes in the chrome as well as adjacent biofilm. Here, the incident red light was assumed to interact with the biofilm solely through scattering and reflection; since characteristic absorbance peaks have not been reported for biofilms, it was assumed that optical density at any visible wavelength would provide representative information on the biofilm state. As DNA and proteins containing aromatic amino acids absorb light in the ultraviolet range at 260 and 280 nm respectively, the use of red LEDs with a peak emission wavelength of 660 nm was expected to minimize specific optical absorbance interactions with protein and DNA [127].

The use of LED illumination has its own set of advantages and disadvantages. Incoherent light yields a low signal since much of the light generated by the LED source does not interact with the biofilm. The biofilm itself acts as an additional source of scattering due to its heterogeneous composition of cells, EPS, and water. While the

photodiode may detect light scattered from an area of biofilm not directly above the measurement window, sections of biofilm above the window may also not be completely represented due to scattering of light away from the photodiode. The pinhole patterned in the chrome eliminates the majority of stray light from the LED, as well as some of the scattered light from the biofilm.

2.1.2 Platform Fabrication, Assembly, and Interfacing

2.1.2.1 Fabrication

As mentioned above, the microfluidic channel itself was formed by molded PDMS placed on top of a transparent base serving as the channel floor. The base was fabricated on a coverslip, providing a substrate that is both transparent and thin enough for high resolution inverted confocal microscopy of the biofilm. A 200 nm layer of chrome was sputtered onto the coverslip and patterned into two 200 μm x 200 μm windows using contact photolithography and chrome etching (see Appendix A, Mask #1). The windows were positioned 5 mm apart, with the first window 7.5 mm from the inlet. The chrome served as an opaque barrier to light, while the two patterned areas in each channel served as observation windows through which the optical density of the biofilm was measured.

The microfluidic channel was constructed of molded polydimethylsiloxane (PDMS). The mold was fabricated by patterning 100 μm -thick Microchem SU8-50 on silicon, using contact photolithography (Appendix A, Mask #2). PDMS (Dow Corning, Sylgard 184) was prepared in a 10:1 ratio of base to curing agent, poured onto the mold, and cured at 80 °C for 20 minutes. The microfluidic channel was 500 μm wide, 100 μm

in height, and 2 cm long. Ports for interfacing the microfluidic channel to Tygon tubing were punched into the PDMS using a 2 mm dermatological punch.

The PDMS was reversibly bonded to the un-patterned side of the coverslip by soaking the side of the PDMS to be bonded in methanol for 1 minute, then aligning and placing the PDMS onto the chip. This bonding technique was found to be most effective when the PDMS was placed on the un-patterned side of the coverslip, as opposed to the chrome-coated side. Reversible bonding allowed for disassembly, cleaning, and reuse of the chip after it has been used for a biofilm formation experiment. In the development of this measurement platform and technique, reusability was a critical factor as many experiments were performed in order to characterize the system. While fabrication of the patterned coverslip and PDMS microfluidic channel were not prohibitively difficult, researcher time and resources were conserved by avoiding fabricating additional platforms through reuse.

2.1.2.2 Fluidic Interfaces

Following assembly, the platform was affixed to a glass slide for more robust handling, and the slide was aligned so that the observation windows in the coverslip were positioned over two external photodiodes sensitive to visible light. One end of the 0.38 mm ID Tygon tubing (Cole Parmer #EW-95609-14) was connected to a 1/16" barbed tubing connector (Cole Parmer #EW-06365-15) via a short section of 1/16" ID tubing (McMaster-Carr #5894K11) that snugly fit both the narrow tubing and the barbed tubing connector. Epoxy was applied to all joints to guarantee leak-free connections for maintenance of continuous and stable flow of growth media throughout a biofilm formation experiment. Connectors were inserted into the ports in the PDMS

layer, so that one tube was connected to a syringe pump and one tube was inserted in a reservoir to provide flow of growth media, bacteria, or fluorescent stain. Epoxy was again applied at the connector-PDMS interface to ensure a leak-free connection. The entire assembly was placed inside an incubator at 37 °C. A schematic of the arrayed microfluidic chips is shown in Figure 2.2, and photographs of an individual chip and platform setup are shown in Figure 2.3.

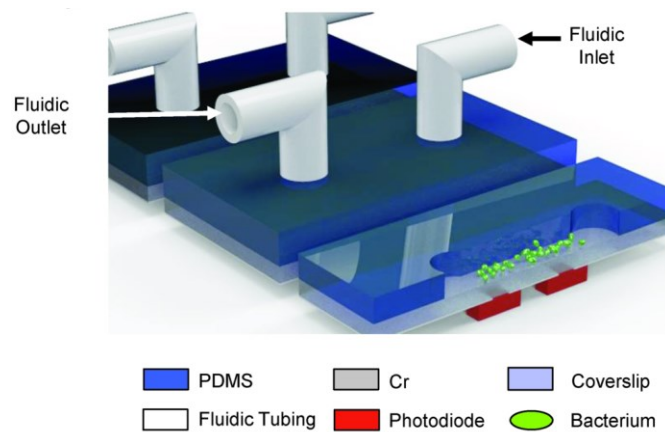


Figure 2.2. Schematic of microfluidic flow cell in which biofilms were formed. The width, length, and depth of the straight microfluidic channel used in these studies were 500 μm , 2 cm, and 100 μm , respectively. A syringe pump operating in withdrawal mode provided flow throughout the channel of suspended bacteria, growth media, or fluorescent dye from a reservoir.

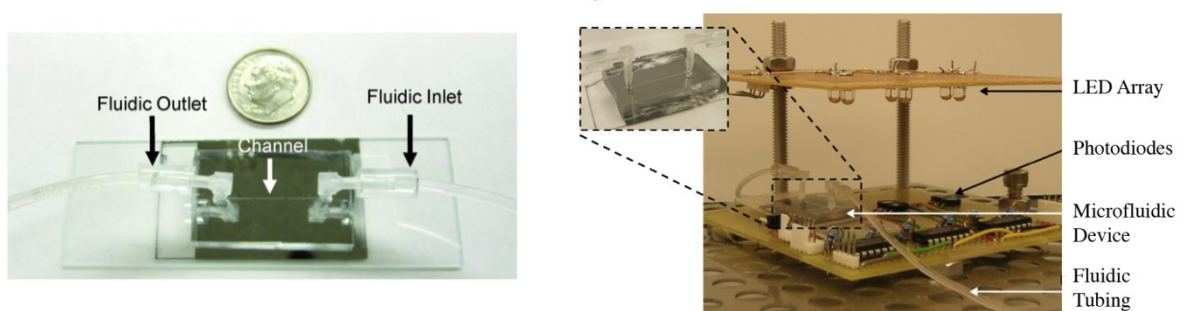


Figure 2.3. a) Photograph of assembled microfluidic device with fluidic connections b) Photograph of microfluidic device (inset) integrated with fluidic components, and positioned over photodiodes and under LEDs.

2.1.2.3 Optical Components

Optical density measurement of light transmitted through the microfluidic channel and its contents required a light source and a photodetector. In this work, an array of high intensity red LEDs (Lumex SSL-LX5093SRC/E), the source of visible light for optical density measurement, was aligned to an array of microfluidic platforms as shown in Figure 2.3b. The LEDs were connected to a 5 V voltage regulator and a dedicated power supply (Appendix B).

Two off-the-shelf photodiodes (Sharp BS520E0F) for measuring light transmitted through the microfluidic channel were placed under each microfluidic platform, with one photodiode centered under each window. As photodiodes transduce the intensity of incident light into a current, a transimpedance amplifier was used to translate the current output of each photodiode into a voltage (Appendix B). Differential voltages for each photodiode were then fed to a data acquisition (DAQ) card (National Instruments USB-6221) with LabVIEW control of inputs and outputs. Proper alignment was verified by monitoring the photodiode output during alignment.

2.1.2.4 Multiplexed Photodiode Output Measurements

In order to obtain sufficient data for statistical analysis to confirm observed trends in biofilm growth, it was necessary to perform a large number of experiments. A custom electrical logic circuit was developed to streamline simultaneous testing of up to nine devices. Evaluation of one photodiode output required differential measurement of two analog voltage inputs by the DAQ; as each device had two photodiode measurement windows, 18 analog inputs were required in order to measure nine devices. As the USB-6221 had only 16 analog inputs, a separate multiplexing circuit was constructed. As

shown below in Figure 2.4, an off-the-shelf, 4-channel differential multiplexer (Fairchild Semiconductor MM74HC4052) was used to reduce four photodiode outputs to one (Appendix B). A digital counter was created in LabVIEW and applied to the multiplexer via the digital output pins of the DAQ. The LabVIEW program was configured to record a time stamp, the state of the counter, and the photodiode outputs averaged over 5 seconds. The LabVIEW files created were processed by a MATLAB program (Appendix C) so that the multiplexed signal could be divided between the measured photodiodes according to the counter state.

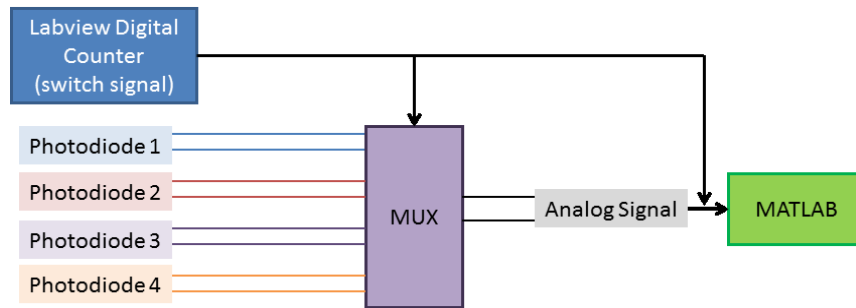


Figure 2.4. Schematic of multiplexer integration with photodiode measurement. A digital counter generated by LabVIEW controls the multiplexer state, and determines which photodiode signal is reflected in the multiplexer output. Both the multiplexer output and the state of the counter over time are exported to MATLAB, where the photodiode outputs are separated.

Key considerations with the system, especially when performing many parallel measurements, are electrical noise and interference. A common phenomenon observed with multiple analog inputs on a multiplexed-sampling DAQ card is “ghosting”, where changes in one input are observed in the adjacent input due to accumulation and transfer of charge between channels. Measures were taken to prevent ghosting as well as interference between photodiode outputs at the hardware level. “Dummy” channels were used between measurement channels on the DAQ card, so that two photodiode inputs were never read one after the other. Implementing the differential multiplexer also created more channels free for use as dummy channels.

2.1.3 Experimental Methods

2.1.3.1 Strains Used

E. coli W3110 served as the standard for biofilm formation. To probe the role of quorum sensing in optically detectable biofilm formation in microfluidics, a quorum sensing-null W3110 mutant, MDAI2 [128], was used. MDAI2 does not express LuxS, an enzyme responsible for the synthesis of AI-2, the primary signaling molecule used by *E. coli*. Restoration of quorum sensing capabilities was evaluated by adding 30 μ M AI-2 to MDAI2 cultures; growth media was refreshed every 12 hours to ensure viability of the AI-2 molecules. Bacterial cultures were grown overnight, then diluted to the desired OD₆₀₀. All cultures were grown in Luria Bertani (LB) growth media.

2.1.3.2 Validation of Optical Response of the System

The photodiode sensitivity was characterized by filling the microfluidic channel with bacterial suspensions of a known OD₆₀₀ measured with a standard spectrophotometer (Beckman Coulter, Inc.). *E. coli* W3110 suspensions were grown as described in Section 2.2.2.1, and prepared in dilutions with OD₆₀₀ values of approximately 0.1, 0.25, 0.5, 1.0, 2.0, 3.0, and 6. The microfluidic channel was disinfected with a flow of 70% ethyl alcohol. An optical density for each suspension was obtained using the developed platform by first introducing sterile LB media into the channel as a blank and measuring the photodiode response over 5 minutes (without flow in the channel). After rinsing the channel with deionized (DI) water, the suspension was injected into the channel. The photodiode response was measured over 5 minutes, followed by rinsing the channel with DI water in preparation for the next sample. Optical density values obtained with the

microfluidic platform were calculated using the average responses over the 5 minute measurement time period, and averaged between photodiodes.

2.1.3.3 *Biofilm Growth*

Prior to channel inoculation with bacteria for biofilm growth, the channel was disinfected with a flow of 70% ethyl alcohol. The bacterial suspension, diluted to an OD₆₀₀ of 0.25, was suctioned into the assembled microfluidic platform. The inoculum was incubated in the channel for 2 hours to allow bacterial adhesion to the substrate. The channel was rinsed with LB growth media for 15 minutes at a flow rate of 10 μ L/hr, corresponding to an average velocity of 0.06 mm/s, to remove non-adherent cells. The platform was continuously operated at 10 μ L/hr over the biofilm growth period.

The initial optical density of the biofilm was measured after rinsing, using the average of the two photodiode outputs over a period of 15 minutes. The photodiode outputs were then continuously monitored using the DAQ card and recorded using NI LabVIEW. Although there were two photodiodes and two measurement windows for each microfluidic channel, the outputs of the photodiodes were typically within 10% of each other; therefore, the average of the two photodiode outputs in each channel was used in all optical density calculations.

2.1.3.4 *Confocal Microscopy and Image Analysis*

While optical density is one characteristic of a biofilm, many biofilm studies evaluate morphological characteristics of the structure formed using microscopy, as discussed in Section 1.3.3.2. In this work, confocal microscopy was used to obtain morphological data that could be compared to optical density data. At timepoints selected for microscopy, flow of growth media over the biofilm was ceased. The channel

was rinsed with DI water then treated with a Live/Dead Bacterial Labeling Kit (Invitrogen # L7012). The dye was fixed by flowing 3% paraformaldehyde into the channel. Labeled samples were imaged using a confocal microscope (Zeiss LSM 710). Z-stacks were analyzed using COMSTAT to obtain morphological properties of the biofilm [8].

2.1.3.5 Calculation of Optical Density Changes

The change in optical density from the baseline biofilm condition was calculated using Equation 1. As mentioned above, the transmitted intensity $I(t)$ was continuously measured by the photodiodes, and the baseline intensity (I_0) was obtained by averaging photodiode outputs over the 15 minute period after rinsing non-adherent bacteria. As the type of photodiode used has its own conversion function between output current and incident illuminance, the transfer function was estimated from the data sheet and is reflected in Appendix C. The photodiode output currents were derived from the voltage using the resistor values used in the transimpedance amplifiers, also reflected in the calculations in Appendix C.

2.1.3.6 Data Analysis

Morphological and optical data were both reported as the average of values obtained at each of the two windows in a microfluidic channel. In some experiments, as detailed below, net changes in optical density and thickness were compared between groups at selected time points to evaluate significant differences. Since changes in optical density were continuously measured, 30 minute averages centered around the time point of interest were used as data points for comparison. Changes from the baseline

optical density and average thickness values were compared using Student's *t*-test. JMP® statistical analysis software was used for all statistical calculations.

2.1.4 Results and Discussion

2.1.4.1 System Characterization

The optical response of the system was characterized using bacterial suspensions with OD₆₀₀ values obtained with a standard spectrophotometer. A graph of the data and a linear fit thereof are presented below in Figure 2.5.

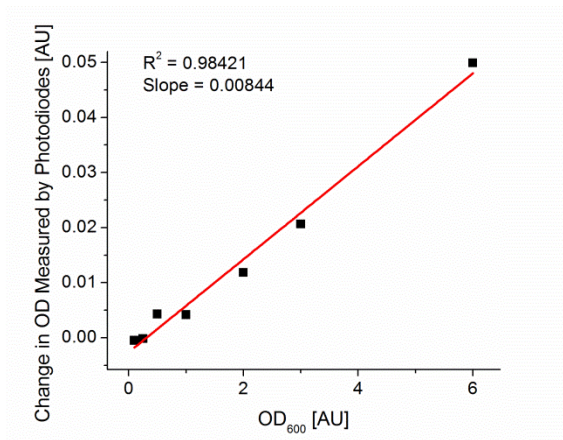


Figure 2.5. Measured changes in optical density of known bacterial suspensions using microfluidic platform with photodiodes. The photodiode output is linearly correlated to turbidity measured with a spectrophotometer.

There was a strong linear relationship ($R^2 = 0.98$) between the actual bacterial density (OD₆₀₀) and the optical density changes measured by the microfluidic platform. The data also highlighted key differences between the platform and a spectrophotometer. First, the change in optical density measured by the photodiodes maintained a linear relationship at high bacterial densities; standard spectrophotometers using traditional cuvettes with a 1 cm pathlength are known to respond nonlinearly at high OD₆₀₀ values, necessitating dilution of the sample to a measurable concentration (OD₆₀₀ < 0.5) and calculating the original optical density of the solution from that of the dilution. The

nonlinearity seen with high turbidity solutions can be attributed to the low light transmission through particularly dense suspensions, as noise will dominate a low photodetector signal. A smaller length scale will minimize the amount of light scattering through a dense suspension, fundamentally generating a dilution without manipulating the sample. Smaller length scales also typically create a higher limit of detection; while the system appeared capable of distinguishing between OD_{600} values of 0.1 and 0.25, values less than 0.1 were not tested, and the detection limit of the system was not explored. For the purposes of biofilm growth, a linear response at higher optical densities is more useful than the ability to measure very low concentrations of bacteria, as biofilms form quickly and involve higher concentrations of bacteria. Additional factors to consider are the fundamental differences between the custom microfluidic platform and a spectrophotometer. In addition to the different optical pathlengths, the LED array produces a wide range of optical wavelengths (a band of spectrum typically greater than 20 nm wide), while the laser in a spectrophotometer produces a very narrow spectrum (typically less than 3 nm). Furthermore, when measuring the optical density of a biofilm formed in the custom microfluidic platform, not only does the number of bacteria contribute to optical density, but incident light is also scattered by the biofilm-media interface. While there are a number of differences between the microfluidic platform and a traditional spectrophotometer that impede direct comparison between the two methods, it is useful to have an approximate correlation between the techniques for comparing results from the microfluidic platform to those from standard biofilm studies. Additionally, such a correlation enables inexpensive, commercial off-the-shelf optical components to replace a more expensive spectrophotometer for optical density

measurement. While a spectrophotometer is expected to have a higher degree of sensitivity due to its lower noise level, the LED and photodiodes are simple to implement and can be integrated with a variety of form factors beyond cuvettes and microwell plates.

Small differences were evident in the outputs of two photodiodes positioned at different locations within the microfluidic channel; an example of this is provided in Figure 2.6a. In this case, the output at the first window, closest to the inlet, showed more aberrations than the output of the second window. In other cases, such differences between photodiode outputs were not as apparent, as shown in Figure 2.6b, indicating that, at least in this work, firm conclusions with regard to repeatability in changes in biofilm properties along the length of the channel cannot be drawn.

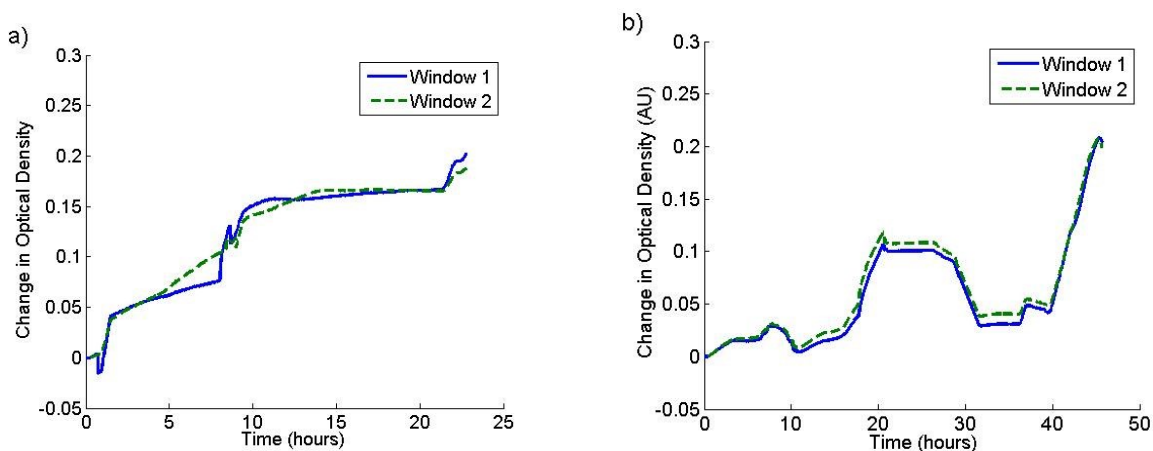


Figure 2.6. Raw optical density change measurements corresponding to the output of the two photodiodes positioned under one microfluidic channel. ‘Window 1’ is closest to the channel inlet. Data correspond to two separate *E. coli* W3110 experiments. a) Outputs differ along the length of the channel, as seen difference in photodiode outputs between 5 and 12 hours; the greatest difference between outputs is 31%. b) Outputs show almost identical behavior with less than a 10% difference between measurement locations.

When evaluating the average output of the two photodiodes, it was observed that the biofilm optical density exhibits unpredictable sharp increases and decreases, as shown in Figure 2.7a. These ‘spikes’ reflect optical density changes faster than the doubling rate

of *E. coli* (< 10 minutes versus 20 minutes), and therefore cannot be attributed simply to natural bacterial growth. It was hypothesized that this was due to both the non-uniform nature of the biofilms grown in the channel and the additional dynamics provided by the flow environment. If a section of biofilm is sheared off, it can either reattach elsewhere along the channel, or exit the flow cell with waste growth media. The location from which it was sheared off will exhibit a sharp decrease in biomass, and if redeposited, the location to which it adheres will exhibit a sharp increase in biomass. If both detachment and reattachment locations were positioned over observation windows, there would be no observed change in average biofilm optical density, as the optical densities were averaged between photodiodes and over a period of 5 seconds. However, if only one of these locations is positioned over a window, either a sharp increase or decrease in optical density will be observed, dependent on if the window observed attachment or detachment, respectively.

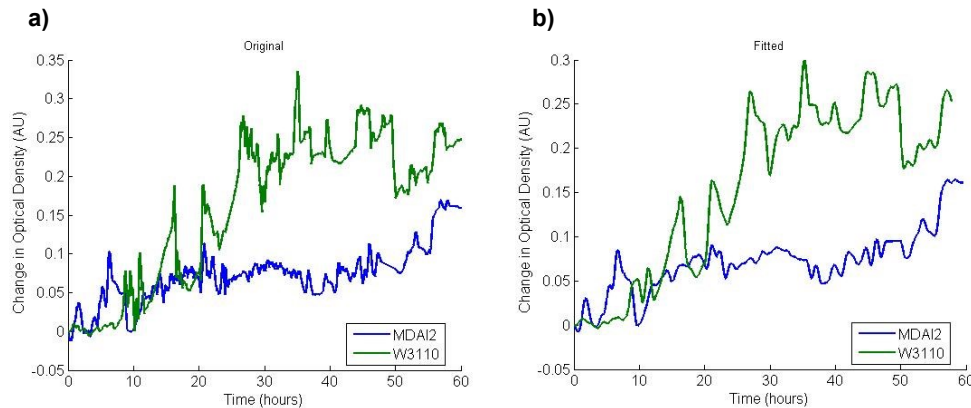


Figure 2.7. Data corresponding to *E. coli* W3110 and MDAI2 biofilms formed in two microfluidic platforms. a) Raw optical density change measurements, illustrating unpredictable “spikes” in observed optical density b) Data from (a) smoothed using quadratic fits (Appendix C).

In order to obtain a representative picture of the biofilm as a whole, as a biofilm is by definition a bulk phenomenon, data was either smoothed using quadratic fits (Figure 2.7b, Appendix C), or evaluated only at the endpoint of growth. While much data is lost,

elimination of this noise provides an adequate representation of the overall biofilm. Further analysis of the raw data, combined with other evaluation methods such as continuous microscopy, can further elucidate the roots of the observed fluctuations.

2.1.4.2 *Biofilm Sensitivity to Shear Stress*

One of the unique capabilities of this platform is real-time observation of the biofilm state without the bulk and expense of confocal microscopy. This capacity was demonstrated through an experiment evaluating biofilms during exposure to shear stress. As biofilm thickness depends on the shear stress experienced by the biofilm (see Section 1.3.1.2), the response of the biofilm to shear stress is reflected in its overall biomass, and consequently, its optical density.

Biofilms were prepared according to the procedures of Section 2.1.2.3, using *E. coli* strains W3110 and MDAI2, and grown for 48 hours. At this point in time, the flow rate was increased to 400 $\mu\text{L/hr}$ for 30 minutes, then returned to the initial flow rate of 10 $\mu\text{L/hr}$. Results of the high shear rinsing studies are shown in Figure 2.8.

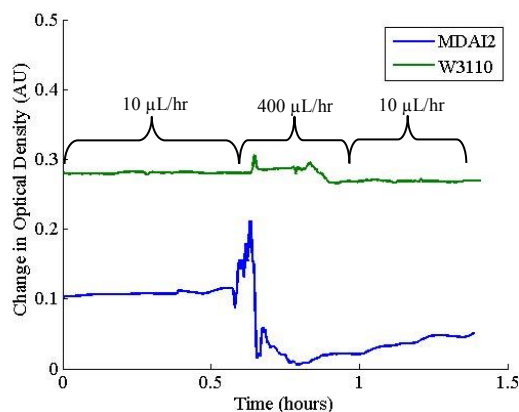


Figure 2.8. Rinsing of *E. coli* W3110 and MDAI2 biofilms measured by the change in optical density. Data indicate the role of quorum sensing in physical robustness of biofilms.

The continuous optical density measurements showed the biofilm sensitivity to shear imposed on the biofilms, emphasizing the real-time observation capability of the platform and measurement system. Using two different strains of bacteria, one wild-type (*E. coli* W3110) and one deficient in quorum sensing (*E. coli* MDAI2), the role of quorum sensing in the mechanical stability of the resulting biofilm was highlighted. The wild-type biofilm exhibited little change in optical density after rinsing, and during the rinsing period, fluctuations of less than 10% with respect to the initial optical density were observed. In contrast, the *E. coli* MDAI2 biofilm exhibited sharp and erratic changes during the rinsing period and a larger overall change in optical density after rinsing as compared to before rinsing. This is most likely due to the lack of exopolysaccharide production in quorum sensing-deficient strains of bacteria [5, 129]; the absence of a sufficient extracellular matrix may reduce biofilm cohesion and render the structure more susceptible to external forces, such as those imposed by fluid shear in the microfluidic channel.

2.1.4.3 Evaluation of Biofilm Optical Density over Repeated Experiments

Building upon the capacity of the developed platform for optical observation of biofilms, a set of more extensive studies of the optical density of biofilms was performed. Characterization of biofilm optical density growth curves and correlation of optical properties to morphological properties of the biofilm confirmed the applicability of the platform for scientific biofilm studies. Here, the dependence of *E. coli* biofilm formation on quorum sensing was explored using the microfluidic platform for optical density monitoring.

In each experiment, three platforms were arrayed in parallel; one was inoculated with wild-type *E. coli* W3110, and two with MDAI2. While LB media was flowed through all of the channels during growth, one of the channels inoculated with MDAI2 was exposed to LB media with 30 μ M AI-2. During the operation of an experiment, the growth medium was refreshed every 12 hours for all biofilms to ensure viability of the AI-2 molecules and to maintain parallelism between concurrent experiments. The optical density of biofilms contained in all three channels was continuously measured. The three types of biofilms were grown for time periods of 12, 24, 36, 48, 60, or 72 hours, with $n = 3$ for each type of biofilm and for each growth period. The biofilm optical density states at the end of each growth period were compared using a 30 minute average to provide a single value for comparison.

The averages of optical density results from repeated experiments are shown in Figure 2.9. The optical absorbance of the biofilms was shown to vary with respect to the degree of intercellular communication. Wild-type biofilms exhibited an initial period of rapid growth within the first 12 hours of flow, while MDAI2 biofilms grown with and without extracellular AI-2 showed more gradual increases in optical density. The different types of biofilms exhibited different overall changes in optical density; wild-type biofilms were the most optically dense, while *luxS*-null biofilms were the least optically dense. AI-2 addition appears to restore optical density to MDAI2 biofilms; this is reflected by the compiled data shown in Figure 2.9, where the mean optical density change of MDAI2 biofilms grown with AI-2 was approximately equal to wild-type biofilm optical density changes after 48 hours. Restoration of the biofilm optical density phenotype by addition of AI-2 confirms the dependence of the biofilm formation on AI-2

within the system. Optical density for all three types of biofilms observed also appeared to continue to increase at 72 hours and did not approach a steady-state value.

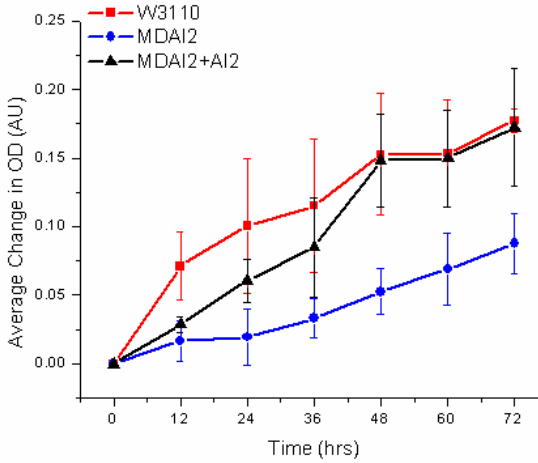


Figure 2.9. Compiled data for the change from baseline optical density for each type of *E. coli* biofilm formed. $n = 3$ for each data point, presented as the average of all trials. Error bars correspond to one standard deviation of the trials.

When evaluating the statistical significance of the differences between time points within one strain and between types of biofilms, the magnitude of optical changes over growth was not consistent between experiments, reflected in the overlapping error bars in Figure 2.9. However, the relative differences between strains were more consistent between experiments. Wild-type biofilms were consistently the most optically dense, MDAI2 biofilms were the least dense, and by adding AI-2 to the latter, density could be restored. The percent difference between wild-type biofilms and MDAI2 biofilms grown with or without AI-2 was expressed as

$$\% \text{ Difference} = 100 \times \frac{OD_w - OD_x}{OD_w},$$

using the optical density change of the wild-type biofilm (OD_w) as a reference for the optical density change of MDAI2 grown with or without AI-2 (OD_x). Comparison of the

percent difference from wild-type biofilms yielded more statistically significant differences between biofilm types (Figure 2.10, Table 2.1).

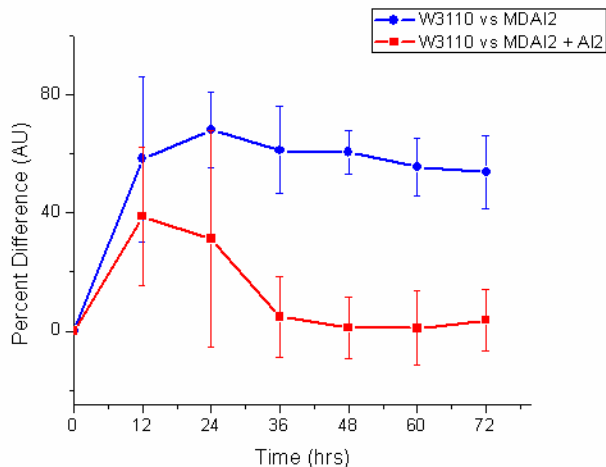


Figure 2.10. Compiled data for the percent difference from wild-type (W3110) biofilms for MDAI2 biofilms (blue circles) and for MDAI2 biofilms grown with AI-2 (red squares). Error bars represent one standard deviation of the averaged data.

Table 2.1. Table of *p*-values obtained through Student's *t*-test for comparison of optical density change magnitude and for comparison of percent difference in optical density change between *E. coli* biofilm groups.

	12 h	24 h	36 h	48 h	60 h	72 h
W3110 versus MDAI2	0.0076	0.0129	0.0362	0.0108	0.0224	0.0510
W3110 versus MDAI2 + AI-2	0.0547	0.1383	0.8478	0.8833	0.9043	0.8713
MDAI2+ AI-2 versus MDAI2	0.1695	0.1247	0.0474	0.0129	0.0264	0.0586
% Difference W3110/MDAI2 versus % difference W3110/MDAI2+AI-2	0.4067	0.1755	0.0084	0.0017	0.0146	0.0768

Differences are considered significant for $p < 0.05$; comparison of strains via percent difference from wild-type biofilms yields more statistically significant differences.

2.1.4.4 Evaluation of Biofilm Morphology over Repeated Experiments

In order to compare optical density studies to traditional morphological studies, the physical nature of the biofilms formed in the microfluidic platform were interpreted through confocal imaging and analysis of image stacks. Using the output of COMSTAT, the mean biofilm thickness and roughness coefficient were also averaged between sets, shown in Figure 2.11a and Figure 2.11b respectively.

Over the windows imaged using confocal microscopy, the variances in thickness differed to a large extent. In some cases where a thick biofilm did not cover the majority of the window, the standard deviation of the thickness could be as much as 100% of the average biofilm thickness. An alternative metric for examining the spatial non-uniformity of the biofilms formed is the roughness coefficient, as defined by Heydorn et al. and evaluated using COMSTAT [95]. This parameter is a dimensionless number representative of the percent variation in biofilm thickness. As roughness coefficient trends within one channel were variable, as with the optical density, the values for all windows measured for one type of biofilm at one time point were averaged. Results, shown in Figure 2.11b, indicated a large degree of variability between channels and a lack of significant differences between types of biofilms. The results suggest that biofilm roughness has a minimal dependence on bacterial quorum sensing activity, although wild-type *E. coli* biofilms appeared to have average roughness values lower than those of the other two types of biofilms investigated, especially after 60 hours of growth. Additionally, the variation in the roughness coefficient, indicated by the error bars in Figure 2.11b, was smallest for all three groups at 72 hours. This may be indicative of an approach to a steady-state biofilm as the biofilm structure settles to a smooth surface that will not be as prone to sloughing.

The average thickness of the biofilms also showed the same overall trend as the changes in biofilm optical density (Figure 2.11a). As with the trends in optical density, wild-type biofilms were the thickest, MDAI2 biofilms were the thinnest, and addition of AI-2 to the latter produced MDAI2 biofilms with thickness approaching that of wild-type biofilms. The thicknesses of all the biofilms increased over time, with the most

significant increases occurring between 36 and 48 hours in W3110 biofilms and MDAI2 biofilms grown with AI-2. Thicknesses of biofilms (Figure 2.11a, Table 2.2) showed less irreproducibility over different experiments than the optical measurements (Figure 2.9) and roughness coefficient calculations (Figure 2.11b) for the same biofilms.

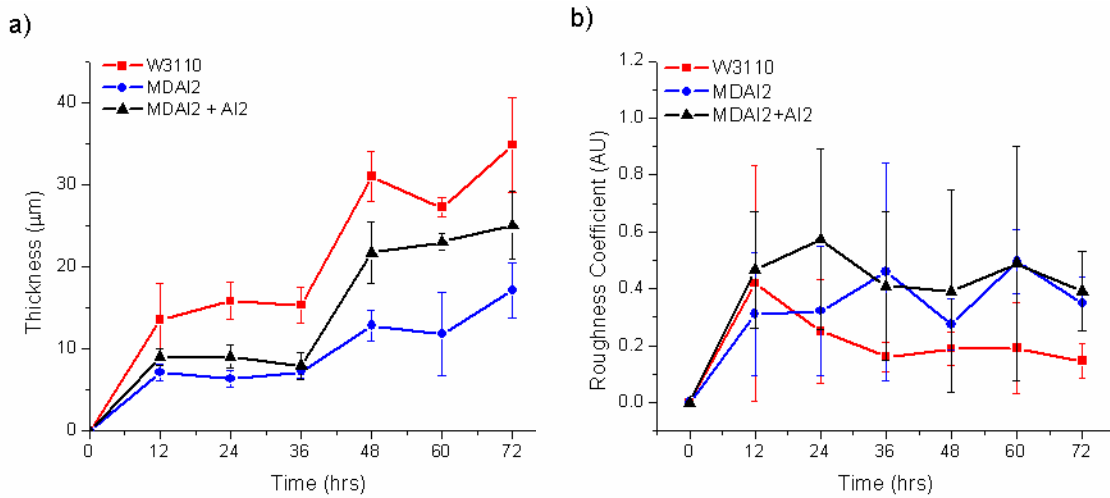


Figure 2.11. Compiled morphological data, including a) average thickness, and b) nondimensional roughness coefficient, for each type of biofilm formed. $n = 3$ for each data point, presented as the average of all trials. Error bars represent one standard deviation of the averaged data.

Table 2.2. Table of p -values obtained through Student's t -test for comparison of thickness between *E. coli* biofilm groups.

	12 h	24 h	36 h	48 h	60 h	72 h
W3110 versus MDAI2	0.0271	0.0004	0.0010	0.0003	0.0008	0.0030
W3110 versus MDAI2 + AI-2	0.0868	0.0024	0.0015	0.0088	0.0040	0.0380
MDAI2+ AI-2 versus MDAI2	0.4218	0.0973	0.6558	0.0108	0.1456	0.0748

Differences are considered significant for $p < 0.05$; comparison of strains via percent difference from wild-type biofilms yields more statistically significant differences.

Both W3110 and MDAI2 formed optically detectable biofilms. While MDAI2 is incapable of synthesizing AI-2 due to the lack of *luxS* expression, formation of biofilms by MDAI2 still occurred, albeit not as efficiently as formation of wild-type biofilms. This agreed with the work of other groups, who have found that while biofilm formation may be encouraged by quorum sensing, in the absence of quorum sensing bacteria may still form thin, sparse biofilms [56].

Addition of AI-2 appeared to restore optical density and thickness to MDAI2 biofilms so that these characteristics approached those of the wild-type biofilms. However, the onset of the restoration was not immediate, as shown in the optical data. It is possible that the concentration of AI-2 used in these studies (30 μM) combined with the flow properties in microfluidics may not be sufficient to immediately restore wild-type behavior. While 20 μM of extracellular AI-2 has produced quorum sensing activity in suspended cultures of MDAI2 [130], the dynamics of the microfluidic reactor may require higher concentrations of AI-2 in the growth media.

While the concentration of AI-2 throughout the media is assumed to be uniform at the channel inlet, laminar flow around the biofilm structure and bacterial uptake of AI-2 will produce a non-uniform concentration profile throughout the channel. Unlike the suspensions of MDAI2, the physical structure of the biofilm will also impede transport of AI-2 through the biofilm to bacteria at the substrate interface. Therefore, AI-2 concentrations that may restore quorum sensing activity in a suspended culture of MDAI2 may not produce the same activity in an MDAI2 biofilm formed in a microfluidic flow environment. However, the microfluidic device is more clinically relevant than bacterial suspensions – not only can biofilms be formed in microfluidics, but biofilms can be grown with a continuous supply of fresh nutrients, similar to *in vivo* environments with flow of fluids containing a variety of metabolites. In microscale environments within both microfluidic and *in vivo* spaces, the dynamics of flow and exposure of the biofilm to molecules within the flow are expected to vary significantly with dimensions of the growth space. For future studies using AI-2 or pharmaceutical

agents for treating biofilms, the dimensions of the microfluidic reactor must be accounted for when translating work between studies.

The changes in biofilm optical density from recorded baseline values for all three types of biofilms investigated appeared to continue increasing steadily at the end of the selected growth period of 72 hours. Conversely, biofilm thicknesses did not appear to exhibit any distinct increase toward the end of the growth period; while longer experiments must be performed in order to confirm or reject the achievement of steady-state thickness in biofilms by 72 hours, it was inferred that the optical density of a biofilm is a unique characteristic, independent of its thickness. While biofilms may achieve a steady-state thickness, the structure may continue to reorganize itself over time, contributing to increased optical density. These results correspond with those of Bakke et al. at the macroscale, in that a morphological steady state was achieved more quickly than an optical steady state [14].

Biofilm thickness did not approach a distinct steady state within the allotted 72 hour time period. However, with a longer experimental duration, it is expected that a steady-state thickness would be reached. The attainment of a steady state is expected given the bacterial growth behaviors observed in macroscale settings. When bacteria are grown in any type of reactor, the growth rate is dependent on nutrient availability. In suspension or in static reactors such as a microwell plate, the amount of growth media and nutrients is fixed; therefore, as metabolites are depleted, the bacteria will reach a stationary phase and, given further time, will begin to die [131]. In a flow reactor, there is a continuous supply of fresh nutrients, encouraging continuous and efficient bacterial growth. However, as the biofilm forms on the bottom of the channel, the availability of

nutrients to the bacteria at the substratum becomes limited by diffusion through the upper portion of the biofilm, causing the growth rate to slow and eventually approach a steady state as a balance is achieved between thickness and nutrient diffusion. Biofilm thickness is also limited by the shear stress imposed on the biofilm surface, since high amounts of shear will cause bacterial shedding. This limiting effect is particularly pronounced in a microfluidic environment such as that constructed in this work; the small dimensions of the channel (100 μm deep) create an environment where as the biofilm grows to thicknesses of tens of microns, the biofilm itself affects the flow by decreasing the effective diameter of the microfluidic channel and thereby increasing shear stress. Through a negative feedback system, the bacteria will consume nutrients and divide in order to sustain the population but will maintain a thickness small enough for unimpeded flow through the channel (i.e. the channel does not become clogged with biofilm) [32]. The combination of biological and physical phenomena is expected to produce the eventual steady-state thickness suggested by the data in Figure 2.11a.

While additional experiments with longer time durations will clarify the dynamics of biofilm formation, it must also be acknowledged that the earlier time points are of particular interest. In terms of the ultimate application of this platform for evaluation of drugs for biofilm prevention and eradication, focusing on early biofilm growth is of particular importance for prevention of serious biofilm infection. Therefore, while it is of scientific interest to continue biofilm growth experiments for longer periods of time, such as the weeks-long experiments performed by Bakke et al. [14], if this platform were to be applied toward drug discovery and evaluation, long-term experiments are not essential.

2.1.4.5 Evaluation of the relationship between biofilm thickness and optical density

Although it appeared that the relationship between biofilm morphology and optical density is not direct, especially considering the differing time scales of steady-state approach, the likelihood of a relationship between the two was statistically investigated. A linear correlation between the values for endpoint optical density and biofilm thickness (Figure 2.9 and Figure 2.11) yielded a correlation coefficient of 0.78. Considering the large number data points used to obtain this correlation ($n = 54$), this degree of correlation is significant and implies a strong association between the two variables. While thickness and optical density are expected to be independent, a linear fit was generated using optical density as an independent variable and biofilm thickness at that time point as a dependent variable. As shown in Figure 2.12, a linear fit of the thickness with respect to change in optical density yielded an r -squared of 0.9; due to the clustering of data at low optical density and thickness values, an intercept was imposed on the data, allowing for an improved fit. Note that while the fit is improved, it is not directly physically relevant; here, at the onset of the experiment the thickness is predicted to be 6 μm . The actual average thickness is expected to be much lower ($< 1 \mu\text{m}$), as the inoculum OD_{600} of 0.25 will not cover the entire floor of the microfluidic channel, and each cell will be less than 2 μm in height. Further experimentation, especially at shorter time points, is expected to improve this fit.

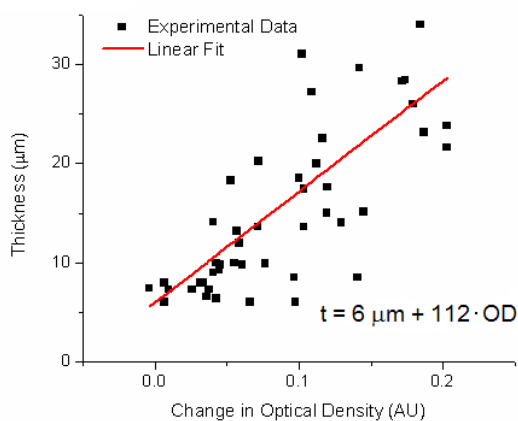


Figure 2.12. Least-squares regression fit of biofilm thickness (t) versus change in optical density (OD), compiled for all biofilms at all timepoints observed. $R^2 = 0.90198$.

The uncertainty of the change in optical density measurement is dependent on a number of factors, including errors introduced by the inherent properties of the measurement equipment, such as the photodiodes (dark current), data acquisition unit (analog input accuracy), and the measurement circuitry (offset introduced by the transimpedance amplifier). As an example, data were used from the endpoint of an immature biofilm with a final optical density change of 0.01; this represents the minimum relevant change in optical density to be measured and is also the point where the most uncertainty will be introduced. From the components of error and using the assumed biofilm, the experimental uncertainty evaluated as outlined in [132] was approximately 0.06% of the overall change in optical density. Note that this uncertainty does not account for natural variations in bacterial systems, and therefore the large variations in the data obtained in this work are most likely due to biological fluctuations. In order to minimize this uncertainty, it would be ideal to perform more repetitions of the experiments to determine the trends in optical density and morphological changes during biofilm formation; this would additionally aid in the refinement of a model of biofilm optical density versus thickness.

Inclusion of other variables in the optical density model, such as substratum coverage and biomass, may produce an improved fit. However, the objective is ultimately to utilize measurement of changes in optical density as a substitute for microscopic measurement of biofilm bulk properties. The refinement of the simplified thickness versus optical density model eliminates the need for corroboration of optical density results using imaging to obtain morphological properties and would be instrumental in development of a completely integrated microfluidic platform for real-time biofilm monitoring.

2.1.5 Conclusion

This section described the development of the first microfluidic platform utilizing optical density monitoring to assess biofilm formation. Optical density measurement is continuous and noninvasive, capable of providing real-time information on biofilm state while preserving the biofilm throughout growth. Due to their ease of implementation and low cost, multiple platforms were arrayed in parallel allowing for simultaneous experiments. The devices and measurement methodology were used to evaluate differences in biofilms formed under varying degrees of quorum sensing activity. The influence of quorum sensing on physical stability of biofilms was evaluated by monitoring optical density while imposing a high shear rate on the biofilms. Biofilm growth evaluated via the change in optical density was also compared to the thickness measured via confocal microscopy. Biofilms formed by *E. coli* incapable of quorum sensing molecule synthesis were less optically dense, thinner, and covered less surface area than wild-type biofilms. Addition of quorum sensing molecules partially restored wild-type biofilm characteristics to non-communicating bacteria. While the optical

density changes of each biofilm were shown to be quite variable, relative optical differences between different types of biofilms showed more reproducibility. A linear fit was used as a preliminary model for relating observed optical density changes to biofilm thickness. With further experimentation, this model will allow for replacement of microscopy with continuous, non-invasive biofilm evaluation via optical density measurement.

2.2 Second Generation Device

The platform and results presented in Section 2.1 demonstrated that optical density can be used for biofilm monitoring. However, a number of questions were raised by the results, particularly when examining variability in the raw data. Some temporal aberrations may be attributed to biofilm sloughing, where segments of biofilm may detach and exit the microfluidic channel, decreasing the average amount of biofilm in addition to locally decreasing the biomass at the location from which the segment detached. Alternatively, these segments may be deposited elsewhere in the channel and continue to grow in the new location; in this situation, the local biomass at the origin of the segment decreases, but the average biomass within the channel is unchanged. These two scenarios are significantly different, especially when evaluating an anti-biofilm treatment – a permanent decrease in total biomass indicates an effective treatment, while sloughing and re-deposition elsewhere in the channel indicates no change in the average biofilm state. In a platform with only two observation windows, it is impossible to differentiate between these two scenarios if all that is observed is a local decrease in biomass.

In order to distinguish local changes from overall changes in biofilm, a platform with the capability of observing the entire microfluidic channel is required. Considering this need, the platform presented in Section 2.1 was redesigned to replace the two individual photodiodes with a charge coupled device (CCD), essentially a linear array of photodiodes extending over the length of the microfluidic channel. The CCD provided the capability of obtaining local optical information from each point in the array; the information obtained over the array was also averaged to reflect the overall biofilm state. The instrumentation, integration, and testing of the CCD with biofilm formation in a microfluidic channel was performed by Mr. Matthew Mosteller [126] as an extension of my development of the initial platform as summarized previously.

2.2.1 Platform Design

While an overview of the CCD-based microfluidic biofilm measurement platform and its implementation is presented here, specifics of the hardware and software involved therein are discussed in detail elsewhere [126].

In general, the CCD-based measurement platform was similar in structure to that of the first generation platform, with a microfluidic channel placed on top of a transparent base with a patterned observation window aligned to a photodetector. The CCD used included a 128 x 1 linear array of photosensitive pixels, with each pixel measuring 120 x 70 μm . The array was positioned under a PDMS microfluidic channel temporarily bonded to a transparent substrate (500 μm -thick Pyrex®). As in the first-generation device, CCD alignment to the channel and the LED light source was aided by metal (20 nm Cr under 200 nm Cr/Au) patterned on the transparent substrate. In addition to defining the observation windows, the patterned metal was also used to apply electric

fields to biofilms for bioelectric effect studies. Channels and CCDs were arrayed in parallel, as shown in Figure 2.13.

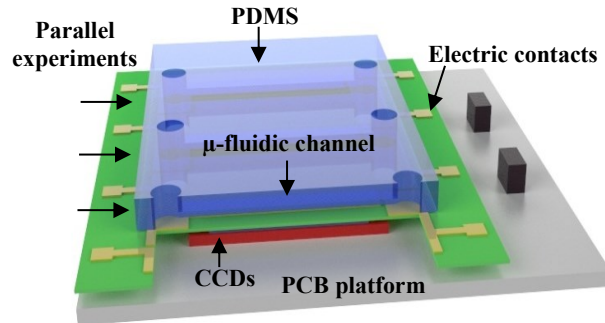


Figure 2.13. Schematic of the CCD-based microfluidic biofilm observation platform. A printed circuit board (PCB) served as a foundation for circuitry and electrical connections. An array of microfluidic channels patterned in PDMS was placed on top of a transparent substrate and aligned to the underlying CCD array. The platform depicted here also included electrodes patterned on the transparent substrate for applying an electric field to biofilms during growth. Modified from [133].

As in assembly and testing of the first generation device, arrayed microfluidic channels and measurement circuitry were aligned to a light source and placed in an incubator maintained at 37 °C (Figure 2.14). In this case, incident light for performing the optical density measurements was provided by an LED panel generating diffuse, red light.

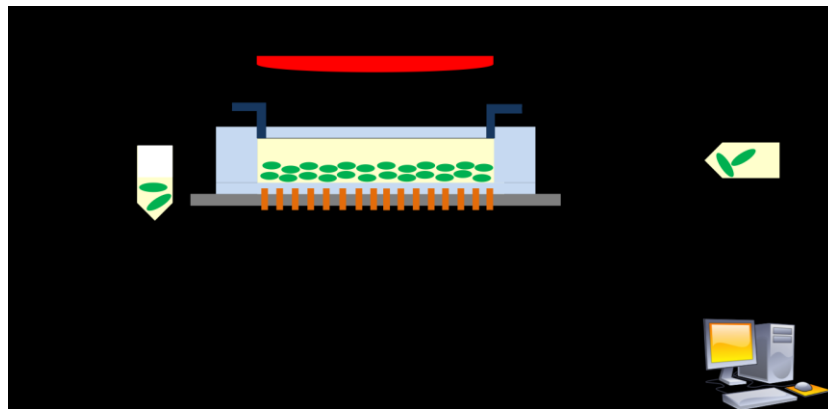


Figure 2.14. Schematic of experimental setup for CCD-based microfluidic biofilm observation platform. The CCD array, microfluidic channel, and samples to be introduced into the channel were contained in a 37 °C incubator. A syringe pump operating in withdrawal mode created sample flow in the microfluidic channels. External power supplies and function generators enabled actuation of the CCD sensors, while a DAQ card and PC were used to obtain and analyze optical density measurements. Reproduced from [126].

The platform was used for biofilm studies using methodologies similar to those in Section 2.1.2. After inoculation of the channels with a bacterial suspension, continuous flow of LB was applied during biofilm formation while optical density signals were continuously recorded.

2.2.2 Results and Discussion

The effectiveness of the CCD setup in providing details on spatiotemporal events in the microfluidic channel was demonstrated by flowing optically dense droplets (water dyed with food coloring with an $OD_{600} \sim 45$) in a transparent fluid (mineral oil) through the channel. The average response of the CCD array, shown in Figure 2.15a, showed a series of peaks in optical density as droplets were introduced into and left the channel. Separating the average signal into the individual signals from each pixel in the array (Figure 2.15b) illustrated how pixels close to the entrance of the channel (position = 0 mm) measured the optical density increase of the droplet before pixels at the opposite end of the channel, the movement of the optical density peak down the position axis of the plot reflecting the movement of the droplet down the channel.

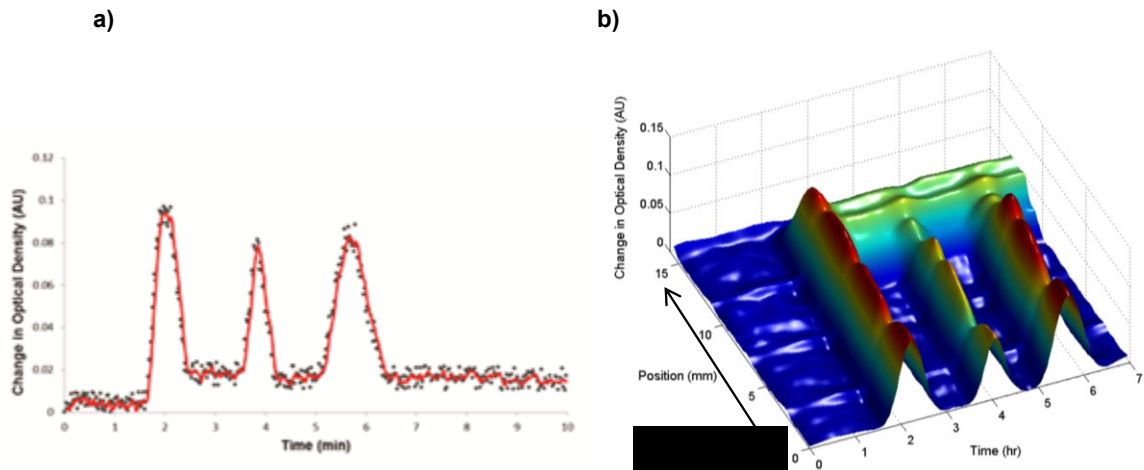


Figure 2.15. Demonstration of spatiotemporal optical density monitoring in the CCD-based microfluidic biofilm observation platform using flow of optically dense droplets in transparent mineral oil. (a) Average change in optical density within one microfluidic chamber of the CCD-based biofilm measurement platform during droplet flow. (b) Spatiotemporal detection of droplet flow within the same microfluidic channel. Reproduced from [126].

The same measurement methods used for droplet observation were expanded toward evaluating bacterial biofilm growth along the microfluidic channel. Figure 2.16 shows a sample spatiotemporal plot of biofilm growth, highlighting what were possibly a stationary biofilm segment (Figure 2.16a) and a segment of biofilm translocating down the channel over time (Figure 2.16b). While the data shown in Figure 2.16 were not obtained from an untreated wild-type *E. coli* biofilm but one treated with an electric field during growth, the principles of spatiotemporal biofilm observation were clearly demonstrated.

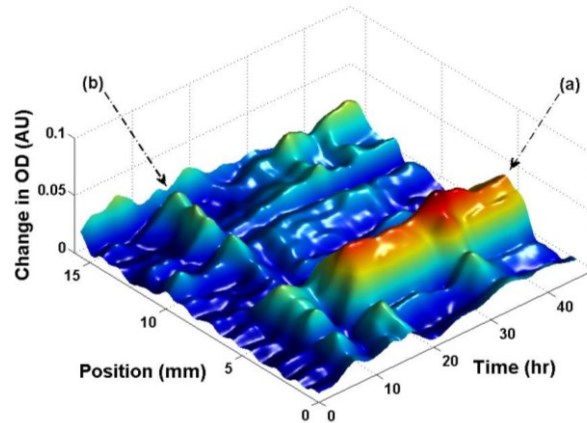


Figure 2.16. Surface reconstruction of biofilm surface morphology showing (a) stationary biofilm and (b) biofilm drifting through the channel with time. The surface reconstruction as created using the spatiotemporal data from optical density measurement using the CCD-based biofilm measurement system. This particular plot is from a biofilm sample treated with an electric field. Reproduced from [126].

2.2.3 Conclusion

This section demonstrated the expansion of microfluidic biofilm optical density measurement into a format allowing higher spatiotemporal resolution of biofilm measurements. Incorporation of a CCD array into a microfluidic biofilm formation platform not only provided average optical density measurements over the entire microfluidic channel, but through the resolution provided by an array of photosensitive pixels, was also able to provide insight into changes in the biofilm structure. The ability to differentiate localized growth, detachment, and reattachment of biofilm in an integrated manner further advances the technique of optical density monitoring as a viable option for biofilm study.

2.3 Chapter Summary

This chapter covered the development of optical density monitoring as a measurement technique for evaluation of bacterial biofilm growth in a microfluidic environment. The platforms developed through this work include the first, proof-of-concept device delivering general information as to biofilm state, and the expansion of

this device to provide spatiotemporal details of biofilm dynamics. Microfluidic biofilm reactors provide tight environmental control and small sample volumes, in addition to the ability of fabrication and parallel integration with optical measurement components at low cost. These capabilities not only can be leveraged for scientific characterization of biofilms, as presented in this chapter, but also can be applied toward evaluating new anti-biofilm treatments, as presented in the next chapter.

3 Evaluating Effects of Quorum Sensing Inhibitors on Biofilm Formation

This chapter will cover the application of the first-generation biofilm optical measurement platform developed in Chapter 2 for evaluating the effect of quorum sensing inhibitors (QSIs) on biofilm formation. First, one such QSI, isobutyl-DPD, was demonstrated to inhibit the maturation of *Escherichia coli* biofilms grown in microfluidics. Using optical density monitoring, it was shown that a combinatorial approach wherein isobutyl-DPD was used with near-MIC levels of the antibiotic gentamicin produced near complete clearance of pre-existing *E. coli* biofilms. Similarly, another AI-2 analog, phenyl-DPD, also applied in combination with gentamicin, resulted in clearance of preformed *Pseudomonas aeruginosa* biofilms.

As antibiotic-tolerant persister cells are a major contributor to the tenacity of biofilm infections, studies were performed to investigate a potential link between the biofilm inhibition and clearance instigated by QSIs, and the incidence of persister cells. The results of this investigation suggested that QSI administration to a bacterial culture has no significant effect on persister cell formation, although future investigation is warranted. The work in this chapter was performed in conjunction with Dr. Varnika Roy as an equal contributor. The majority of Section 3.1 has also been published in Applied Microbiology and Biotechnology with Dr. Varnika Roy as a co-first author [119].

3.1 Evaluation of Quorum Sensing Inhibitors using Microfluidic Platform with Optical Monitoring

The inhibitory effects of the QSIs studied were evaluated in two biofilm growth scenarios: application from the beginning of growth, and application to a preformed

biofilm after maturation. The former demonstrated efficacy in biofilm prevention, and the latter demonstrated efficacy in clearing biofilms. While the microfluidic platform provided dynamic, real-time measurements of biofilm density, studies were also performed in a microfluidic channel on an unpatterned glass coverslip (i.e. no observation windows patterned in chrome as in Section 2.1). While the unpatterned substrate precluded real-time optical density measurement, it allowed more detailed confocal microscopy studies that provided strong physical evidence of biofilm clearance. The combination of biofilm evaluation methods and growth scenarios produced detailed proof that the AI-2 based QSIs studied not only reduce biofilms, but also can potentiate the biofilm-clearing efficacy of traditional antibiotics.

3.1.1 Methods

3.1.1.1 Microfluidic Device Fabrication and Assembly

Fabrication of the microfluidic platform was described in [118] and is also presented in Section 2.1.1; it is summarized again here. The base of the device was a coverslip, a transparent substrate thin enough for high resolution inverted confocal microscopy. For experiments with continuously measured optical density, coverslips were patterned with two observation windows in chrome (see Appendix A, Mask #1) to allow alignment of windows with embedded optics. In experiments where confocal microscopy alone was used to evaluate biofilms formed throughout the channel (7 points in each channel were imaged), the coverslips were uncoated. Although the elimination of the two windows precluded measurement of optical density using the methods of Chapter 2, the information gained with confocal microscopy at more than two locations within the

channel provided more certainty in evaluating biofilm knockdown by a new QSI. Optical density data was then used to corroborate these confocal microscopy results.

The microfluidic channel itself consisted of polydimethylsiloxane (PDMS) molded by photopatterned Microchem SU8-50 (Appendix A, Mask #2). Here, the mold produced microfluidic channels 100 μm deep, 500 μm wide, and 2 cm long. Ports for interfacing the channel to fluidic tubing were punched into the PDMS using a 2 mm dermatological punch. The PDMS was reversibly adhered to the coverslip by soaking the bonded side of the PDMS in methanol for 1 minute, then aligning and placing the section of PDMS over the coverslip.

3.1.1.2 Biofilm Formation

Biofilms were formed either by *E. coli* K-12 MG1655 ATCC #47076, or by *P. aeruginosa* PAO1. For both strains, overnight cultures were diluted to an OD_{600} of 0.25, introduced into the microfluidic channel, and incubated with no flow at 37 °C for 2 hours. Luria Bertani (LB) growth medium was then continuously suctioned from a microcentrifuge tube reservoir into the device at a rate of 10 $\mu\text{L/hr}$. As needed, this medium was supplemented with various concentrations of analog or antibiotic at specified times. In studies of biofilm inhibition, after 2 hours of cell incubation, the analog diluted in LB medium was flown into the microfluidic channel for 48 hours at 10 $\mu\text{L/hr}$. In studies of effects on preformed biofilms, LB was introduced over the cells at 10 $\mu\text{L/hr}$ for a period of 36 to 48 hours to yield stable biofilms. Then, the analog or analog-antibiotic combination was introduced for an additional 36 to 48 hours. In all experiments, growth medium was refreshed every 12 hours for all biofilms by replacing the used reservoir with one containing fresh LB or a freshly prepared solution of LB and

analog or antibiotic. This procedure was implemented to prevent potential QSI degradation and maintain parallelism between concurrent experiments.

3.1.1.3 Biofilm Staining and Confocal Microscopy

Biofilms were stained *in situ* for microscopy. They were first treated with a Live/Dead bacterial labeling kit (Invitrogen #L7012) in which two labeling components were mixed in a 1:1 ratio to a final volume of 10 μ L. The dye was introduced into the channel at 10 μ L/hr, the same flow rate as during biofilm growth. This treatment was then followed by 10 μ L/hr flow of 100 μ g/mL of calcofluor (Fluorescence Brightener 28, Sigma Aldrich #F3543) in deionized (DI) water for labeling polysaccharides contained in the biofilm matrix [134]. The dyes were fixed by flowing in 3% paraformaldehyde at the same flow rate.

Labeled samples were imaged using a confocal microscope (Zeiss LSM710). For unpatterned coverslips, Z-stacks were obtained at 7 points in each microfluidic channel, with each stack containing 150 image slices. For patterned coverslips used while measuring the optical density of the biofilms, two image stacks were obtained in each channel (i.e. one at each observation window). The image stacks were analyzed using COMSTAT [95], which provided morphological characteristics. Biofilm thickness and biomass were averaged over the image stacks obtained at each point in the microfluidic channel. While other parameters may be investigated via COMSTAT, these two features were deemed most representative of the changes observed in these studies. Additionally, surface reconstructions of the biofilms were created using Imaris (Bitplane, Inc.) to aid in visualization of the resulting structures.

3.1.1.4 Optical Density Measurement and Analysis

While confocal microscopy is extremely effective for characterizing bacterial biofilms, especially in conjunction with analysis software such as COMSTAT [95] and Imaris, implementing this method requires extensive sample preparation and imaging time; the staining and imaging performed in this study required up to 12 hours of time added to the experiment itself. In addition to the benefits provided by the microliter-size channel volume, microfluidic biofilm reactors also possess the ability to integrate precise biofilm measurements with the fluidic operation of the device. In this work, the microfluidic reactor was integrated with continuous optical density measurement [118] to dynamically evaluate the synergistic influence of AI-2 analog and antibiotic on preformed biofilms.

The data corresponding to the change in optical density of the biofilms were obtained from the photodiodes using the methodologies described in Chapter 2. However, the methodology for analyzing the raw optical density data was updated to aid in understanding the trends and to account for device-to-device variations. As optical density measurement was used only to evaluate QSI effects on preformed biofilms, data for each channel (the average of the response of the two photodiodes) was normalized with respect to the optical density at the time treatment was introduced (48 hours). This method reflects that as of the time of introduction, the biofilms were grown under identical conditions although their optical density values may not be identical due to device-to-device variations in biofilms. In a system such as a spectrophotometer, a high optical density such as that of a mature, 48 hour biofilm, is expected to yield a non-linear response. However, normalization to the biofilm state at 48 hours was considered to be

appropriate for this particular microfluidic platform due to the linearity seen at high OD_{600} values in the photodiode output, as discussed in Section 2.1.3.1.

Since the optical density data itself fluctuates as the biofilm grows, as discussed in Section 2.1.4.1, the data for each curve was fitted in Origin (Origin Lab Corporation) using a Churchill model [135]. The Churchill model, while intended for application toward batch cultures, was used here to approximate the similar growth and death phases of a biofilm. The model is represented by

$$\log N = [f_1^{-1} + f_2^{-1}]^{-1} . \quad (3.1)$$

Here, N represents the biomass; in this case, it was assumed to be directly correlated to the optical density. f_1 and f_2 represent the growth and death of the culture, respectively, and can be expressed in a generalized form as

$$f_1 = K_1 \exp(\lambda_1 t) \quad (3.2)$$

$$f_2 = K_2 \exp(-\lambda_2 t) . \quad (3.3)$$

When the model was fitted to the raw data, overall trends were represented, as shown in the sample data from Figure 3.1a. However, the occasional sharp fluctuations in optical density heavily influenced the fitted curve – while the biofilm at one observation window may become suddenly much more optically dense than the other due to natural fluctuations, the average of the two windows also changes sharply, but is not indicative of the overall behavior of the biofilm. To minimize the effects of sharp fluctuations, the Churchill model was also fitted to data points representing 6 hour optical density averages, producing the plot shown in Figure 3.1b.

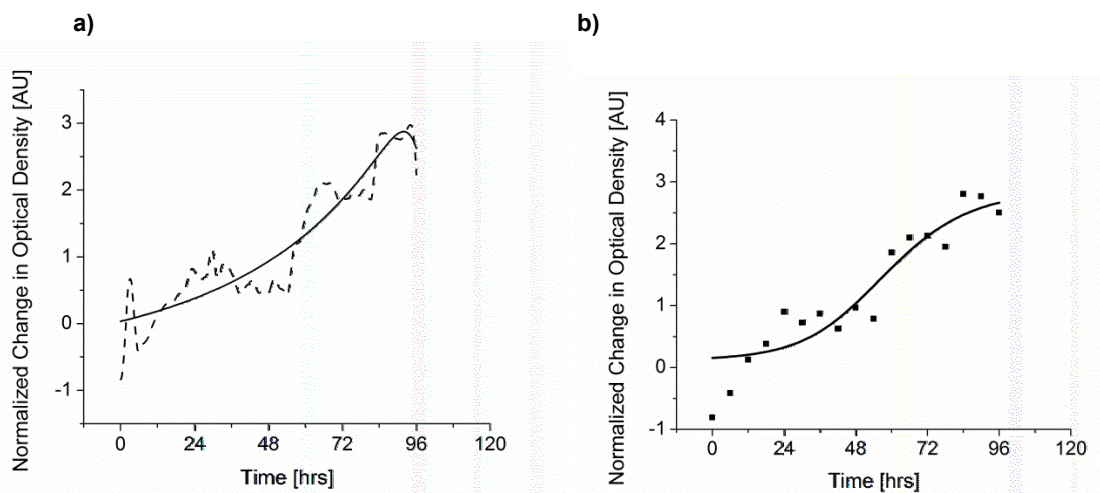


Figure 3.1. Analysis of optical density curves and fits using *E. coli* biofilm growth data (a) Normalized change in optical density; raw data (dotted line) was normalized with the change in optical density at 48 hours set to be 1. The curve was fit (solid line) using a Churchill model. (b) Adjusted curve fit, using a fit to data averaged every 6 hours (squares). The curves have also been adjusted to reflect a zero change in optical density at the beginning of growth.

3.1.2 Results and Discussion

3.1.2.1 Biofilm Maturation in the Presence of AI-2 Analog

The effect of the analog on biofilm growth was tested by continuously exposing the cells to analog diluted in LB. As summarized in Figure 3.2a, perfusion of LB media enabled biofilm growth to an average thickness of 22 μm and an average biomass of 14 $\mu\text{m}^3/\mu\text{m}^2$ by the end of the incubation period (48 hours). The presence of 40 μM isobutyl-DPD inhibited the biofilm growth by approximately 70%, yielding films 7 μm thick with a biomass of 3.5 $\mu\text{m}^3/\mu\text{m}^2$. Increasing the analog concentration to 100 μM had no further inhibitory effect on biofilm thickness. Surface rendering images of the biofilms confirmed that without isobutyl-DPD exposure, the biofilm was much thicker and more structured (e.g. more void space, microchanneling, larger groupings of live and dead cells, Figure 3.2b). The presence of analog in both 40 and 100 μM concentrations yielded biofilms more like thin bacterial carpets (Figure 3.2c, d). A striking difference however, was found between the isobutyl-DPD treated cultures. The biofilm

with 100 μM isobutyl-DPD appeared sparser and had less surface coverage than the biofilm exposed to 40 μM isobutyl-DPD. Moreover, nonviable cells were virtually absent and a preponderance of polysaccharide was found. These morphological differences are evident in the surface reconstructions presented in Figure 3.2b-d.

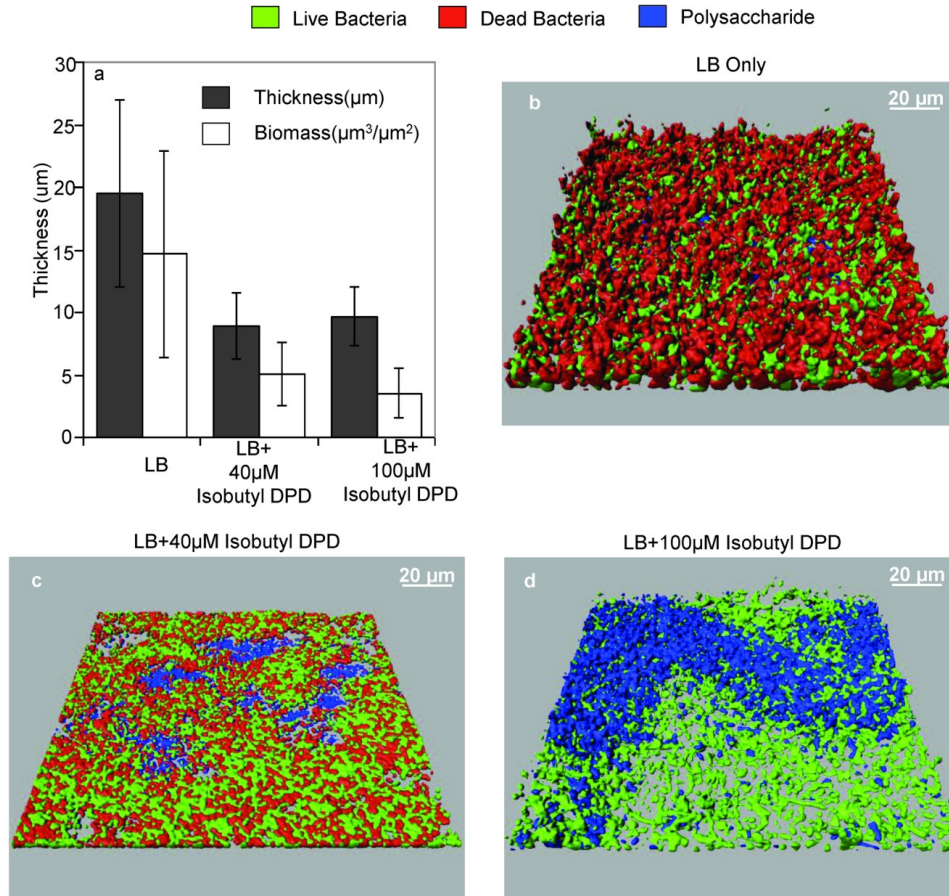


Figure 3.2. Analysis of 48 hour *E. coli* biofilm thickness and architecture in response to isobutyl-DPD. a) Thickness and biomass of biofilm analyzed by COMSTAT (average of four different points). **b–d)** Representative Imaris 3D surface reconstructions of the biofilm with **b)** LB only, **c)** LB+40 μM isobutyl-DPD, **d)** LB+100 μM isobutyl-DPD. Images were selected from locations with average thicknesses and biomasses closest to the average of all points analyzed.

While the AI-2 analogs did not directly kill the bacteria, the interference in the mechanisms involved in forming a biofilm (e.g. motility [15] and extracellular matrix secretion [56, 129]) appeared sufficient for inhibition of a stable, three-dimensional biofilm architecture. Lacking the structural cohesiveness of an extracellular matrix

produced with the aid of native quorum sensing [56], biofilms treated with large analog concentrations were potentially more susceptible to delamination. As non-viable cells have weaker substrate adhesion than viable cells, they are more likely to delaminate in the absence of a cohesive polysaccharide matrix. This hypothesis was supported particularly by the results in Figure 3.2d; after growth with 100 μ M isobutyl-DPD, nonviable cells were removed from the biofilm polysaccharide matrix. Conversely, the remaining polysaccharide matrix that was not able to retain these cells maintained adhesion to the substrate. Irrespective of these polysaccharide and Live/Dead assays, results clearly demonstrated that isobutyl-DPD, a known inhibitor of QS responses in *E. coli* [84], can also decrease biofilm formation by *E. coli*.

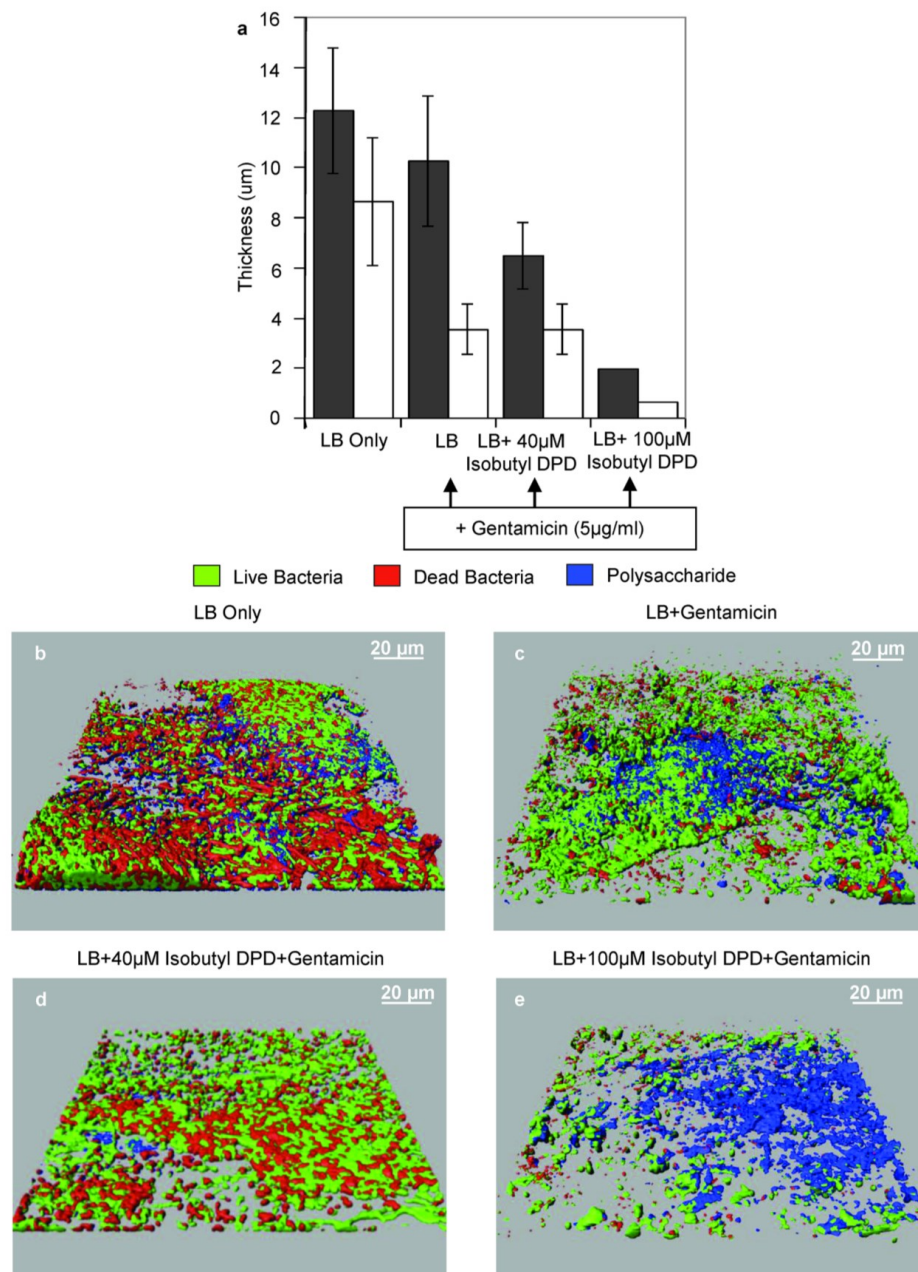
Compared to untreated biofilms, biofilms treated with AI-2 analogs throughout growth were thinner and less ordered as noted by an apparent lack of cohesive 3D structure, such as mounds. QS inhibitors, while not bactericidal, can mitigate biofilm formation by inhibiting bacterial communication, thereby restricting expression of genes related to biofilm formation [56, 136]. This suggests that the bacteria within a nascent biofilm might phenotypically be more similar to bacteria in suspension. Biofilms grown here, while continuously supplemented with AI-2 analogs, showed decreased formation even without additional antibiotic.

3.1.2.2 Effects of Analog on Preformed E. coli and P. aeruginosa Biofilms

The phenotypic changes in biofilms continuously exposed to a QSI spurred interest in whether the analog could alter existing biofilms. As isobutyl-DPD is an established QS quencher, it is neither bacteriostatic nor bacteriocidal among planktonic cells [84]. Thus, if isobutyl-DPD were used to treat the bacteria and the pathogenic

bacterial populations were not removed from the host, an infection would persist. As the biofilms described in Section 3.1.2.1 appeared to persist after continuous exposure to isobutyl-DPD, seen in their thinner and more porous structures, it was hypothesized that antibiotic co-administration could be more effective in eventual eradication of biofilm.

In order to test this approach, combinations of gentamicin (5 µg/ml) with increasing concentrations of isobutyl-DPD (40 µM and 100 µM) were used to treat pre-established *E. coli* biofilms. The control biofilm, exposed to LB medium only, exhibited an average thickness of 12 µm and an average biomass of 8.5 µm³/µm² (Figure 3.3a). Addition of gentamicin without AI-2 analog decreased the thickness slightly to 10 µm, yet the biomass dropped by 50% (3.5 µm³/µm²). However, addition of antibiotic and analog (40 µM isobutyl-DPD) decreased the average biofilm thickness to 6 µm (Figure 3.3a). Most importantly, this study showed that 100 µM isobutyl-DPD used with gentamicin was the most effective in clearing the preformed biofilm, shown by the reduction in thickness by more than 80% to an average of 2 µm and by the nearly complete removal of biomass. The 3-D surface rendering images confirmed morphological data (Figure 3.3b-e), as the biofilm surface thickness decreased significantly in the presence of both isobutyl-DPD and gentamicin. With 100 µM of analog and 5 µg/ml gentamicin, the biofilm was extremely sparse.

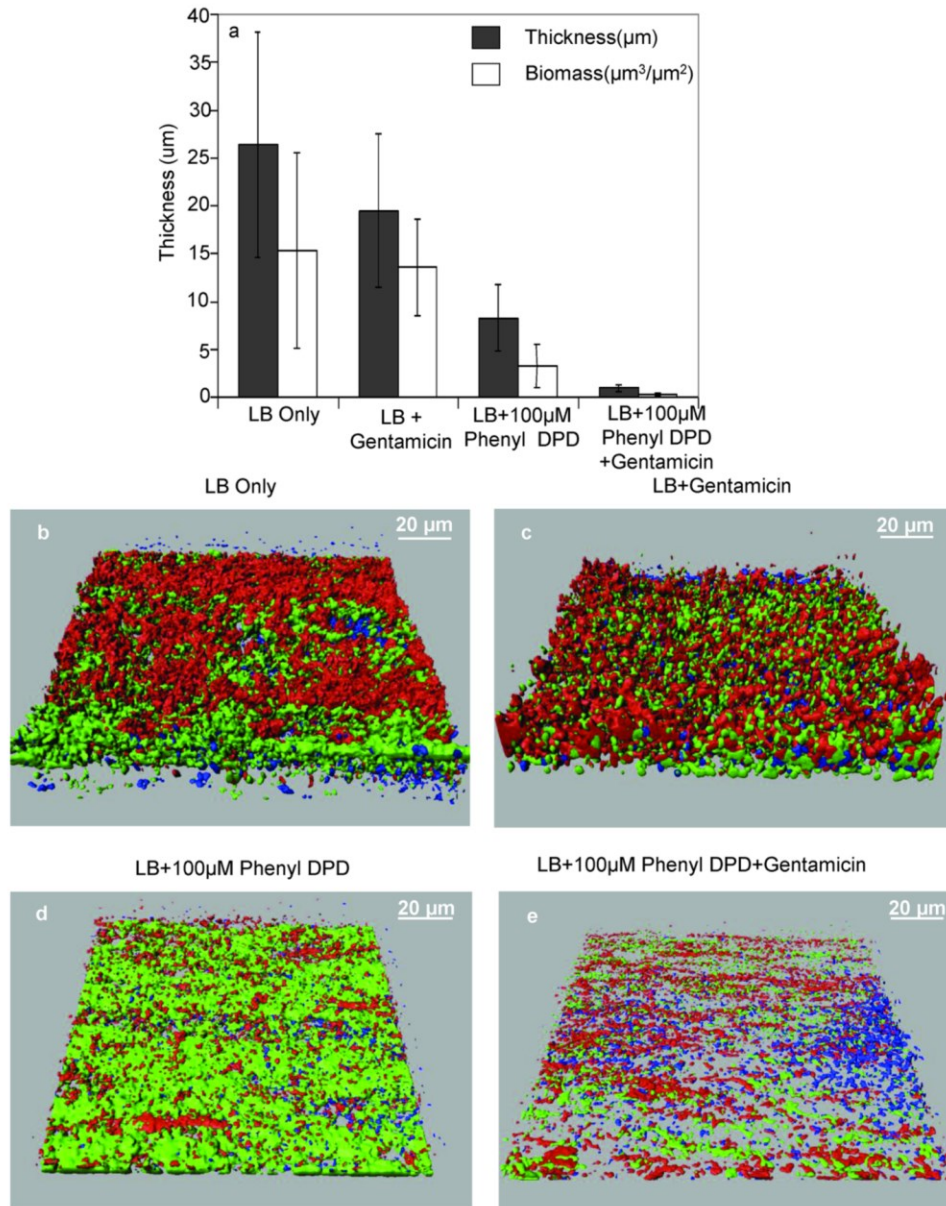


Note: Biofilms were formed for 36 hours, then analog and antibiotic were flown over the preformed biofilm for another 36 hours.

Figure 3.3. Analysis of effect of combinatorial approach analog and gentamicin on preformed *E. coli* biofilm thickness and architecture. a) Thickness and biomass of biofilm analyzed by COMSTAT (average of five different points in the channel). b–e) Representative Imaris 3D surface reconstructions of the biofilm with b) LB only, c) LB+5 µg/mL gentamicin, d) LB+40 µM isobutyl-DPD+5 µg/mL gentamicin, e) LB+100 µM isobutyl-DPD+5 µg/mL gentamicin. Images were selected from locations with average thicknesses and biomasses closest to the average of all points analyzed.

QS quenching activity of *P. aeruginosa* by some C1-alkyl analogs, phenyl-DPD in particular, has been observed [85]. Considering the reduction of preformed *E. coli*

biofilms upon application of isobutyl-DPD with gentamicin, a combination of phenyl-DPD (100 μM) and gentamicin (5 $\mu\text{g/ml}$) was applied to pre-existing *P. aeruginosa* biofilms, analogously to the *E. coli* experiments. When treated with a combination of phenyl-DPD and gentamicin, *P. aeruginosa* biofilms became far more thin and more sparse than untreated controls (thickness, 2 μm vs. 26 μm ; biomass, < 2 $\mu\text{m}^3/\mu\text{m}^2$ vs. 15 $\mu\text{m}^3/\mu\text{m}^2$, Figure 3.4a). These results were corroborated by qualitative evaluation of the images obtained through surface rendering of confocal microscopy results (Figure 3.4b-e). Biofilms grown without the addition of phenyl-DPD showed denser surface coverage and appeared more structured than biofilms grown with phenyl-DPD. The *P. aeruginosa* biofilms treated with both phenyl-DPD and gentamicin, similar to *E. coli* results, were much sparser than controls with LB.



Note: Biofilms were formed for 36 hours, then analog and antibiotic were flown over the preformed biofilm for another 36 hours.

Figure 3.4. Analysis of effect of combinatorial approach analog and gentamicin on preformed *P. aeruginosa* biofilm thickness and architecture. **a)** Thickness and biomass of biofilm analyzed by COMSTAT (average of five different points in the channel). **b–e)** Representative Imaris 3D surface reconstructions of the biofilm with **b)** LB only, **c)** LB+5 $\mu\text{g}/\text{mL}$ gentamicin, **d)** LB+100 μM phenyl-DPD, **e)** LB+100 μM phenyl-DPD +5 $\mu\text{g}/\text{mL}$ gentamicin. Images were selected from locations with average thicknesses and biomasses closest to the average of all points analyzed.

In the experiments performed on biofilms continuously exposed to a QSI from the beginning of growth, it was demonstrated that a QSI could inhibit biofilm formation. Here, it was also observed that application of QSIs to a mature biofilm also decreased its

thickness and biomass compared to untreated biofilms. When AI-2 analog was supplemented with gentamicin, the biofilms were almost completely removed, presumably because they were more susceptible to antibiotic exposure. The above experiments, for the first time, demonstrated the effectiveness of AI-2 analogs in decreasing the growth of *E. coli* and *P. aeruginosa* biofilms.

This study highlighted the importance of a QSI and antibiotic combinatorial therapy as being more effective than antibiotics alone in significantly clearing both *E. coli* and *P. aeruginosa* preformed biofilms. Of note is the concentration of gentamicin used in this work, 5 µg/mL, specifically selected to be on the same order of the 4 µg/mL MIC for *E. coli* K-12 [137]. Gentamicin MIC values for *P. aeruginosa* PAO1 have been reported from 2 to 6.25 µg/mL [138]. The effects on biofilms seen here are created by antibiotic concentrations within the normal planktonic culture-derived MIC values, which in turn, are expected to be much lower than needed for biofilms [121, 139]. That is, standard inhibitory antibiotic doses for planktonic cultures were applied combinatorially with AI-2 analogs and were able to clear preformed biofilms in the microfluidic channels. The augmentation of the antibiotic or anti-biofilm effects of gentamicin by co-administration with AI-2 analogs is significant because it could lead to dispersal of biofilm infections with sub-MIC levels of antibiotics, thereby preventing destruction of the native microflora. Second, the use of lower concentrations of antibiotics can potentially delay the emergence of resistant strains. Also, for existing antibiotics with a narrow therapeutic window due to toxicity to the host, a strategy to lower the MIC or synergistically aid the antibiotic to clear biofilms at lower concentrations would expand the applicability of these antibiotics.

3.1.2.3 Investigation of Live/Dead Proportions

The Live/Dead staining kit used is designed so that SYTO9, which fluoresces green, stains the DNA of both viable and unviable bacteria. Propidium iodide (PI) stains the DNA of only unviable bacterial cells with damaged cell membranes; as PI has a higher degree of fluorescence intensity than SYTO9, its signal dominates over the SYTO9 signal generated by stained unviable cells. In theory, exposure to antibiotic kills more bacteria and produces more PI-stained cells. As posited previously, exposure to an AI-2 analog inhibits EPS production, possibly allowing for the release of nonviable cells from the biofilm since they have a weaker degree of adhesion than healthy bacterial cells. Therefore, it is conceivable that a biofilm may be characterized by the ratio of red to green fluorescent cells, indicative of the health of the biofilm when taken into consideration with the biofilm's average thickness.

In order to investigate the potential for biofilm characterization via live : dead ratio, the confocal images obtained for the above studies were analyzed for viable cell content, using the volumetric ratio of red fluorescent to green fluorescent cells obtained using Imaris. Data are summarized below in Figure 3.5.

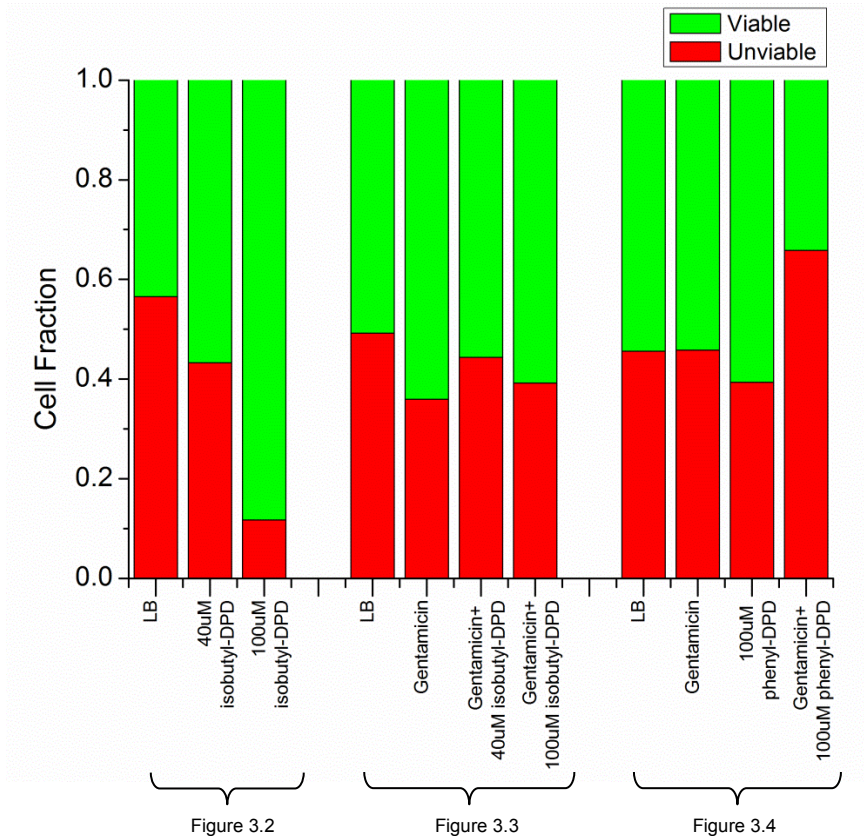


Figure 3.5. Comparison of Live/Dead percentages in confocal images presented in Figures 3.2-3.4, reflecting the effect of continuous *E. coli* biofilm exposure to isobutyl-DPD (Figure 3.2), and exposure of preformed *E. coli* (Figure 3.3) and *P. aeruginosa* (Figure 3.4) biofilms to gentamicin and isobutyl-DPD. Each bar represents one imaged location within the channel. Results were expected to show a decrease in unviable cells with addition of DPD analogs, indicative of a weaker extracellular matrix; as shown, actual results obtained were inconclusive.

No clear deductions can be made from Figure 3.5. In the case of the data obtained from image stacks presented in Figure 3.2 (the first 3 bars), addition of analog decreased the unviable cell composition as expected. However, in the data from Figure 3.4 (the last 4 bars), addition of analog or of antibiotic had little effect on the unviable cell composition, and combinatorial addition of both increases the unviable cell composition.

Although the concentrations of stains are developed by the manufacturer to be applicable to the majority of strains of bacteria, irregular staining or false signals are still possible depending on a number of factors, including the metabolism of the bacterial culture and thoroughness of rinsing after stain application [140, 141]. If the

viable : unviable cell ratio is to be used as a metric for biofilm health, extensive characterization of the stains and staining protocol for the strains and conditions used must be performed. For the purposes of these studies, no quantitative conclusions were drawn from the amount of viable and unviable cells within a biofilm, and both types of stained cells were considered as a lumped element of biomass.

3.1.2.4 Leveraging Microscale Reactor for Streamlined Measurement

Optical density measurement using the device with the patterned base, as in Chapter 2, was used to gather data from both *E. coli* and *P. aeruginosa* biofilms treated with the analog-antibiotic combinatorial approach. Dynamic analysis of replicate windows revealed a complex non-uniform process that when fitted to a mathematical model suggested relatively uniform biofilm growth overall for the first 48 hours, at which time, divergent behaviors were observed based on small molecule addition (Figure 3.6a, c). For *E. coli* (Figure 3.6a, b), biofilm growth was similar over the first 48 hours between the three experimental groups grown under identical conditions over that period. After 48 hours and initiation of treatment to two of the channels, the biofilm progression deviated with the most dramatic departure being the combination of isobutyl-DPD and gentamicin. For *P. aeruginosa*, effects were roughly similar, although gentamicin alone was less effective when comparing optical density and thickness (Figure 3.6c, d). In all cases, however, the addition of gentamicin with a QSI after 48 hours slowed the progress of biofilm maturation relative to the controls, resulting in diminished films by the end of the experiments.

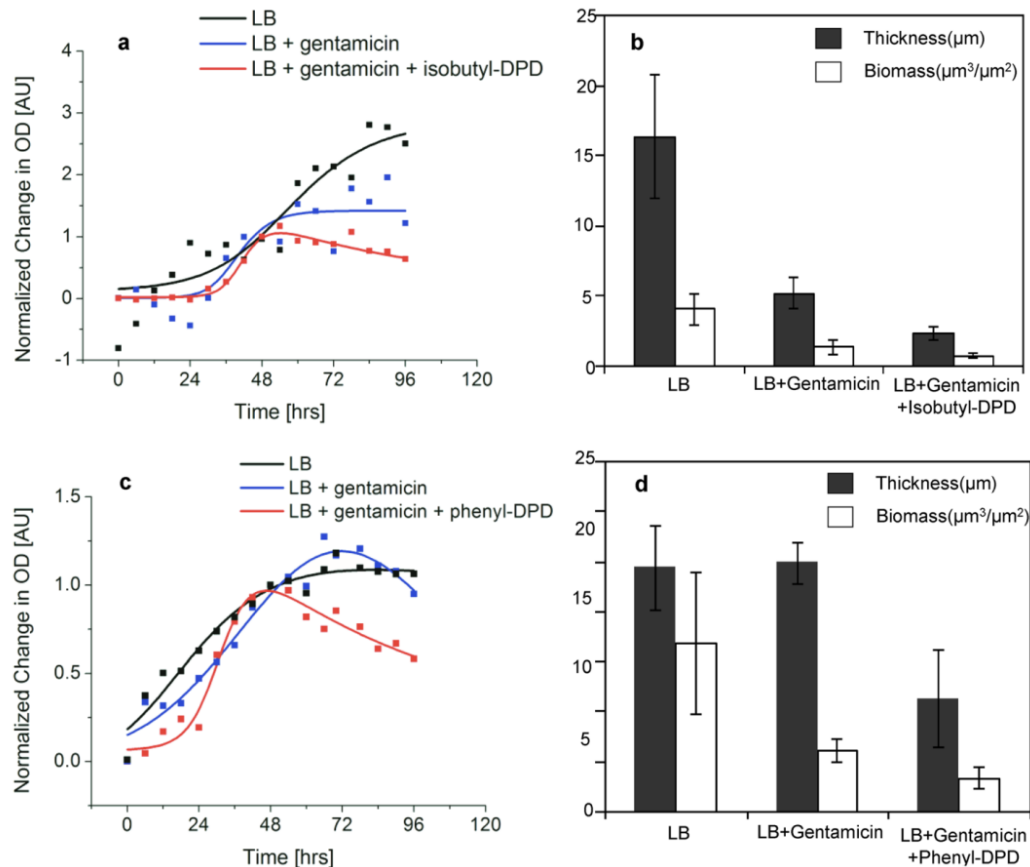


Figure 3.6. Analysis of effect of combinatorial approach on optical density and thickness using analog and gentamicin on *E. coli* (a, b) and *P. aeruginosa* (c, d) biofilms preformed for 48 hours. a) Normalized change in optical density of *E. coli* biofilms; raw data (dotted lines) were normalized with the change in optical density at 48 hours set to unity. Curves were fitted (solid lines) using a Churchill model [135]. b) Thickness and biomass of *E. coli* biofilm analyzed by COMSTAT (average of two points in the channel). c) Normalized change in optical density of *P. aeruginosa* biofilms; raw data (dotted lines) were normalized and fitted (solid lines) using a Churchill model. d) Thickness and biomass of *P. aeruginosa* biofilm analyzed by COMSTAT (average of two points in the channel).

While the optical data in Figure 3.6a, c are presented as discrete and averaged values, in actuality, a large amount of information was gathered from the two photodiodes. By observing the temporal variance in the response (Figure 3.7), the state of the biofilm and temporal disturbances were evaluated. It was noted that for continuous optical measurements over the two observation windows, the standard deviation in the optical density values was typically less than 10% of the average after initial biofilm growth, as seen after the first 24 hours of *P. aeruginosa* biofilm growth in the sample data in Figure 3.7. The internal consistency of the spatial and temporal variation in

biofilm optical density added to the reliability of the trends in optical data observed for such a small sample volume. It was noted, however, that increasing the number of observation windows as in the second generation device in Section 2.2 would enable greater resolution of the area-based heterogeneity of the film.

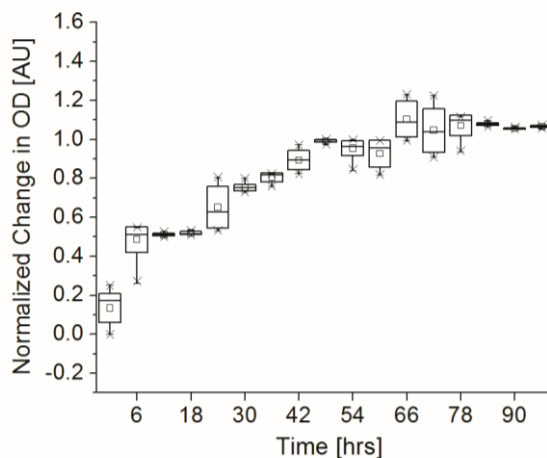


Figure 3.7. Box-and-whiskers plot of the control group (LB) in Figure 3.6c, demonstrating the temporal variability observed through optical density monitoring. Each square represents the optical data averaged between two windows and averaged over 6 hour time windows centered at each point (endpoints are averaged over 3 hours). Middle horizontal lines represent the median, and top and bottom horizontal lines represent ± 1 standard deviation of the data. Minimum and maximum points within the data sets are denoted by an “x”.

3.1.3 Conclusion

The use of a microfluidic testing environment with small sample volumes made this investigation of QSI impact on biofilm formation possible. The integration of optical measurements in a dynamic and controllable environmental setting allowed for evaluating the “instantaneous” state of the biofilm. This contrasts with the sole use of microscopy, which only permits an endpoint measurement. Therefore, the use of this microfluidic setup revealed phenotypic data which normally would have been lost had only endpoint measurements been used. Obtaining as much information as possible is especially important considering that the formation of a biofilm itself is highly variable. This is evidenced by the degree of variance in optical density observed over time. By

tracking discrete points throughout biofilm growth and treatment, not only is the timescale of the contribution of the analog and antibiotic synergism toward biofilm reduction clarified, but additional information as to the instantaneous biofilm state and stability is gained. The methodology implemented here thereby promotes a more complete understanding of the temporal and spatial variance in biofilm growth.

In the translation of this work to clinical application, parameters obtained from the *in vitro* device that enable prediction *in vivo* or in other clinical situations would be valuable. The flow conditions, for example, that are imposed on biofilms within our device create shear stress levels similar to those found in interstitial fluid [142]. Shear stress, along with the bacterial strain, growth media, and materials used to construct the microfluidic channel, may all be adjusted to more closely mimic the environments in which biofilms typically form infections [143]. Also, owing to the microscale confinement imposed by this system, another physical parameter, biofilm thickness, might be a good predictor of *in vivo* behavior. Dental biofilm thicknesses have been shown to grow to approximately 50 μm after 1 week [144], while mature biofilms recovered from urinary catheters can range between 3 and 490 μm , depending on the formative species [145]. A mouse model of thermal injury showed mature, 11 μm -thick *P. aeruginosa* biofilms at 46 hours [146]. While the biofilms formed may be thin, the infections formed in this type of model are typically fatal within 48 hours [147]. Combining these models with the fact that biofilms produced in this work range from 25 to 40 μm within 48 hours, this microfluidic platform is capable of producing biofilms within the appropriate ranges for extension to clinical environments. Also, the novel combinatorial treatment, as presented in this work, is ideally suited toward expanding the

range of physiological, chemical, and physical parameters needed to most accurately mimic *in vivo* systems.

3.2 Effect of Quorum Sensing Inhibitors on Persister Cells

The major knockdown of biofilm formation produced by QSIs applied in conjunction with antibiotics raised a number of questions as to the mechanisms by which the biofilm was reduced. As discussed in Chapter 1, antibiotic-tolerant bacterial persister cells are a major contributor to the formation of chronic biofilm infections; one hypothesis for the effectiveness of the synergistic treatment was that the mechanism of biofilm inhibition was related to a possible knockdown in the number of persister cells. While unpublished studies mentioned in a review by Lewis indicate quorum sensing most likely has no effect on persister cell formation [54], two different persister assays were performed on cells exposed to a QSI in order to evaluate potential effects of QSIs on persister cells.

3.2.1 Methods

3.2.1.1 Culture Conditions and Persister Isolation

Persister assays were performed on *E. coli* K-12 MG1655 ATCC #47076 using a colony forming unit (CFU) assay adapted from [148]. Normally, persister cells are formed in suspension cultures of bacteria by treating the culture with a high dose of antibiotic. All the cells are killed except for the persisters, which are genetically identical to the cells that were killed, but are simply dormant. To perform the assay, an overnight culture of *E. coli* was grown in LB media at 37 °C and 200 rpm. 1 mL of the overnight culture was re-inoculated in 50 mL of LB media, and the suspension was allowed to grow

to an OD₆₀₀ of approximately 0.5. The suspension was centrifuged at 750 rpm for 15 minutes, then resuspended in LB media to yield a suspension of OD₆₀₀ 1.0. The resulting suspension contains cells in exponential phase, but at an artificially high concentration.

Samples of these cells were treated for 24 hours under four conditions: control (no treatment), 100 µg/mL gentamicin, 100 µM isobutyl-DPD, and 100 µg/mL gentamicin with 100 µM isobutyl-DPD. Within an experiment, replicates were performed for each of these four groups.

3.2.1.2 Assessment of Persister Cell Populations

After 24 hours of exposure to treatment, serial dilutions from 10⁻² to 10⁻⁸ were prepared from all groups and plated on LB agar plates containing 50 µg/mL gentamicin. After 24 hours, colonies on the plates were counted; the number of colonies is indicative of the number of CFU remaining after the four treatments were administered. After exposure to high doses of antibiotic, colonies are only formed by persister cells able to withstand such treatment.

In addition to the CFU assay, samples of cells were treated with a Live/Dead bacterial labeling kit (Invitrogen #L7012) for examination with fluorescence automated cell sorting (FACS) to determine the percentage of live cells in treated cultures. While FACS is not a traditional method for evaluating persister cell populations, after treatment with a high dose of antibiotic, most cells should be dead except for a small number of persisters, whose intact cell membranes will allow for fluorescent staining as “live” cells. FACS samples were prepared by centrifuging 250 µL samples from each culture at 750 rpm for 15 minutes. The supernatant, presumably consisting of spent LB growth

media, was pipetted out and replaced with the same volume of phosphate buffered saline (PBS). Cells were resuspended in the solution, and treated with the Live/Dead staining kit according to the datasheet, which specifies 3 μL of total dye solution (consisting of a 1:1 ratio of SYTO9 to propidium iodide) for a 1 mL bacterial suspension. Dye was mixed thoroughly with the suspension, and incubated in the dark for 15 minutes. Stained samples were fixed with 3% paraformaldehyde in a 1:1 ratio of sample to paraformaldehyde.

3.2.2 Results and Discussion

The results, including details of replicates within the colony forming unit assay and the FACS study, are shown in Figure 3.8. Note that colonies were counted on plates with higher dilutions (denoted below x-axis) for groups with no antibiotic administration, as the high number of CFU plated at high dilutions yielded a number of colonies so large that colonies often merged together.

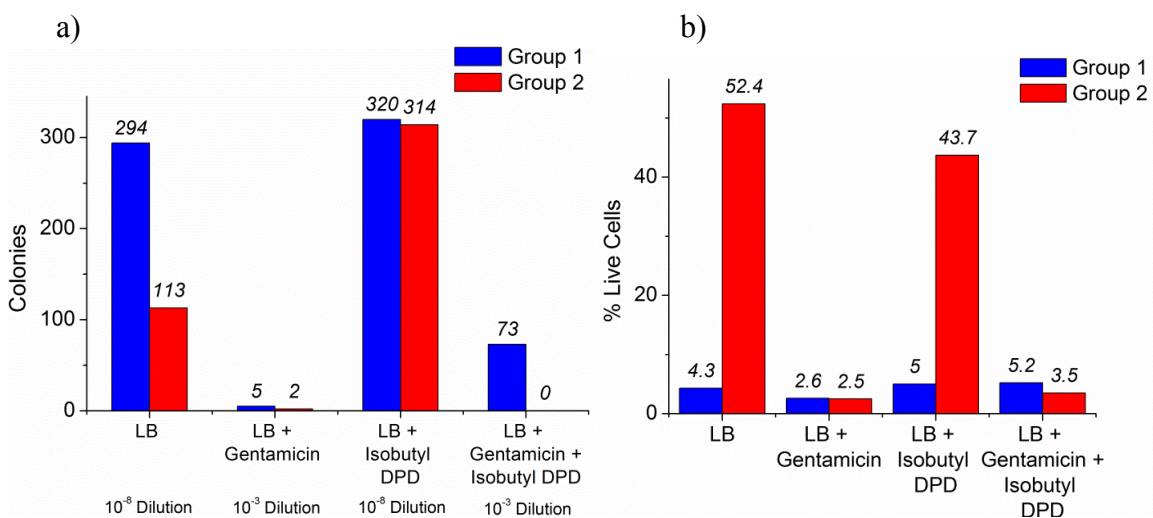


Figure 3.8. Results from persister cell formation experiments. In both (a) and (b), the first column was untreated, representing a control in which many colonies are expected; similarly, the third column was treated only with isobutyl-DPD, which does not cause cell death. The second column and fourth columns respectively represent generation of persister cells via treatment with a high concentration of antibiotic and the addition of analog to this treatment. Groups 1 and 2 are replicates. (a) Data from counting colonies formed after plating treated suspensions. (b) Data obtained via FACS.

There was a large amount of variation between replicates, making it difficult to draw definitive conclusions. While most likely unrepresentative of the true biological results, averages of the two replicates in both assays were taken to aid in data interpretation.

These data are shown in Figure 3.9.

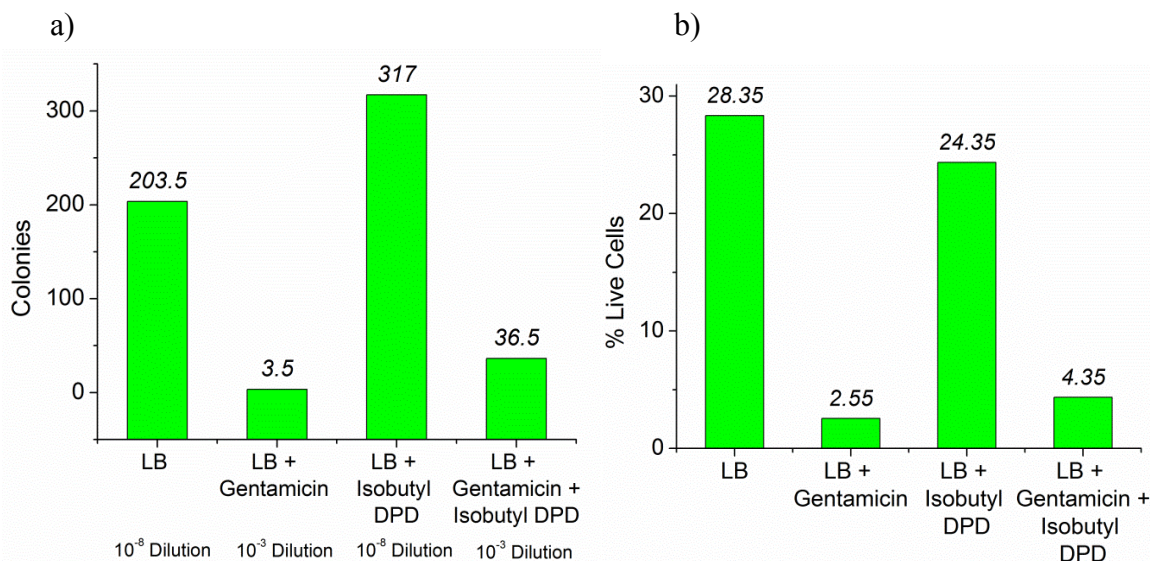


Figure 3.9. Data from Figure 3.8, where each bar is an average of Group 1 and Group 2 as presented in Figure 1. (a) and (b) correspond to the data from Figure 3.8a and 3.8b respectively. As the data are the average of two data points, standard deviations are not presented.

Examining the averages, the results for the control were expected, in that there were many live, intact cells capable of forming colonies. Additionally, the large number of CFU and live cells in the group treated with only isobutyl-DPD were also expected, as isobutyl-DPD does not kill the cells at the concentration used. Note that in these cases, plates with higher dilutions were used, as individual colonies could not be counted on plates inoculated with low dilution cultures. In general, the groups to which gentamicin was added also yielded expected results, since there were fewer live cells. These live cells represent the population of persister cells. However, the addition of analog appeared to have little effect on formation of persister cells.

As discussed in Chapter 1, there are mentions in literature of unpublished studies indicating quorum sensing has no influence on persister cell formation [54]. It is possible that there may be an indirect relationship between quorum sensing and persister cells that the experiments here and in literature cannot elucidate, as AI-2 is linked to intracellular enzymatic pathways through a complex network. Additionally, QSIs may also influence cellular pathways outside of the intended targets. For example, Pan et al. showed that some synthetic brominated furanones, inhibitors of AI-2 based quorum sensing and biofilm formation, reduce the incidence of persister cells of *P. aeruginosa* PAO1 [149]. However, this restoration of antibiotic sensitivity was also independent of the QS inhibition that the brominated furanones are associated with. Considering the complexity of both quorum sensing and biofilm formation, along with the ongoing characterization of the AI-2 analogs used here, extensive studies beyond the preliminary work here must be designed and performed in order to clarify the relationships between these analogs, biofilm formation, quorum sensing, and persister cells.

3.3 Chapter Summary

This work demonstrated several key findings. First, biofilm development was inhibited by continuous application of AI-2 analogs. Second, combination of these analogs with sub-MIC gentamicin concentrations enabled removal of preformed biofilms. While the precise mechanisms of biofilm clearance in the presence of analogs remains unclear, initial experiments indicated a lack of connection between analog exposure and persister cell elimination. In terms of the goals of the dissertation, what was most important was application of the microfluidic observation platform developed in Chapter 2 to provide critical information about short-range biofilm changes in response to

administration of a new antimicrobial under test. As a whole, the work demonstrated both the success of the platform when used as a pharmaceutical testbed, as well as the potential to enable significant advances in bacterial biofilm science.

4 Development of Multi-depth Microfluidics for Controlled Biofilm Studies

This chapter covers the development of a device designed to address the variability in biofilm formation between devices observed in the studies presented in Chapter 2. The new device also streamlined performance of multiple parallel experiments. The platform was designed to segment bacterial biofilms in one microfluidic channel for multiplexed experiments and promotion of experimental control. Sectioning was achieved by integrating hydraulically actuated valves into the polydimethylsiloxane (PDMS) microfluidic device. The differing geometric requirements of hydraulic valving (shallow, rounded) and biofilm growth (deep) were negotiated by creating a mold with two types of photoresist. Fabrication incompatibilities between resist types were circumvented by protecting pre-existing photoresist structures with a solvent barrier layer using atomic layer deposition (ALD). The final device successfully demonstrated the growth and subsequent segmentation of *Escherichia coli* biofilms, and was used to evaluate the effects of different concentrations of the detergent sodium dodecyl sulfate (SDS) on mature biofilms.

4.1 Design

4.1.1 Overview

Macroscale biofilm studies have shown that biofilm formation is sensitive to a variety of growth parameters, and it is likely that no two biofilms can be compared [27, 28]. To address biofilm variability, macroscale reactors such as the Modified Robbins Device or Calgary Biofilm Device often incorporate a method for performing assays on multiple sections of one biofilm [8, 11]. Performing different tests on separate portions

of one biofilm provides a significant advantage over parallel biofilm formation, as the variability between biofilms formed separately under the same conditions can preclude their accurate comparison when used as experimental and control groups in a biofilm assay.

The compiled results of the previous chapters demonstrated that biofilms formed in the custom microfluidic reactor also exhibit variability between separate experiments. This was seen in the spread of optical density data in Chapter 2 – identical experiments performed on different days yielded biofilms with different optical densities, necessitating use of the percent difference between experimental and control groups as a metric. Variability was also evident in comparing the control biofilms between experiments in the QSI studies in Chapter 3. In one study, 96-hour *Pseudomonas aeruginosa* biofilms were $26 \pm 11 \mu\text{m}$ thick, while another identical study yielded $17 \pm 2 \mu\text{m}$ -thick biofilms (Figure 3.4a and Figure 3.6d). Considering the observed experiment-to-experiment variability, the macroscale approach of biofilm segmentation was adapted for integration in a microfluidic biofilm growth platform.

The platform included one set of microfluidic channels where biofilms grew and were sectioned, placed on top of another layer of microfluidic channels that operated valves to manipulate the biofilms. An overview of the device operation is depicted in Figure 4.1a, b. The device was designed to have one central microfluidic channel where biofilms form and mature, with access to side channels blocked by closed valves (Figure 4.1a). After maturation, the central channel was divided into three sections using hydraulically actuated valves integrated in the PDMS structure. Valves that formerly

blocked access to the side channels were opened, as shown in Figure 4.1b, to allow flow over each of the three sections of preformed biofilm.

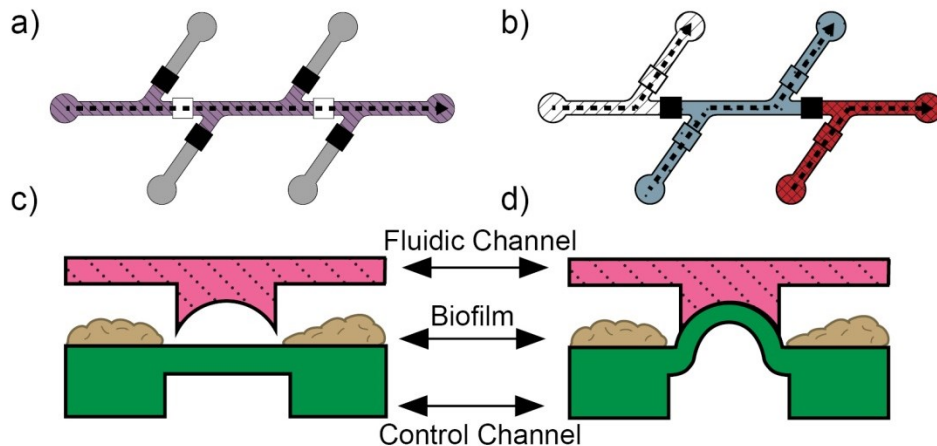


Figure 4.1. a) Schematic of device operation during biofilm growth, with side channels blocked by closed valves (solid black squares) b) Device operation during biofilm sectioning, with side channels open and central channel trisected by two closed valves c) Side-view schematic of open push-up valve integrated with two-depth channel d) Side-view schematic of closed push-up hydraulic valve with pressure applied to the liquid-filled control channel to close the valve.

The valves to control flow and create the device configurations shown in Figure 4.1a, b were integrated in two devices layers of PDMS using a hydraulically actuated “push-up” style valve [110] (Figure 4.1c). Microchannels in the top layer contained biofilms and the surrounding media. The bottom layer contained channels covered by a thin PDMS membrane and filled with liquid, to which pressure was applied for hydraulic actuation. In the valve area, this pressure deformed the membrane and pressed it against the rounded ceiling of the top channel, thereby closing the valve (Figure 4.1d). A three-dimensional representation of this platform is also presented in Figure 4.2.

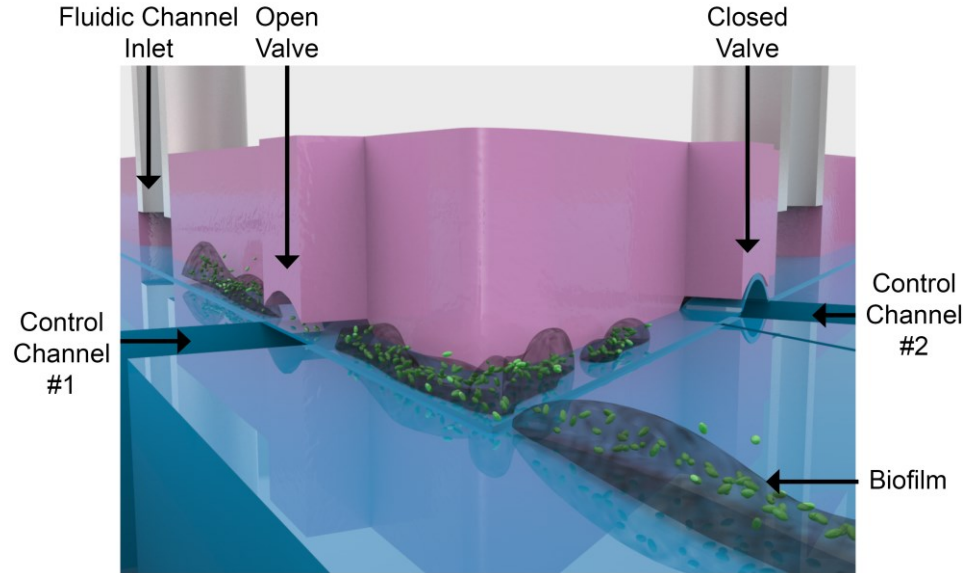


Figure 4.2. Three-dimensional representation of the assembled platform in the biofilm growth configuration (corresponding to Figure 4.1a). Pressure applied to Control Channel #2 closes the corresponding valve and prevents flow into the side channel. The valve regulated by an unpressurized Control Channel #1 remains open, allowing biofilm growth in the central channel where there is flow.

4.1.2 Design Consideration: Channel Depth and Shear Stress on Biofilms

The amount of membrane deflection of a PDMS valve relies on a variety of factors, including the channel dimensions, the PDMS thickness, and the pressure applied [110]. The maximum deflection of a push-up-style valve is typically no more than 60 μm [110]. The channel geometry, including its depth, is directly related to shear stress; the shear stress in turn affects biofilm growth properties, such as thickness and structure [32, 36, 116]. The relationship between channel geometry, flow rate, and shear stress in the microfluidic device can be expressed as

$$\tau = \frac{6Q\mu}{W[\delta - L(t)]^2}, \quad (4.1)$$

where Q is the flow rate, μ is the fluid viscosity, W is the channel width, δ is the channel height, and L is the biofilm thickness at time t . In the extreme case of no biofilm, the shear at the wall would be

$$\tau_w = \frac{6Q\mu}{W\delta^2} . \quad (4.2)$$

In order to more closely follow device parameters shown to create functional push-up valves in literature [110], the final device was designed with channel widths (W) of 350 μm . Aiming to obtain biofilms that could be compared to the biofilms formed in the previous work presented in Chapters 2 and 3, the final device used a 100 μm -deep channel for biofilm growth. Since the channel geometry has a large influence on the shear rate, as shown in Equation 4.2, the volumetric flow rate was adjusted in order to obtain the same shear rate as in the 500 μm -wide, first-generation microfluidic platform. The flow rate that was used, 7.5 $\mu\text{L/hr}$, combined with a 100 μm x 350 μm cross-sectional area created an average flow velocity of 0.06 mm/s and a shear rate only 7% larger than that in the previous work.

While a 100 μm channel depth was desired for biofilm growth, the integrated valves still required a channel less than 60 μm in depth. Consequently, it was necessary to design a compromise between the valve and biofilm growth depth requirements. The incorporation of these design constraints into the microfluidic platform is shown in Figure 4.1c, d. In literature, the control channel is typically the top layer in the PDMS stack, and a PDMS membrane is spun on-top of the fluidic channel [108-110]. However, it is difficult to spin a uniform PDMS membrane on-top of a structure with large variations in topography, such as the multi-depth microfluidic mold required for the valved biofilm growth channel. Since a uniform membrane can be obtained by spinning PDMS on top of a shallow, single-depth mold such as that for the control channel, the final device featured the control channel as the bottom-most layer. The top layer of PDMS contained channels that were deep except in the locations to be sealed by valves.

In the valving areas, the channel profile was shallow and rounded, allowing for more complete sealing than a square profile.

While literature indicates that a channel as deep as 60 μm can be sealed with a push-up valve, the shallow valving areas of the top layer of PDMS were designed to have a maximum depth (at the apex of the arc-shaped cross section) of approximately 35 μm . Designing a shallower channel than the hypothetical maximum provided a safety factor to ensure full sealing, with the additional possibility of lowering the required actuation pressure. Minimizing the pressure required to deflect the membrane and seal the fluidic channel can also minimize the risk of rupturing the membrane and disabling the device.

4.1.3 Design Considerations: Depletion of Oxygen and Nutrients Along Channel

An important consideration for this device was maintaining biofilm uniformity along the channel. While no clear dependence of biofilm growth on location within the channel was observed in previous work, it was considered possible that molecules essential for efficient biofilm growth may be depleted by the time fluid reached the biofilm closest to the channel outlet. An assessment of the likelihood of depletion was performed considering both oxygen and available carbon sources for bacterial metabolism.

Bacterial growth is highly dependent on the available carbon sources. As Luria Bertani (LB) growth medium does not contain glucose, cultures grown in LB utilize amino acids as carbon sources [150]. In this work, growth media was introduced at a volumetric flow rate of 7.5 $\mu\text{L/hr}$, effectively refilling the channel with fresh growth media every 6 minutes. As growth media was introduced faster than the ~ 20 minute doubling time of *E. coli* in LB, it was also assumed that the biofilm culture as a whole

was not restricted by carbon source availability. While nutrient starvation was expected to exist within the biofilm structure, this may be attributed to diffusion, consumption, and degradation as a function of the biofilm itself and not of the reactor.

In order to evaluate the potential for oxygen depletion within the microfluidic channel, a basic analysis of oxygen consumption and transport via convection and diffusion was performed. The elements contributing to changes in oxygen concentration in the microfluidic biofilm growth reactor, as considered in this analysis, are outlined in Figure 4.3.

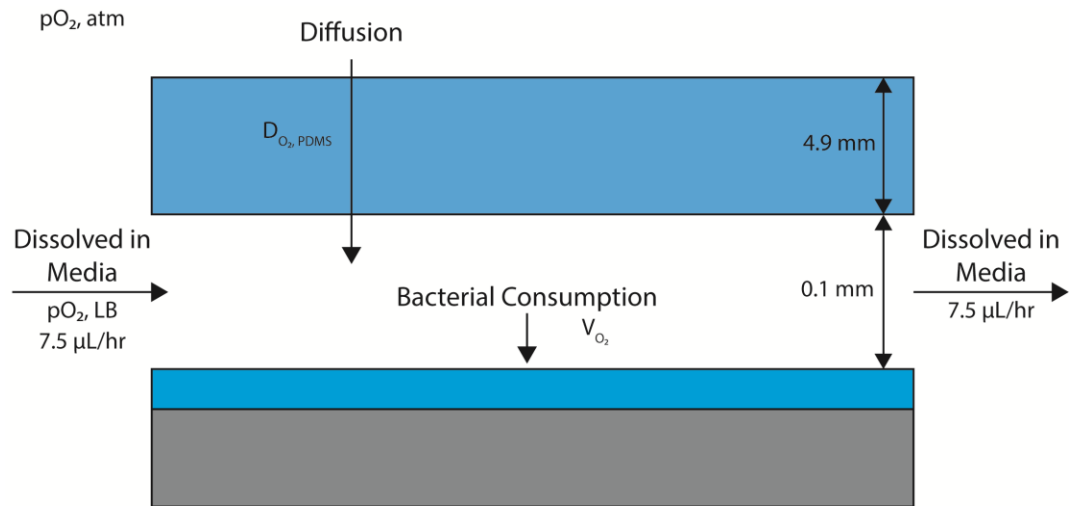


Figure 4.3. Conceptual model of oxygen transport in microfluidic biofilm reactor. This simplified model includes valve-less geometry and does not account for effects on changes in oxygen transport and reaction rates due to biofilm growth.

Oxygen sources include dissolved gas in the growth media and environmental oxygen that diffuses through the PDMS and into the microfluidic channel. Oxygen is consumed by the bacteria, dependent on their metabolic state; unconsumed oxygen exits the channel with waste.

In the microfluidic biofilm growth reactor, oxygen is dissolved in the LB injected into the system. A 1 L solution of LB typically contains 10 g tryptone, 5 g yeast extract,

and 10 g NaCl. The salts and organic compounds in LB alter the solubility of oxygen in the water-based solution. The change in the Bunsen coefficient can be derived from a modification of the Sechenov equation [151]:

$$\log \frac{\alpha_0}{\alpha} = \sum_{i=1}^n H_i \cdot \frac{1}{2} c_i z_i^2 + \sum_{i=1}^n K_i c_{org,i} . \quad (4.3)$$

Here, α is the Bunsen coefficient for the solute (oxygen) in LB and α_0 is the Bunsen coefficient for oxygen in water at 35 °C. H_i is a temperature-dependent parameter specific to the gas and the type of the i -th ionic species dissolved; z_i and c_i represent the charge and molar concentration of the i -th ionic species, respectively. Similarly, K_i is a constant specific to the gas and the i -th organic compound dissolved in the solution, and $c_{org,i}$ is the molar concentration of the i -th organic compound. Using the modified Sechenov equation, the oxygen concentration in LB at 35 °C was estimated to be 6.6 mg/L or 0.206 mol/m³, based on $\frac{\alpha_0}{\alpha} = 1.06$. However, in practice, the composition of LB can vary between batches and experiments dependent on factors such as autoclave time and age of the solution [150].

In addition to oxygen dissolved in the growth media, oxygen also can diffuse into the microfluidic channel through the PDMS, well known for its high gas permeability. The rate of oxygen diffusion into the channel is dependent on the difference in oxygen concentrations between atmospheric air and in the interior of the microfluidic channel. PDMS also has its own oxygen saturation limit, reported as 1.69 mol/m³ [152, 153].

While experiments were not performed to obtain an oxygen consumption value specific to the bacteria and system used here, *E. coli* K-12 consumption of oxygen has been reported as approximately 4.31x10⁻²⁰ mol/cell/s [154]. At the start of an

experiment, with a bacterial inoculum of OD₆₀₀ 0.25 (approximately 1.25x10⁸ cfu/mL), oxygen is consumed at a rate of 4.6x10⁻¹² mmol/s. As the bacteria within the biofilm divide, more oxygen will be consumed throughout the channel.

A basic simulation was performed in COMSOL Multiphysics 4.1 to evaluate possible depletion given higher rates of oxygen consumption. The model included dissolved oxygen in the growth media entering the system, oxygen from ambient air diffusing through the PDMS and into the media, and a flux of oxygen out of the channel floor representing bacterial metabolic activity. The Laminar Flow physics mode was coupled to the Transport of Diluted Species physics mode in the subdomain representing the channel, and a separate Transport of Diluted Species physics mode was applied to the subdomain representing the PDMS.

Diffusion of oxygen into the PDMS from ambient air was modeled using a stiff-spring boundary condition [153], incorporating the partition coefficient into the term for oxygen flux at the air-PDMS boundary. The diffusive flux of oxygen from air into the PDMS can be expressed as

$$N_{O_2} = M(C_{air} - K_{P,air}c_{PDMS}) , \quad (4.4)$$

where M is the stiff spring velocity, $K_{P,air}$ is the partition coefficient, C_{air} is the constant concentration of oxygen in ambient air, and c_{PDMS} is the oxygen concentration on the PDMS side of the interface. Oxygen diffusion from the PDMS into the media was modeled similarly to the PDMS-air boundary, with the diffusive flux of oxygen from the PDMS into the media expressed as

$$N_{O_2} = M(c_{PDMS} - K_{P,PDMS}c_{media}) , \quad (4.5)$$

where M is the stiff spring velocity, $K_{P,PDMS}$ is the partition coefficient, and c_{PDMS} and c_{media} are the oxygen concentrations on the PDMS and media sides of the interface, respectively. Concentrations within the PDMS and the media were modeled using separate Transport of Diluted Species physics modes linked through the flux terms at the boundary between the PDMS and media.

The consumption of oxygen by the biofilm was calculated assuming the bottom of the channel is completely covered with a monolayer of *E. coli* cells, each with an assumed rectangular footprint of $1 \mu\text{m} \times 2 \mu\text{m}$, resulting in a cell density, ρ_{cell} , of 5×10^{11} cells/m². This value corresponds to the same number of cells contained in a suspension of OD₆₀₀ 10 filling the entire $0.84 \mu\text{L}$ channel volume. The boundary flux of oxygen produced by biofilm metabolism can be expressed as

$$N_{O_2} = V_{O_2} \rho_{cell} , \quad (4.6)$$

where V_{O_2} is the bacterial rate of oxygen consumption noted above. While the consumption can be more accurately represented by Monod kinetics, allowing the rate to vary with oxygen concentration, the use of the maximum consumption rate was selected as representative of a condition most likely to induce oxygen depletion. Additionally, while the biofilms formed within microfluidics are typically thicker than a monolayer of *E. coli*, they do not cover the entire channel floor. Biofilms formed experimentally are also expected to have a lower average metabolic rate due to the inclusion of dead cells and extracellular matrix components within the biofilm structure.

Flow within the microfluidic channel was modeled with the Laminar Flow physics mode, using the density and viscosity of water at 35 °C. The boundary condition at the inlet was a normal inflow velocity of 0.06 mm/s, calculated using the channel

dimensions and volumetric flow rate of 7.5 $\mu\text{L/hr}$ used in this work. Within the Transport of Diluted Species physics mode, the boundary at the inlet was set to the calculated saturation concentration of oxygen in growth media, C_{media} .

Relevant parameters for the simulation are summarized in Table 4.1; Figure 4.44.4 shows the simulated media oxygen concentration near the channel inlet.

Table 4.1. Parameters used for COMSOL simulation of oxygen transport.

Parameter	Value	Source	Description
M	1×10^3 m/s	-	Stiff spring velocity
D_{media}	2.5×10^{-9} m ² /s	[153]	Diffusion coefficient, oxygen in growth media
D_{PDMS}	3.4×10^{-9} m ² /s	[152]	Diffusion coefficient, oxygen in PDMS
C_{media}	0.206 mol/m ³	Calculation	Saturation concentration of oxygen in growth media
C_{PDMS}	1.69 mol/m ³	[153]	Saturation concentration of oxygen in PDMS
C_{air}	8.27 mol/m ³	Calculation	Concentration of oxygen in 35 °C air
$K_{P,air}$	8.20	Calculation	Partition coefficient, air/PDMS
$K_{P,PDMS}$	4.89	Calculation	Partition coefficient, PDMS/growth media
V_{O_2}	4.31×10^{-20} mol/cell/s	[154]	Rate of <i>E. coli</i> K-12 consumption of oxygen
ρ_{cell}	5×10^{11} cells/m ²	Calculation	Area density of cells on bottom of channel
U_0	6.0×10^{-5} m/s	Calculation	Normal inflow velocity with 7.5 $\mu\text{L/hr}$ flow rate
L	2.4 cm	-	Channel length
w	350 μm	-	Channel width
h	100 μm	-	Channel height
Q	7.5 $\mu\text{L/hr}$	-	Volumetric flow rate
t	4.9 mm	-	PDMS thickness

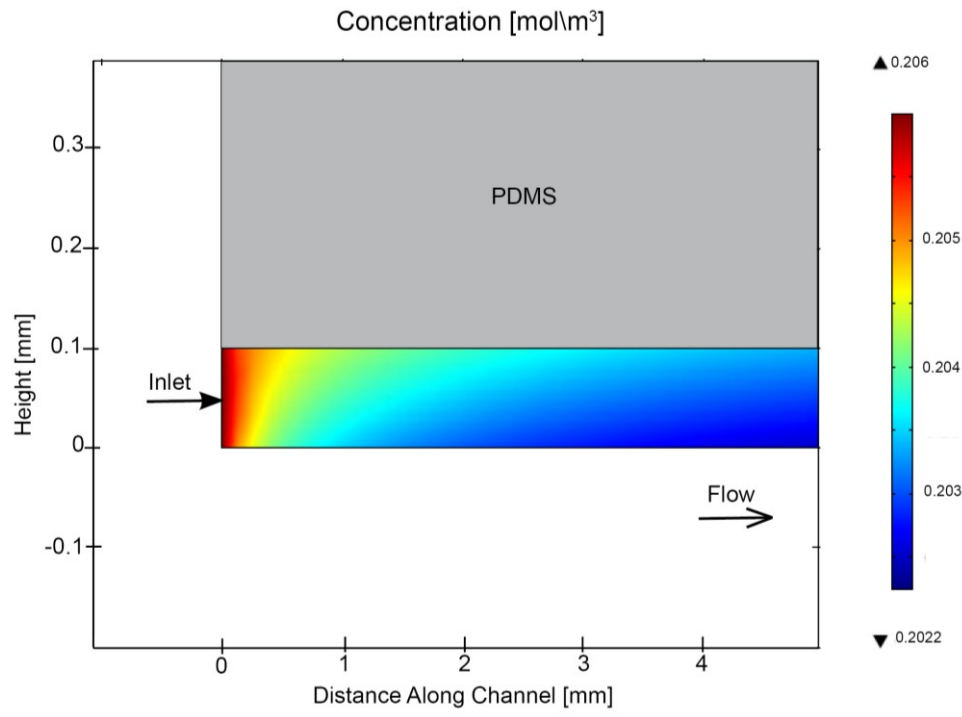


Figure 4.4. Detail of oxygen concentration within growth media near the channel inlet from steady state COMSOL simulation of oxygen transport in the microfluidic system. The simulation was based on the conceptual model of Figure 4.3 and used the parameters in Table 4.1.

These results showed that the bacterial oxygen consumption rate is not large enough to fully deplete the media. Close to the inlet, the primary source of oxygen for bacterial consumption is convection of oxygen dissolved in the growth media. After an initial entry length, oxygen diffusion through the PDMS channel ceiling supplements oxygen convection [153]. The diffusive transport of oxygen allows the concentration along the bottom of the channel to approach a constant value of 0.2022 mol/m^3 , only 1.8% less than the saturation concentration of oxygen in LB media. Although oxygen in the media is consumed, it is at a low rate and has a minimal impact on the bulk oxygen concentration.

While the above simulation provides general insight into the dynamics of microfluidic biofilm reactors, the biofilm growth rate and composition must be more

thoroughly accounted for, as in mathematical models presented in literature [32, 155], for a true representation of oxygen transport and reaction in the system. For example, a biofilm whose biomass contains both live and dead bacteria will have a lower effective metabolic rate than a biofilm composed entirely of live bacteria. Diffusion through the biofilm matrix itself must also be accounted for, as bacteria at different depths experience dissimilar oxygen and nutrient environments and accordingly exhibit different growth rates. Growth of the biofilm also physically alters the system, effectively reducing the hydraulic diameter. As this device was designed for end-point characterization of mature biofilms, the use of the above simplified model to verify sufficient oxygen throughout the channel is adequate for the purposes of this work.

4.2 Fabrication

4.2.1 Overview

The channel profiles in both PDMS layers were created using photoresist molds patterned photolithographically on a silicon wafer. Schematics of the device layout indicating the mask layers used are shown in Figure 4.5. The fluidic channels were 350 μm wide, and the central channel through which biofilms were grown was 24 mm long.

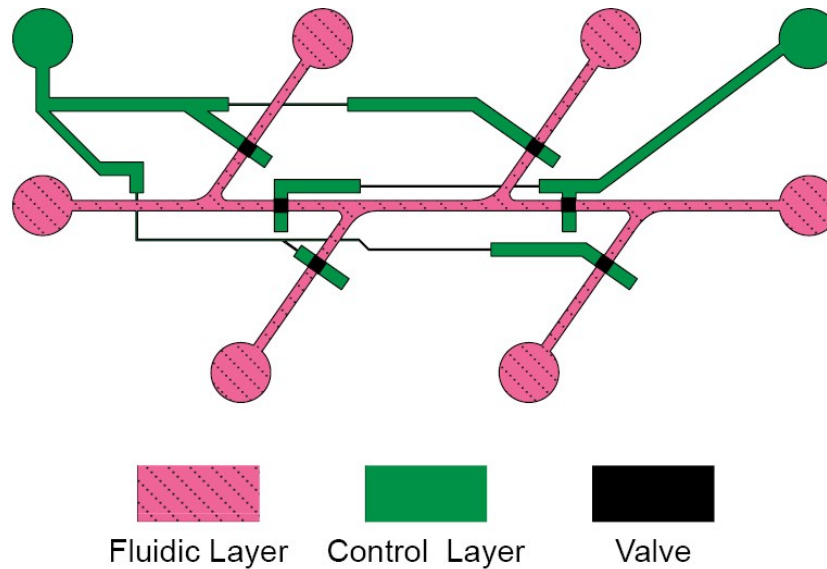


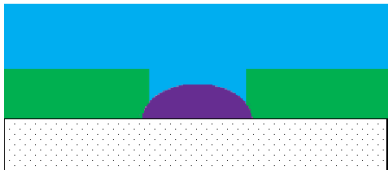







Figure 4.5. Mask layout for PDMS molds. Pink channels denote the top, biofilm-containing layer, and green channels denote the bottom, hydraulic control layer. Valve locations are indicated by black squares at the intersections of the pink and green channels. Drawn to scale.

An overview of the entire fabrication process is given in Table 4.2; details of key fabrication parameters and intermediate steps are presented in the subsequent section. Briefly, to form a mold for the biofilm growth and valving layer, first a thin photoresist (AZ 9260) was patterned and rounded to form the shallow areas for valving. While a negative-tone photoresist could be used in place of the AZ 9260, it cannot produce the rounded profile needed for valve sealing. A thicker photoresist (Microchem KMPR 1050) was patterned on top of the AZ 9260 to form the areas for biofilm growth. This structure was then used as a mold to generate the inverse of this pattern in PDMS. The mold for the other PDMS layer, providing control of the valves, was formed by a single layer of KMPR 1050. The two PDMS layers were stacked on top of each other and bonded together, then bonded to a coverslip to generate the entire structure.

Table 4.2. Process flow of the PDMS molding and assembly process.

Step	Cross-Sectional View
1) Photolithography and rounding of thin positive photoresist (AZ 9260).	
2) Photolithography of thick, negative photoresist (KMPR 1050) for biofilm growth areas.	
3) PDMS is poured onto the 2-depth fluidic mold.	
4) PDMS is peeled off the mold.	
5) In parallel, a separate mold for the control channel is fabricated from KMPR 1050.	
6) PDMS is spun onto the control channel mold and cured.	
7) Peeled 2-depth fluidic PDMS is aligned to and placed on top of the spun PDMS, creating a two layer PDMS stack on top of the control channel mold. After curing the layers together, the PDMS stack can be peeled off and bonded to a glass substrate.	
	

4.2.2 Fluidic Mold Fabrication

4.2.2.1 AZ 9260 Patterning and Hardbake

The standard AZ 9260 patterning and rounding process involved spinning, developing, and exposing the resist to obtain the overall pattern, then baking it above its reflow temperature in order to form rounded structures. In developing the fabrication

process, it was found that the first layer of photoresist patterned, AZ 9260, was very sensitive to subsequent patterning of the thicker layer of photoresist, KMPR 1050, on top of it. The AZ 9260 typically dissolved during the KMPR 1050 development in SU-8 developer. A hardbake was implemented to counteract this to reduce solubility by exposing the photoresist to higher temperatures and longer periods of time than imposed by standard AZ 9260 rounding procedures (2 minutes at 120 °C, as described in [156, 157]). However, AZ 9260 would often crack during either the hardbake, one of the KMPR bakes, or the exposure to SU-8 developer. While the general shape of the AZ 9260 would remain, the cracks rendered the pattern unusable as a PDMS mold. Since PDMS is viscous before it is cured, it fills any cracks and sticks within the cracks during curing. When the PDMS was peeled off the wafer, the cracked AZ 9260 was peeled off along with the PDMS, as shown in Figure 4.6.

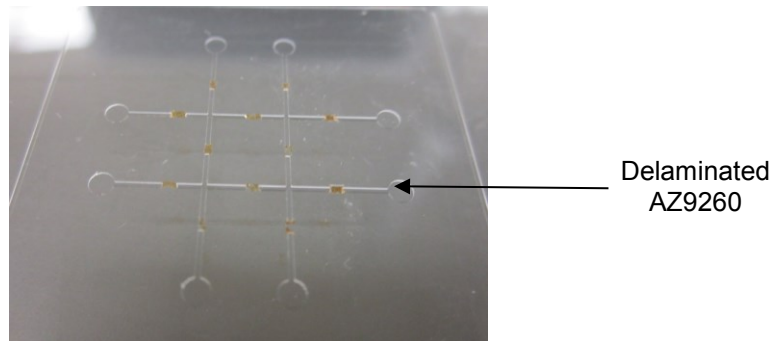


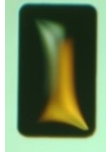









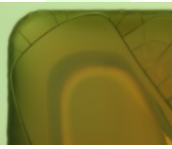


Figure 4.6. Photograph of PDMS molded with the 2-depth AZ 9260/KMPR mold. Brown squares of cracked AZ 9260, indicated by the arrow, delaminated off the wafer and became stuck in the channels in the PDMS. The AZ 9260 residues could not be removed from the PDMS without severely damaging the microfluidic channel.

Initially, hardbake parameters were altered to investigate a potential solution to the cracking, as baking positive photoresist too quickly or at too high a temperature may produce temperature gradients that can crack the resist. However, the resist must be baked to a sufficient degree to prevent dissolution in SU-8 developer. Hardbake parameters that reliably produced patterned AZ 9260 without cracks were identified

through iterative, chip-scale experiments. Variables altered during this process include bake temperature, bake time, temperature ramping up or down from the bake, and the presence of a cover (inverted glass petri dish creating a chamber) over the chip. Success of a hardbake was evaluated by immersing a patterned chip in SU-8 developer for 5 minutes, with agitation. Table 4.3 provides examples of the parameters altered and corresponding photographs of AZ 9260 test patterns throughout the process.

Table 4.3. Parameters varied in AZ 9260 hardbake characterization, including temperature, time, and whether the chip was covered during the bake. Corresponding photographs were obtained after the hardbake and after immersing the chip in SU-8 developer for 5 minutes. The red box highlights parameters used in further process development.

Temperature (°C)	Time (min)	Covered	After Hardbake	After 5 min SU-8 Developer
160	60	No		(dissolved)
160	60	Yes		(dissolved)
170	20	Yes		
175	10	Yes		
175	15	No		(dissolved)
175	15	Yes		
175	20	Yes	 	 

By evaluating the yield of intact test structures after full processing, the bake parameters that produce the most reliable results were identified. The patterned wafer was placed on a room temperature hotplate, and the wafer was covered with an upside-

down Pyrex® petri dish. The wafer and petri dish were placed off-center on the hotplate surface so that a small section of the dish protruded from the edge of the hotplate, providing an opportunity for solvent evaporation. The hotplate was then allowed to heat up to 175 °C for approximately 8 minutes, held at that temperature for 20 minutes, then allowed to cool naturally to room temperature, at which point the cover and wafer were removed. However, even without cracks after the hardbake, subsequent exposure to SU-8 developer still damaged the patterned AZ 9260, as in the last row of Table 4.3, with a yield of approximately 50%. The introduction of a passivation layer improved yield by protecting the AZ9260 from SU-8 developer exposure, as discussed in the next section.

The process parameters for the AZ 9260 processing and hardbake that were used in all of the following work are presented in Table 4.4.

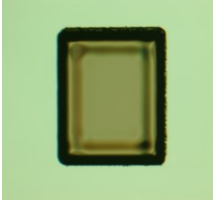
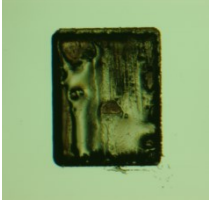
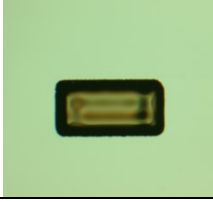
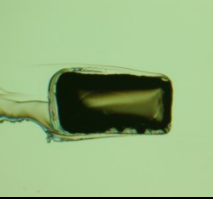
Table 4.4. Table of processing steps and parameters used for AZ 9260 lithography, rounding, and hardbaking.

Step	Parameters	Description
Spin HMDS	3000 rpm, 30 s	Adhesion layer deposited immediately on dehydrated wafer
Bake	150 °C, 3 min	HMDS activation, solvent evaporation
Spin 1 st AZ 9260 Layer	2000 RPM Ramp: 2 s Time: 60 s	Spin dispense; creates film ~11 μm
Bake	Room temperature, 15 min 60 °C, 5 min 100 °C, 5 min	Evaporate solvent
Spin 2 nd AZ 9260 Layer	1500 RPM Ramp: 2 s Time: 60 s	Spin dispense; Creates final film thickness ~ 24 μm
Bake	Room temperature, 15 min 60 °C, 5 min 100 °C, 20 min	Evaporate solvent
Rehydration	>24 hours	Rehydration time based on humidity
Exposure	600 mJ/cm ² @ 365 nm	Expose with Mask #3 (Appendix A) in intervals to avoid bubbles
Develop	4:1 AZ400k, 10 min	May rinse off residues with additional dip in fresh 4:1 AZ400k
Hardbake	175 °C, 20 min Default hotplate ramp to bake temperature, natural cooldown.	Solvent evaporation and profile rounding. Cover wafer with upside-down petri dish protruding from hotplate.

4.2.2.2 ALD Passivation of AZ 9260

As an alternative to simply patterning the two photoresists one after the other, passivation of the first layer was investigated. There are multiple methods used in literature for passivation of photoresist, including creating a crosslinked photoresist “skin” using UV ozone or chemical treatments [158, 159]. UV-ozone curing was attempted using a UVOCS ® T10X10 UV Ozone Cleaner and the parameters listed below in Table 4.5. However, this treatment did not significantly decrease the amount of AZ 9260 degradation.



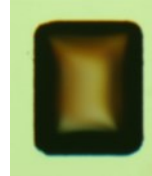
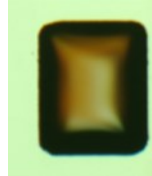

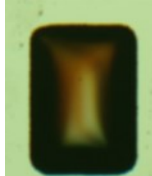


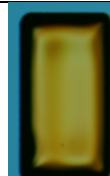





Table 4.5. UV-ozone curing parameters and corresponding images of AZ 9260 structures after the hardbake (before UV-ozone exposure) and after testing stability by exposure to SU-8 developer. UV-ozone exposure was performed in multiple steps to prevent overheating and bubbling of the resist; chips were exposed to 1 minute of UV-ozone, then allowed to cool for 1 minute.

Total UV-Ozone Exposure Time	After Hardbake	After 2 min SU-8 Developer
20 min		
30 min		

In contrast to altering the photoresist itself to increase its chemical resistivity, others have used metal as a thin barrier layer in multiple process steps using the same photoresist [160]. Additionally, our group has demonstrated the passivation of a biosensor from biological media using atomic layer deposition (ALD) of aluminum oxide [113]. ALD materials deposition is suited for passivation of photoresist structures not only because it is thin and conformal, preserving the rounded shape of AZ 9260, but also allows for low temperature deposition, preventing thermal stresses on the resist.

ALD deposition of Al₂O₃ over patterned, rounded AZ 9260 test structures was deposited using a 150 °C process in a Beneq TFS 500 as in previous work [113]. The passivation ability of the ALD Al₂O₃ was characterized using two different layer thicknesses – 45 nm and 95 nm. The quality of the passivation was evaluated by immersing chips with patterned AZ 9260 in SU-8 developer after passivation. As shown in Table 4.6 below, 45 nm of Al₂O₃ still appeared to be insufficient to passivate against SU-8 developer; 95 nm of Al₂O₃ appeared to passivate the majority of the test chips adequately.

Table 4.6. Chart depicting different squares on different test chips after deposition of the Al₂O₃ layer, and after immersing the chip in SU-8 developer for the time interval specified in the top row. (a) Chips with 45 nm of Al₂O₃ passivation; (b) Chips with 95 nm of Al₂O₃ passivation.

ALD Al ₂ O ₃ Thickness	After ALD	6 min SU-8 Developer	8 min SU-8 Developer	20 min SU-8 Developer	Yield
45 nm					8/12
			(dissolved)		
95 nm					46/48
					

When the Al₂O₃ failed, as in the 45 nm cases, the AZ 9260 structures completely dissolved, occasionally leaving residue on the wafer. The two failed patterned structures

seen in the 95 nm Al₂O₃ samples still possessed intact patterns, albeit with cracks. However, since the 20 minute immersion period used is much longer than the actual 5-10 minute development needed for 100 μm thick KMPR, a higher yield in fabricating the multi-depth mold was expected. For the remainder of this work, patterned and hardbaked AZ 9260 was protected by an ALD Al₂O₃ passivation layer deposited at 150 °C with a target thickness of 95 nm.

4.2.2.3 KMPR Patterning

Using the parameters for the AZ 9260 lithography, hardbake, and passivation with ALD Al₂O₃ as presented above, the parameters for the KMPR 1050 processing were finalized. Detailed procedures for this process are presented in Table 4.7.

Table 4.7. Table of processing steps and parameters used for KMPR 1050 lithography on top of patterned and passivated AZ9260.

Step	Parameters	Description
Bake	150 °C, 5 min	Dehydrate wafer surface
Spin KMPR1050	500 RPM Ramp: 4 s Time: 10 s 1000 RPM Ramp: 3 s Time: 30 s	Creates film ~100 μm
Pre-exposure Bake	95 °C, 25 min	Evaporate solvent
Expose	1000 mJ/cm ² @ 365 nm	Expose with Mask #4 (Appendix A)
Post-exposure Bake	95 °C, 6 min	Cross-links photoresist
Develop	SU-8 Developer, 6 min	Isopropanol rinse after develop complete

A summary of the entire fabrication process for the fluidic mold is presented in Figure 4.7 along with representative photographs taken after each of the steps was performed.

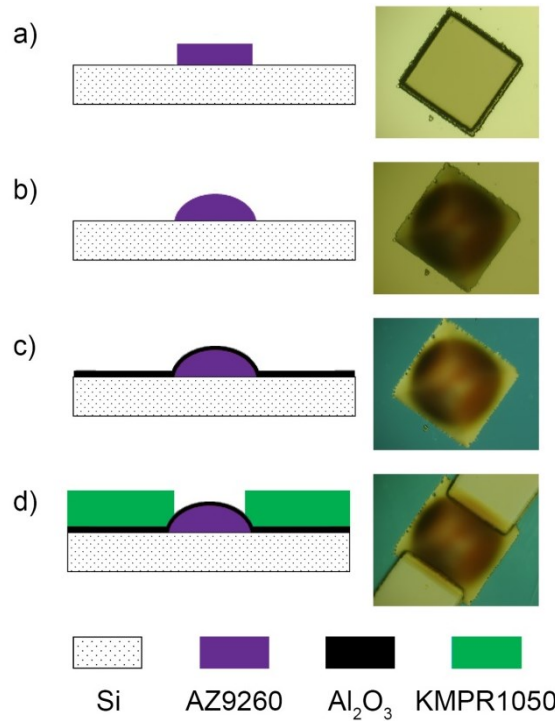


Figure 4.7. Cross-sectional schematics and corresponding photographs of fluidic mold fabrication: a) patterning of AZ 9260 positive resist, b) resist rounding and hardbake, c) passivation with ALD Al₂O₃, and d) KMPR 1050 patterning.

4.2.3 Hydraulic Control Mold Fabrication

The mold for the bottom layer of PDMS containing the valve control channels was fabricated from a single layer of Microchem KMPR 1050 patterned on a silicon wafer. The thickness of the resist was not as critical as the thicknesses in the fluidic mold; the most critical feature was the PDMS membrane spun on top of the control mold, and given control of the PDMS thickness on top of the control mold, the thickness of the mold itself was less important. A KMPR 1050 thickness of 40 μm produced membranes of appropriate thickness using the PDMS spin procedure described later in this chapter. The final process parameters for the KMPR 1050 processing for the hydraulic control mold are presented in Table 4.8.

Table 4.8. Table of processing steps and parameters used for KMPR 1050 lithography to create hydraulic control channels.

Step	Parameters	Description
Bake	200 °C, 10 min	Dehydrate wafer surface
Spin KMPR1050	500 RPM Ramp: 4 s Time: 10 s 2000 RPM Ramp: 3 s Time: 30 s	Creates film ~40 μm
Pre-exposure Bake	95 °C, 20 min	Evaporate solvent
Expose	1000 mJ/cm ² @ 365 nm	Expose with Mask #5 (Appendix A)
Post-exposure Bake	95 °C, 5 min	Cross-links photoresist
Develop	SU-8 Developer, 5 min	Isopropanol rinse after develop complete

4.2.4 PDMS Layer Fabrication and Bonding

Prior to pouring or spinning PDMS onto a mold wafer, the mold must be treated with a release agent to prevent PDMS adhesion to the features on the wafer, or breakage of the entire wafer while attempting to remove the PDMS. The first release agent tried involved vapor phase deposition of a chlorosilane layer on the wafer surface by exposure to trimethylchlorosilane in a vacuum dessicator. Upon exposure of the vapor to silicon dioxide on the wafer, silanol groups bond to the wafer surface. The resulting coating is very stable and reduces the surface energy, allowing PDMS to be peeled from the mold during subsequent steps. While this process has been performed previously within the MEMS Sensors and Actuators Laboratory at the University of Maryland [157], vapor phase silanization did not repeatably create an adequate release layer for this device, most often observed by permanent adhesion of PDMS to the Al₂O₃-passivated, multi-depth mold. After accounting for variables such as silanization time and age of the trimethylchlorosilane solution, environmental factors were most likely responsible for the poor PDMS release. Experimentation with release layers was performed during high

humidity weeks in the spring; however, silanization is very humidity sensitive, as silanes react readily with water. While this may not be a critical factor for silicon silanization, Al₂O₃ silanization may be more sensitive and therefore did not succeed even when molds with silicon substrates were silanized in the same environmental conditions. It is likely that molecular water on the Al₂O₃ surface reacts with the silane vapor before the hydroxyl groups on the Al₂O₃ surface react with the vapor. Although standard silanization is an effective procedure for most PDMS molds, it was necessary to identify an alternative less sensitive to ambient humidity and more compatible with Al₂O₃.

Detergent treatments have also been used as a surface treatment to promote PDMS release [161]. This process was adapted as a replacement for silanization to prevent PDMS adhesion to patterned mold wafers in this work. Both molds were treated with an aqueous solution of Alconox® powdered precision cleaner prior to PDMS processing to prevent PDMS adhesion to the mold surface. Wafers were placed in a petri dish with 0.75% Alconox® detergent dissolved in deionized (DI) water for 2 minutes, removed, and allowed to air dry.

PDMS for the control channel layer was mixed in a ratio of 20:1 (base : curing agent) and degassed in a vacuum dessicator. The mixture was spun on top of the prepared control channel mold using a spin dispense, then spinning it at 1050 rpm for 90 seconds. The wafer was placed in a furnace programmed to ramp to 60 °C in 5 minutes, then hold at 60 °C for 15 minutes.

PMDS for the fluidic channel layer was mixed in a ratio of 5:1 (base : curing agent) and degassed. The mixture was poured on top of the prepared fluidic channel mold, and the wafer placed in a furnace programmed to ramp to 60 °C in 5 minutes, then

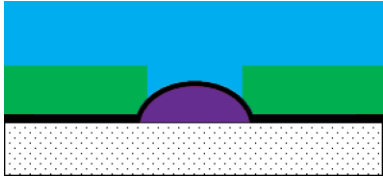






hold at 60 °C for 15 minutes. After curing, the PDMS was peeled off of the fluidic channel, and each chip was cut out of the wafer-sized PDMS piece using a knife. A 2 mm dermatological punch was used to punch holes at the inlets and outlets for fluidic tubing.

After both PDMS layers were cured, each fluidic channel PDMS chip was aligned to and placed on top of the control channel mold with the spun PDMS cured on top. A microscope was used to aid in alignment of each chip to the pattern on the control channel mold wafer. The PDMS stack on top of the control channel mold wafer was placed in a furnace programmed to ramp to 80 °C in 10 minutes, then hold at 80 °C for 3 hours. The different base : curing agent ratios (20:1 in the control channel layer, 5:1 in the fluidic channel layer) create an excess of one of the components in each layer. Excess molecules are believed to interact with each other at the interface between the two layers, encouraging formation of a PDMS-PDMS bond [162]. After cooling the stack to room temperature, a knife was used to cut around the outline of each chip. The entire PDMS stack for each chip was then carefully peeled off of the control channel mold. A 2 mm dermatological punch was used to punch holes at the inlets for the pressurized nitrogen used to control the valve actuation.

After each of the PDMS chips on the wafer had been removed from the mold, they were permanently bonded to glass coverslips using oxygen plasma bonding. Each PDMS chip and coverslip was placed in the chamber of a March Jupiter III O₂ Plasma System with the surfaces to be bonded together oriented toward the plasma source. In the final device fabrication process, surfaces were exposed to oxygen plasma for 30 seconds at 20 W and approximately 450 mTorr. The coverslip was removed from the chamber

and the PDMS stack carefully placed on top. Any bubbles were pressed out of the interface between the PDMS and glass as soon as possible after contact. The plasma bond was strengthened by baking the devices in a furnace at 60 °C for 3 hours. The entire PDMS layer fabrication and bonding procedure is detailed in Table 4.9.

Table 4.9. Process flow of the final PDMS molding and assembly process.

Step	Cross-Sectional View
1) PDMS is poured onto the 2-depth fluidic mold.	
2) After curing, PDMS is peeled off the mold.	
3) PDMS is spun onto a separate mold for the control channel, and cured.	
4) The peeled multi-depth fluidic PDMS is aligned to and placed on top of the spun PDMS.	
5) After curing the two layers together, the PDMS stack is peeled off of the control channel mold.	
6) The PDMS stack is permanently bonded to a glass coverslip using oxygen plasma bonding.	
	

Fluidic connections were made to the device as described in Chapter 2. Holes were punched in the PDMS with a 0.2 mm dermatological punch. Barbed tubing connectors (1/16") were inserted into the resulting holes and connected with Tygon® tubing to either a syringe pump operating in infusion mode, or a microcentrifuge tube serving as a waste reservoir.

4.3 Device Preparation and Testing

4.3.1 Device Preparation

When pressurized nitrogen was applied to an empty, non-liquid-filled control channel, the nitrogen gas diffused through the thin PDMS membrane at the valves and emerged in the fluidic channel as a bubble, interrupting flow and delaminating adherent biofilms. Therefore, the first step in preparing the device for experimentation was conversion of the pneumatic channels into hydraulic channels by pre-filling them with DI water mixed with a drop of standard food coloring. Tubing connected to the control channel inlets was coupled to a filled syringe dispensing dyed DI water at a flow rate of 20 $\mu\text{L/hr}$. Injection of the water forces gas in the control channel to diffuse through the membrane as it is replaced by the liquid. As the control channels lack outlets, injection of dyed water was stopped when it was visually confirmed to have reached the ends of the channels. The tubing connected to the control channels was subsequently connected to a tank of controlled, pressurized nitrogen. To close the valves, a nitrogen pressure of 15 psi was applied to the hydraulic channel, and the valves were opened by releasing this pressure.

4.3.2 Operation: Biofilm Growth

Channels were sterilized using 70% ethanol at a flow rate of 20 $\mu\text{L/hr}$ to introduce into the channels. After rinsing the device with DI water at 20 $\mu\text{L/hr}$, the device was set to the biofilm growth configuration as in Figure 4.1a. The *E. coli* strains used were BL21 pGFP and K-12 MG1655. The former was used for rapid characterization of biofilms formed, since it constitutively expresses green fluorescent protein (GFP) so staining was not required for fluorescence microscopy. Wild type *E. coli* MG1655 was used as a model of wild type biofilm dynamics, and can only be imaged in conjunction with fluorescent stains. All biofilms were initiated from cultures grown overnight at 250 rpm and 37 °C and diluted to an OD_{600} of 0.25 in LB media. Suspensions were injected into the center channel of a sterilized device just until it was filled. The suspension was incubated in the device under static conditions for 2 hours in a 37 °C incubator to allow bacterial adhesion to the PDMS channel floor. With the device remaining in the incubator, flow of sterile LB growth media at 7.5 $\mu\text{L/hr}$ was initiated after the incubation period and applied continuously for the set time period of biofilm growth.

4.3.3 Operation: Biofilm Segmentation

In the presented biofilm segmentation studies, biofilms were grown as previously described. After the set period of biofilm growth time, the valve orientation was switched by releasing the pressure from the valves blocking the side channels, and applying pressure to the channels controlling the valves in the center channel. Each section could then be exposed to treatment as shown in the schematic in Figure 4.1b; in this demonstration of the device's applicability to biofilm studies, two sections were exposed to two different SDS concentrations (0.1% and 0.2% in LB media) at 7.5 $\mu\text{L/hr}$

for one hour, and one section was maintained as a control via exposure to LB media at 7.5 $\mu\text{L/hr}$ for one hour.

4.3.4 Staining, Confocal Microscopy, Image Analysis

Biofilms were stained, imaged, and analyzed based on the procedures developed in Chapters 2 and 3 [118, 119]. After biofilm formation or treatment, biofilms were rinsed with DI water then stained with the FilmtracerTM LIVE/DEAD[®] Biofilm Viability Kit (Molecular Probes, Inc.), using equal proportions of SYTO9 and propidium iodide introduced into the biofilm-containing channels at a flow rate of 7.5 $\mu\text{L/hr}$. The biofilms were rinsed again with DI water and imaged using confocal microscopy (Zeiss LSM 710). One location was imaged in each of the three segments per device; images were obtained close to the center point of each segment, approximately 4 mm away from the valve areas. Confocal image stacks were quantitatively analyzed using COMSTAT [95], and visualized using Imaris (Bitplane, Inc.). JMP[®] statistical analysis software was used for all statistical calculations.

4.4 Results and Discussion

4.4.1 Fabrication of Multiple Channel Profiles

Deposition of a physical and chemical barrier via ALD proved a reliable method for patterning multiple resist formulations and profiles. Using the methods described above, a 100% yield of intact AZ 9260 was obtained repeatably. Successful patterning of the two photoresists to obtain the desired profiles is depicted by the profilometry data and scanning electron microscopy (SEM) image in Figure 4.8a-b. A photograph of the finished mold is also included in Figure 4.8c.

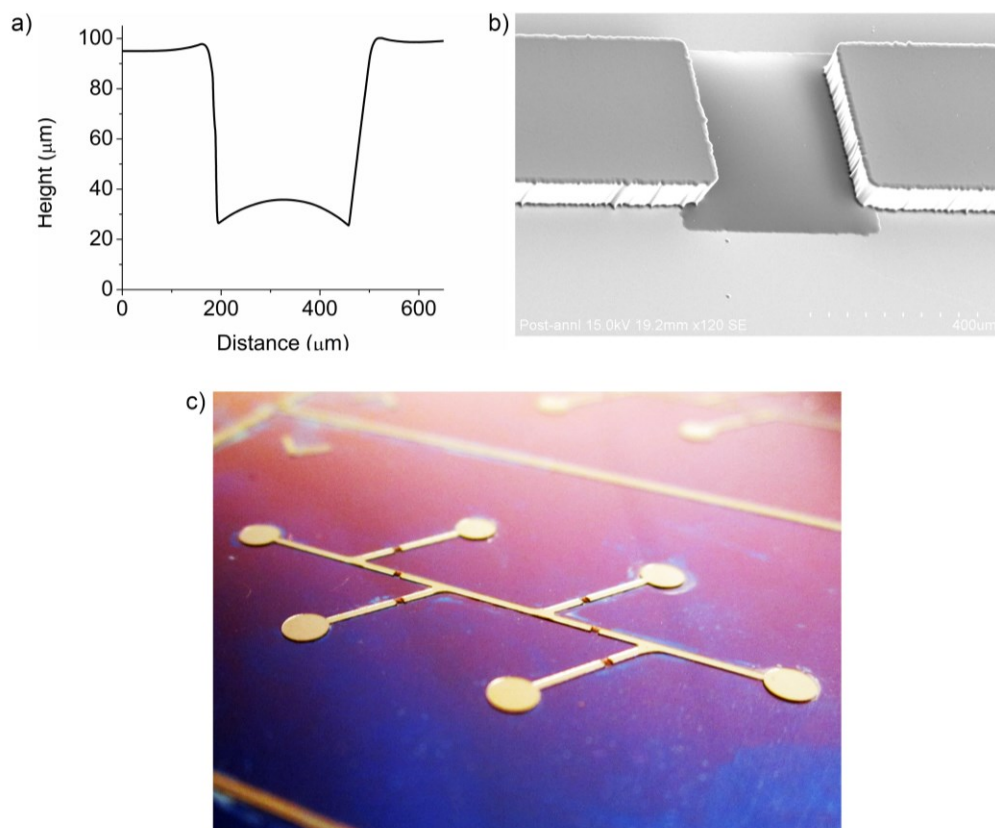


Figure 4.8. a) Contact profilometry scan of mold at valve region, verifying the presence of the desired profiles. In the measured region, the rounded AZ 9260 section had a peak height of 36 μm , and the KMPR 1050 channels had a depth of approximately 97 μm . b) SEM image of multi-depth structure created from two photoresists. Note the large difference in aspect ratios minimizes the appearance of curvature in the shallow section. c) Photograph of multi-depth mold.

In order to create the device presented here, a new technique for protecting photoresist from chemical attack by solvents was developed. This enabled multi-depth, multi-profile microfluidic channels. While this demonstration of the technique only employed two types of resist, a multitude of photoresists or other polymeric materials with different patterning capabilities or thicknesses may be used to create varied microchannel geometries. Using ALD passivation allows researchers the freedom to use any polymeric materials regardless of compatibility. As the body of research on ALD processing expands, there are an increasing number of methods for low-temperature deposition of a variety of materials [163, 164], which in turn may be used for passivating

polymers more sensitive to high temperatures. The ability to deposit very thin layers of high quality material facilitates the creation of even finer passivated photoresist patterns than those demonstrated here (on the order of 100 μm). The fabrication technology of ALD passivation of photoresist to create multi-depth, multi-profile microfluidics also can be applied to an even broader number of applications outside the field of bacterial biofilms. Microfluidics with mixed profiles can be applied to the growing number of tissue culture studies in microenvironments. Microfluidic channels can be created to mimic *in vivo* spaces where tissue might form or be implanted [165]. Channels featuring deliberately patterned obstacles to flow could contribute an additional tool for understanding shear environments around *in vivo* perturbations such as atherosclerotic lesions [166]. Multi-depth microfluidics would also be useful in hydrodynamic studies where the channel dimensions would affect the results. For example, the presence of a “ceiling” above an electrochemical sensor in a microfluidic channel has been shown to affect the sensor output [167]; this phenomenon could be further investigated by evaluating sensor performance in channels of different depths. While this could be accomplished in a series of devices, each with its own unique channel depth, using one device with multiple channels and sensors not only eliminates device-to-device variability, but is more efficient and streamlined for the researcher.

4.4.2 Valve Functionality

The functionality of the valves was confirmed by introducing flow of DI water dyed with food coloring, then activating and releasing valves to control flow localization. Sample results of two device assessment tests are presented in Figure 4.9 and Figure 4.10. In one test, shown in Figure 4.9, one set of valves was actuated to create one

central channel, and green-colored water was injected into the device. The valve configuration and the resulting flow pattern are shown in Figure 4.9b. The valve orientation was then reversed, segmenting the channel into three sections. Two sections were rinsed with undyed water (Figure 4.9c), then filled with different colors of water (Figure 4.9d), while the first section was not rinsed and maintained as a control.

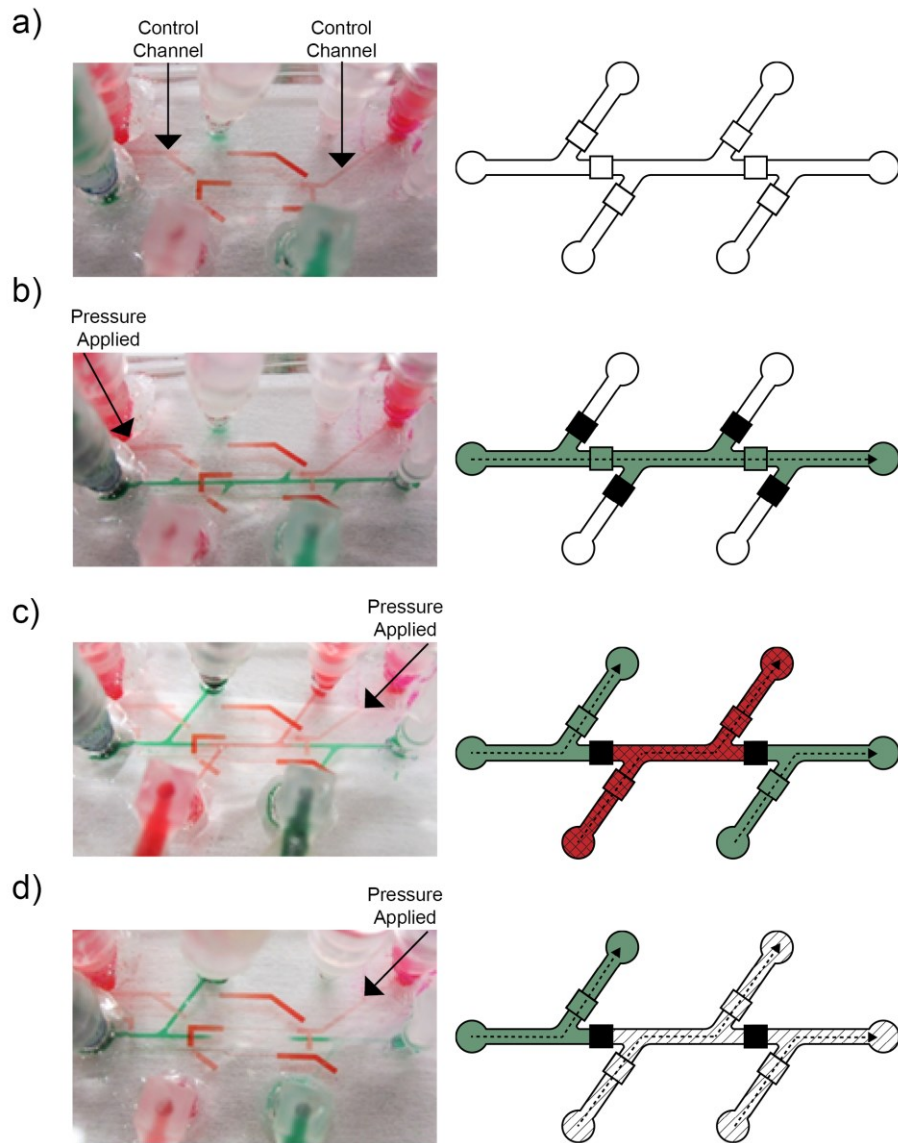


Figure 4.9. Photographs (left column) of the device taken at different stages over a several-hour testing period, and diagrams (right column) illustrating flow patterns and valve configurations, where solid black squares indicate closed valves. a) Filling the hydraulic control channels with red-dyed water, leaving the fluidic channels empty. b) Actuating one set of valves and creating flow through the center channel in the fluidic layer. c) Reversing valve orientation and rinsing out two of the three new channels with undyed DI water. d) Creating different flows in each of the three segmented channels.

In a separate test (Figure 4.10), three different colors of water were used to simulate operation as a biofilm segmentation and testing device as postulated in Figure 4.1a-b. The use of dyed water also allowed for qualitative evaluation of leakage through valves between sections, as leaks became manifest by the mixing of colors.

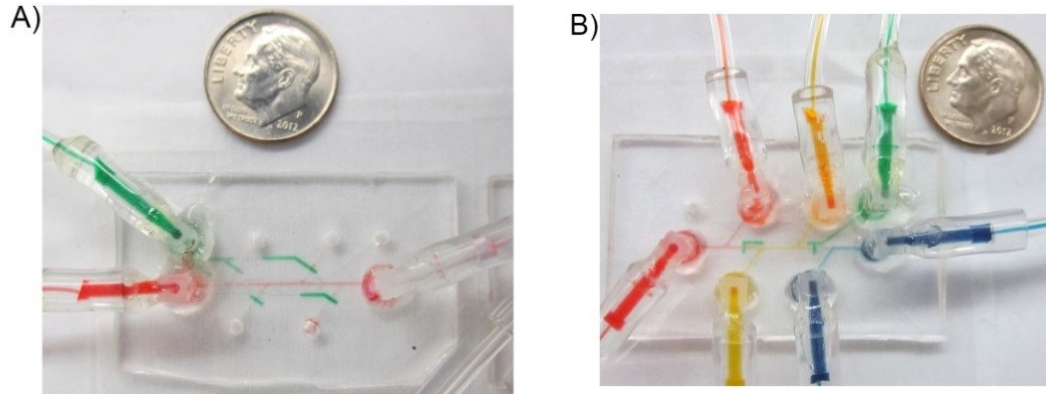


Figure 4.10. Photographs of assembled devices with green water filling actuated control channels. a) Device in biofilm growth orientation, with side channels blocked by closed valves. Photograph corresponds to Figure 4.1a. b) Device in biofilm sectioning orientation, with side channels open and central channel sectioned by closed valves. Photograph corresponds to Figure 4.1b.

4.4.3 Biofilm Uniformity

In order to use the device for biofilm studies with integrated controls, biofilms grown in the center channel must be uniform so that upon segmentation, the control section may be compared to the experimental sections in good faith knowing that prior to segmentation, all sections were comparable. One concern was that the shallow valve areas might easily become clogged with biofilm, preventing further flow of growth media and biofilm growth beyond the clog. However, this proved not to be the case, since biofilms preferentially did not grow in the valve area. This is demonstrated by the images shown in Figure 4.11, where *E. coli* BL21 pGFP was grown in the center channel for 60 hours, and the control channels were filled with DI water and red food coloring, which has its own fluorescent signal.

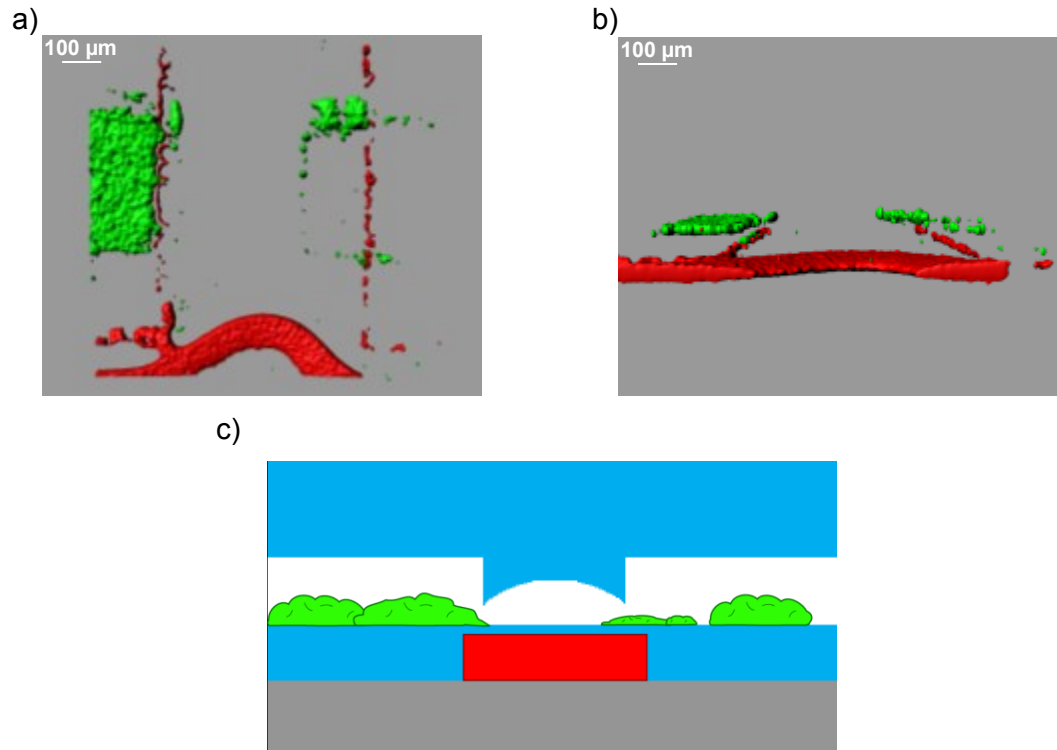


Figure 4.11. Surface reconstruction of confocal microscopy of 60-hour *E. coli* BL21 pGFP biofilm within the microfluidic channel. Bacteria showed only green fluorescence; red areas are residual red food coloring absorbed into PDMS or the air-colored water interface in the control channel. The red food coloring is visible due to its intrinsic low-level fluorescence. a) Top view b) Angled view from side, c) Schematic representation of confocal images in the context of the layered PDMS channels. Hydraulic control channel is depicted as completely filled with red-dyed water, whereas during confocal microscopy the water receded toward the open fluidic ports, leaving behind fluorescent residue.

The lack of bacterial growth within the valve area was most likely due to the increased amount of shear stress in the narrow parts of the channel at the transition between the KMPR 1050 and AZ 9260 sections of the channel mold. The shear stress in the center of the valve region, where the channel was deepest at approximately 35 μm , is about 8-fold greater than the shear stress in the 100 μm -deep biofilm growth areas. Increased shear imposed on the biofilm can reduce its thickness and can inhibit overall growth.

Having verified that biofilms could be grown without clogging the shallow valve areas, uniformity was verified by growing *E. coli* MG1655 biofilms in the central channel

for 48 hours, then staining, imaging, and analyzing the biofilm in each of the three segments. The segments were denoted as I, II, and III corresponding to the segment closest to the inlet, the middle segment, and segment closest to the outlet as indicated in Figure 4.12a. Two of the devices, Devices 1 and 2 as shown in Figure 4.12b, were tested in parallel, while Device 3 was tested one month later. Results from the three devices tested are summarized in Figure 4.12b and samples of rendered confocal microscopy images from one device are shown in Figure 4.12c-e.

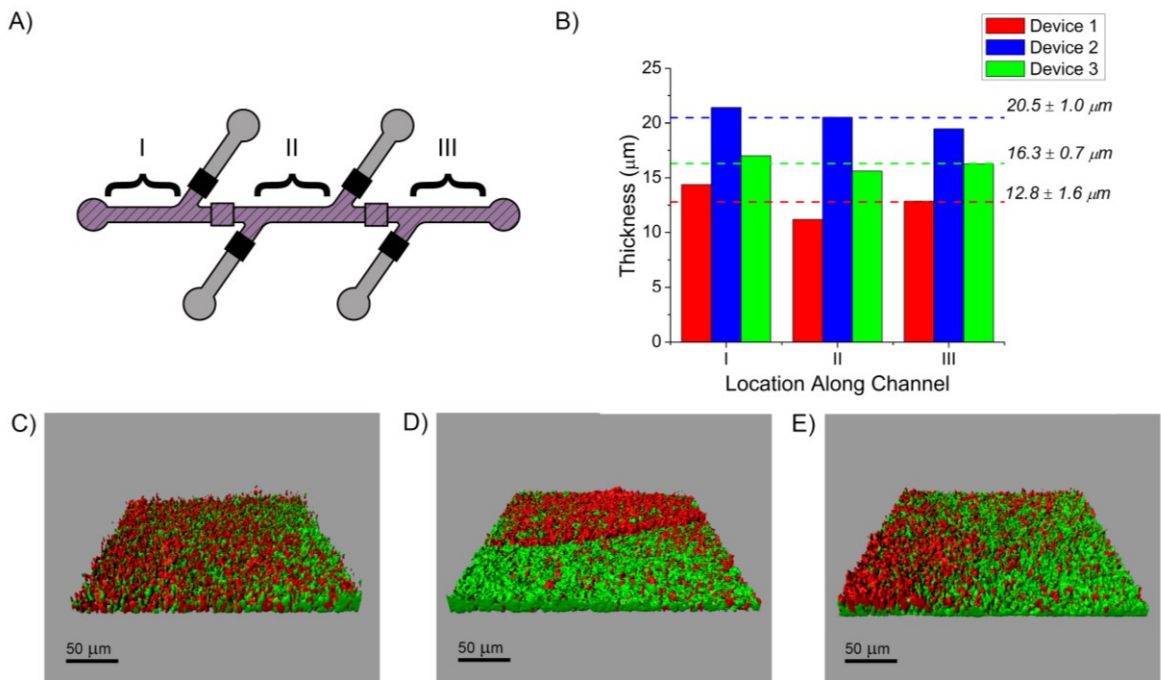


Figure 4.12. a) Schematic of device operation during biofilm growth, with side channels blocked by closed valves. Confocal microscopy images were obtained at the center of each of the three sections indicated (I, II, and III) b) Average biofilm thicknesses measured at imaged locations in the three devices tested. Locations were positioned in the center of each section, with Section I closest to the inlet, and III closest to the outlet. Dashed lines indicate averaged thickness across imaged locations for each device. c-e) Surface rendered confocal microscopy images from Device 3, Sections c) I, d) II, and e) III. Thicknesses were 17.0, 15.6, and 16.2 μm respectively.

The results show that biofilms had small thickness variations within each device (SD < 2 μm , 13% of the average thickness at greatest). Comparatively, this variation within a device was smaller than that between devices (SD = 3.9 μm , 23%). Using an

unweighted analysis of variance (ANOVA), the variance between devices was $9.82 \mu\text{m}^2$ (SE 2.25, P-value 0.8388), and the variance within a device between measurement locations was $0.61 \mu\text{m}^2$ (SE 0.67, P-value 0.0006). The smaller differences in average thickness over one channel as compared between the three devices highlighted the importance of an integrated control. These results confirmed that the biofilms were uniform throughout the center channel of each device, and had more uniform thicknesses than biofilms grown between devices.

While biofilm variability in general can partially be addressed by performing an experiment multiple times and examining data trends, implementing internal controls adds an additional level of scientific rigor. The need for these controls is clear in the device-to-device variation of biofilm thickness between devices in this work. Additionally, considering average thickness values obtained from devices prepared and tested at the same time varied similarly as devices tested on different dates, it is evident that between-device biofilm variation must be considered in experimental design. In this demonstration of the valved biofilm sectioning device, within-device biofilm variation was less than between-device variation, as evident in the ANOVA results. By comparing sections of one biofilm grown in one device, fewer iterations of an experiment would be required to obtain a representative understanding of the biofilm phenomena at play than if biofilms were grown in and compared between separate devices.

4.4.4 Biofilm Segmentation

The applicability of the device toward biofilm studies was demonstrated by testing biofilm sensitivity to SDS within a single device. SDS is an anionic surfactant that has been shown to denature the bacterial cell wall by solubilizing its phospholipid

and protein contents [130, 168]. Exposure of bacterial biofilms to SDS has been used as a gauge of biofilm health [56], as well as a method for preventing biofilm formation [169]. After growing *E. coli* MG1655 biofilms for 60 hours, the valve orientation was switched, dividing the center channel into three sections, as depicted in Figure 4.1b and Figure 4.10b. The three biofilm sections were either treated with 0.1% or 0.2% SDS, or remained untreated as a control. Two devices were tested in parallel; the location of each treatment within the device (i.e. Section I, II, or III as pictured in Figure 4.13a) was varied between the devices as described in Table 4.10. Results from the segmentation studies are summarized in Figure 4.13b, and samples of rendered confocal microscopy images from one of the devices are presented in Figure 4.13c-e. In both devices, the control biofilm was thickest, and increasing the SDS concentration decreased the measured thickness in the applicable segment. Additionally, there appeared to be no relationship between location of treatment administration and the results obtained; despite administration of treatments to biofilm segments at different locations within the device, both devices showed similar trends for thickness versus SDS concentration. This observation relied on the observed biofilm uniformity within the channel (Figure 4.12), which enabled the assumption that the control segment represented the initial state of the biofilms in the other two segments before SDS exposure. The results demonstrated the use of microfluidic devices to perform multiple, controlled experiments on a single biofilm.

Table 4.10. Summary of treatments applied to biofilm sections in each device, describing how positioning of treatments was varied between the two devices tested. Section I denotes the section closest to the inlet, and III denotes the section closest to the outlet.

Section	Treatment	
	Device 1	Device 2
I	Control	0.1% SDS
II	0.1% SDS	0.2% SDS
III	0.2% SDS	Control

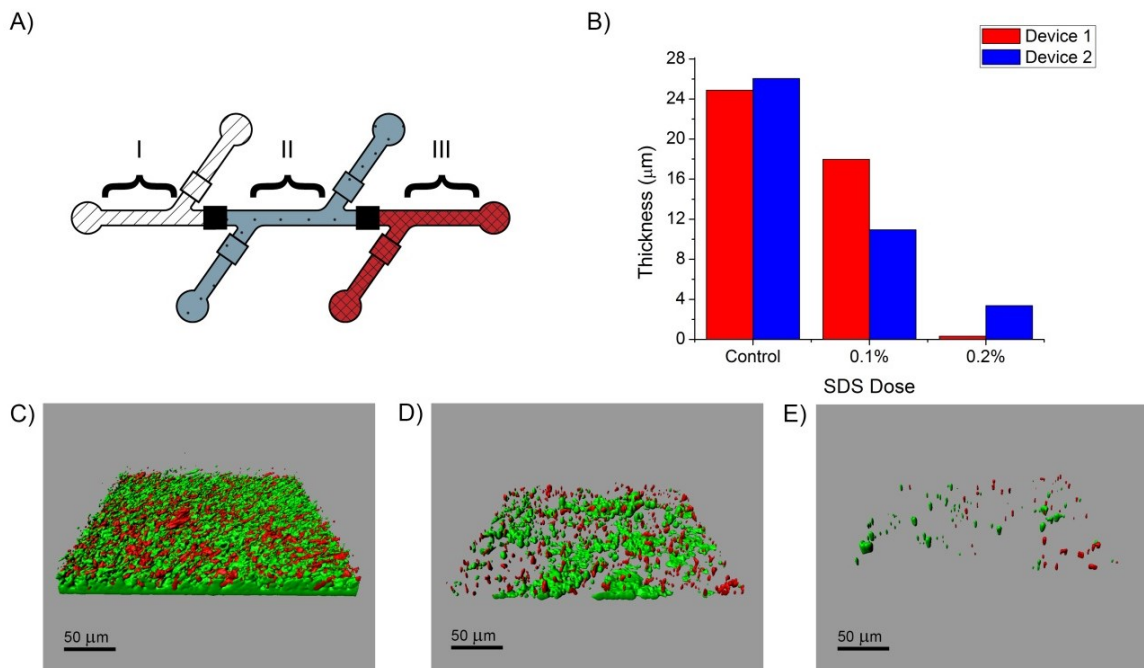


Figure 4.13. a) Schematic of device operation during biofilm segmentation, with the central channel trisected by two closed valves. Confocal microscopy images were obtained at the center of each of the three sections indicated (I, II, and III) b) Average biofilm thicknesses measured at the imaged locations in the two tested devices with different SDS exposure levels. c-e) Surface rendered confocal microscopy images of *E. coli* biofilms in Device 1 with c) no treatment (control) d) exposure to 0.1% SDS, and e) exposure to 0.2% SDS. Biofilm thicknesses were 24.9, 7.9, and 0.3 µm respectively.

The device presented here is suited for inverted confocal microscopy imaging, as the light path must only pass through the coverslip and the bottom-most PDMS layer before encountering the biofilm. While using confocal microscopy is a standard method for biofilm observation and quantification [170], more information about biofilms can be gathered in a continuous manner by integrating sensors into the microfluidic platform. As the biofilm grows on top of PDMS, integration of electrical or mechanical sensors

would require sensor fabrication within or on top of the PDMS [171, 172], or integration of pre-fabricated sensors into the PDMS [173, 174]. While possible, these processes may require extensive characterization so that the sensor integration fabrication processes do not preclude valve operation. The device is immediately compatible with off-chip, continuous optical detection methods such as optical density [118, 133] or on-chip fluorescence [175]. The integrated valves featured in this work allow the entire device to remain compact and to be integrated without opaque instrumentation impeding lightpaths.

Advancement of this methodology to include integrated biofilm optical density measurement for continuously evaluating the biofilm state, as developed and applied in Chapters 2 and 3, will provide additional information unattainable with end-point measurements from microscopy [118, 133]. For instance, any instantaneous changes in the biofilm structure can be measured as the valve orientations are switched for biofilm sectioning. Real-time biofilm sensitivity to antibiotics or other anti-biofilm treatments can also be measured, offering more detailed information about antibiotic tolerance kinetics than end-point microscopy can provide. Additionally, the development of biofilm non-uniformity or maintenance of uniformity throughout the channel can be monitored, providing a metric to compare to analytical bacterial biofilm growth models.

Expansion of the device design to include more biofilm sections than the three demonstrated in this work will also allow more experiments to be performed in the same platform. These experiments could range from the identification of appropriate staining procedures to the evaluation of biofilm sensitivity to antibiotics or shear stress. In addition to the variety of experiments that can be performed on a mature biofilm, there

are also a number of growth factors that can be altered to produce varied biofilm morphologies; these growth variables include growth media, flow conditions, bacterial strain, and the degree of maturity [32, 176, 177]. In extending the variety of biofilms grown in the platform, biofilm uniformity must be characterized for each introduction of a new growth variable in the system to ensure that each section of the biofilm is initially comparable to the others.

4.5 Chapter Summary

Microfluidics provide a convenient platform for targeting the challenge of bacterial biofilms, enabling scientific studies and drug testing in a small format easily integrated with many sensing modalities. The issue of biofilm variability between microfluidic devices was addressed by creating a platform where one biofilm was grown and sectioned into discrete segments that were subjected to different treatments in parallel or used as internal controls. Sectioning was achieved using hydraulically actuated valves integrated with a two-depth biofilm growth channel, enabled by ALD passivation of a photoresist mold to bypass incompatibilities between multiple photoresists. The platform was successfully used to segment biofilms and evaluate sensitivity to SDS. Through this work, the need for integrated controls observed in previous biofilm studies was confirmed, and the presented platform was proven to address this need. The novel ALD passivation technology developed to enable this work has an even broader impact beyond the biofilm research community, as photoresist passivation enables a host of microfluidic devices with varied cross-sectional geometries. This work introduces an additional degree of freedom in channel geometry into the microfluidic toolbox, thereby expanding

experimental design options as well as the broader base of scientific knowledge produced by microfluidic technologies.

5 Conclusion

5.1 Summary

A set of new microfluidic technologies were designed specifically to aid investigations of bacterial biofilms. Many types of bacterial biofilm growth platforms and evaluation methods exist and are widely employed at both the macroscale and microscale, and each presents a set of advantages and disadvantages for biofilm studies. The platforms created in this work were inspired by and combine the benefits of separate technologies to address challenges in the current technology. The non-invasive, continuous optical density measurements used in macroscale reactors with large sample volumes was integrated with the highly parallel studies and controllable microenvironments unique to microfluidic systems. The biofilm variability typically observed between microfluidic devices was addressed by using integrated valves to emulate techniques employed in larger reactors, where a single biofilm is partitioned into separate, comparable segments that can each be assayed as representatives of the original biofilm.

The first platform developed in this work addressed the requirements for continuous, non-invasive, and label-free evaluation of bacterial biofilms formed in microfluidics, as well as the need for efficient, multiplexed formation of biofilms assessed with traditional biofilm measurement techniques. This was accomplished by integrating optical density monitoring of biofilms with a microfluidic flow reactor for biofilm formation. Commercial, off-the-shelf photodiodes and LEDs served as optical detectors and light sources. These measurement components were aligned to a microfluidic channel, in which biofilms were grown and continuously measured by

monitoring the decrease in light transmitted through the growing biofilm. The optical response over biofilm growth was compared to results obtained using confocal microscopy. The correlation between optical density and biofilm thickness confirmed the validity of this measurement technique as applied to biofilms in microfluidics. As confocal microscopy typically interferes with the biofilm phenotype by requiring a fluorescent label, the use of optical density as a comparable measurement method provides a more accurate representation of the biofilm state.

The microfluidic platform for optical density measurement of biofilms was used in a scientific investigation of the dependence of bacterial biofilm growth on quorum sensing. First, biofilms formed by *Escherichia coli* with varying degrees of quorum sensing activity were evaluated. The method confirmed that a mutant strain of *E. coli* incapable of AI-2 synthesis formed thinner biofilms than wild type *E. coli*, and adding extracellular AI-2 to the mutant biofilm was able to partially restore thickness. Having proved the ability of the platform to distinguish between biofilms of different thicknesses formed in the microfluidic channel, the platform and measurement technique were applied toward assessing the potential for biofilm inhibition by AI-2 analogs. While a number of AI-2 analogs have been verified as quorum sensing inhibitors, their potential for inhibiting biofilm formation had not been previously investigated. The microscale biofilm reactor minimized the amount of analog required for experiments, allowing efficient use of the small samples generated in early research of new treatments. The results were the first demonstration that AI-2 analogs not only can inhibit bacterial biofilm formation, but when applied in conjunction with a traditional antibiotic, can virtually eliminate mature biofilms.

The second platform developed in this work was designed to provide improved experimental control by addressing variability observed between biofilms in different experiments. Hydraulically actuated PDMS valves were integrated with microfluidic channels to divide a biofilm into separate segments for further experimentation. In the development of this platform, a novel fabrication technique was developed for creating multi-depth microfluidic channels required for valve integration with biofilm growth channels. The incompatibilities between the different photoresists used to create the multiple depths were bypassed by using ALD to passivate layers with Al_2O_3 deposited at a low temperature compatible with the photoresist. The ability of the fabricated platforms to host uniform biofilms was confirmed, establishing the validity of using sections as representatives of the entire biofilm. Biofilms were partitioned with the integrated valves, and the resulting segments were used in experiments assessing bacterial biofilm sensitivity to SDS. The use of comparable segments of one biofilm contributed to the validity of the results, as observed differences could be attributed to SDS treatment as opposed to naturally occurring variation within one biofilm, between devices, or between devices tested on different days.

5.2 Future Work

The work presented in this dissertation reveals many avenues for further investigation. These research directions can be classified as either technology-driven, improving the functionality and applicability of the developed microfluidic platforms, or as application-driven, advancing the development of new anti-biofilm treatments.

In this work, biofilms formed within the valved device for biofilm segmentation were evaluated with confocal microscopy. A continuous biofilm measurement method – optical density monitoring – was developed for use with microfluidic platforms, and an immediate technological advancement of the valved device would be its integration with CCD-based optical density measurement. Detailed spatiotemporal information obtained during biofilm formation in the valved device would not only reveal dynamics of applied treatments, but could also be used to further investigate and characterize biofilm uniformity in the microfluidic channel.

The device for biofilm segmentation developed here was designed to divide biofilms into three sections. The throughput of biofilm studies could be expanded if the channel could be divided into more sections. However, before redesigning the geometry of the device presented in this work, additional characterization is required to evaluate the interactions between the biofilm and channel geometry. In this work, biofilms were deemed uniform based on measurements obtained in the center of each section, 4 mm away from either a valve or a fluidic inlet or outlet. It is likely that the morphology of the biofilm changes with the altered flow closer to channel features such as valves or fluidic inlets and outlets, and may be different from the biofilm in the center of the section. Future work with this device should determine the limit on how close together valves can be positioned while allowing development of a uniform biofilm unaffected by perturbations in flow. Integration of CCDs for continuous optical density measurement could provide this data and inform the rearrangement of valves and channels for increasing the number of sections to increase the throughput of biofilm experiments.

When characterizing new antibacterial treatments, it is common to evaluate the minimum drug concentration necessary to completely eliminate the bacterial population. In order to streamline biofilm research using system automation, a diffusive gradient mixer can be added upstream of the existing platform, analogous to the device developed by Kim et al. [111]. The configuration use valves to prevent flow through the side channels and through the gradient mixer during growth. For experimentation, one set of valves would close in order to divide the biofilm growth channel into sections, while another set would open to allow flow through the side channels and the gradient mixer. This configuration would deliver different concentrations of the same drug to different sections of the biofilm, as depicted in Figure 5.1.

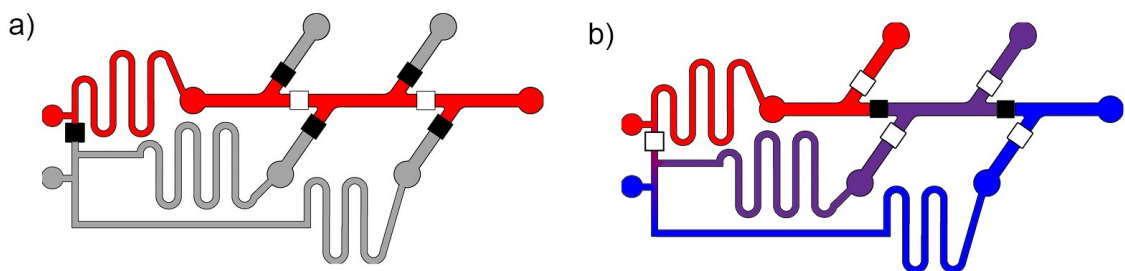


Figure 5.1. Schematics of valved device for biofilm segmentation integrated with a diffusive gradient mixer for generating multiple concentrations of a solution, e.g. antibiotic or AI-2 analog, on-chip. a) Device configuration during biofilm growth, with side channels and gradient mixer blocked by closed valves (solid black squares) b) Device operation during biofilm sectioning and exposure of biofilm sections to different concentrations of drugs, with side channels open and central channel trisected by two closed valves.

The integration of concentration gradients generated on-chip could be used to evaluate the minimum antibiotic concentration needed to induce synergistic biofilm inhibition with an AI-2 analog. Conversely, a complex mixer with three inlets, for growth media, antibiotic, and AI-2 analog could be constructed in order to vary the antibiotic and AI-2 analog concentrations simultaneously and determine the combination most effective for biofilm inhibition.

As previously mentioned, the technologies developed here can be employed as pharmaceutical testbeds. The types of biofilms grown in the device can be expanded from monocultures to co-cultures of multiple species, more similar to the diverse ecosystems found in biofilm infections. Co-cultures would be particularly useful in testing the AI-2 analogs used in this work, as the analogs can be tailored to inhibit quorum sensing in several species at once, or to target one type of bacteria within a co-culture [84]. This concept could be expanded to modeling infections formed on tissue by forming a biofilm on a monolayer of epithelial cells, similar to the work of Kim et al. [124]. Such an infection model could be used first to characterize how biofilms interact with the epithelial cells, then expanded to evaluate possible changes in the biofilm response to treatment in the presence of the simulated tissue. Additionally, while treatments may be effective at eradicating biofilms, they may produce toxicity in the host. Use of an on-chip infection model would aid in evaluating potential side effects. While replication of *in vivo* conditions in a microfluidic device is unlikely, preliminary studies performed in a microfluidic device can serve as a guide for designing studies in animal models of infection.

5.3 Conclusion

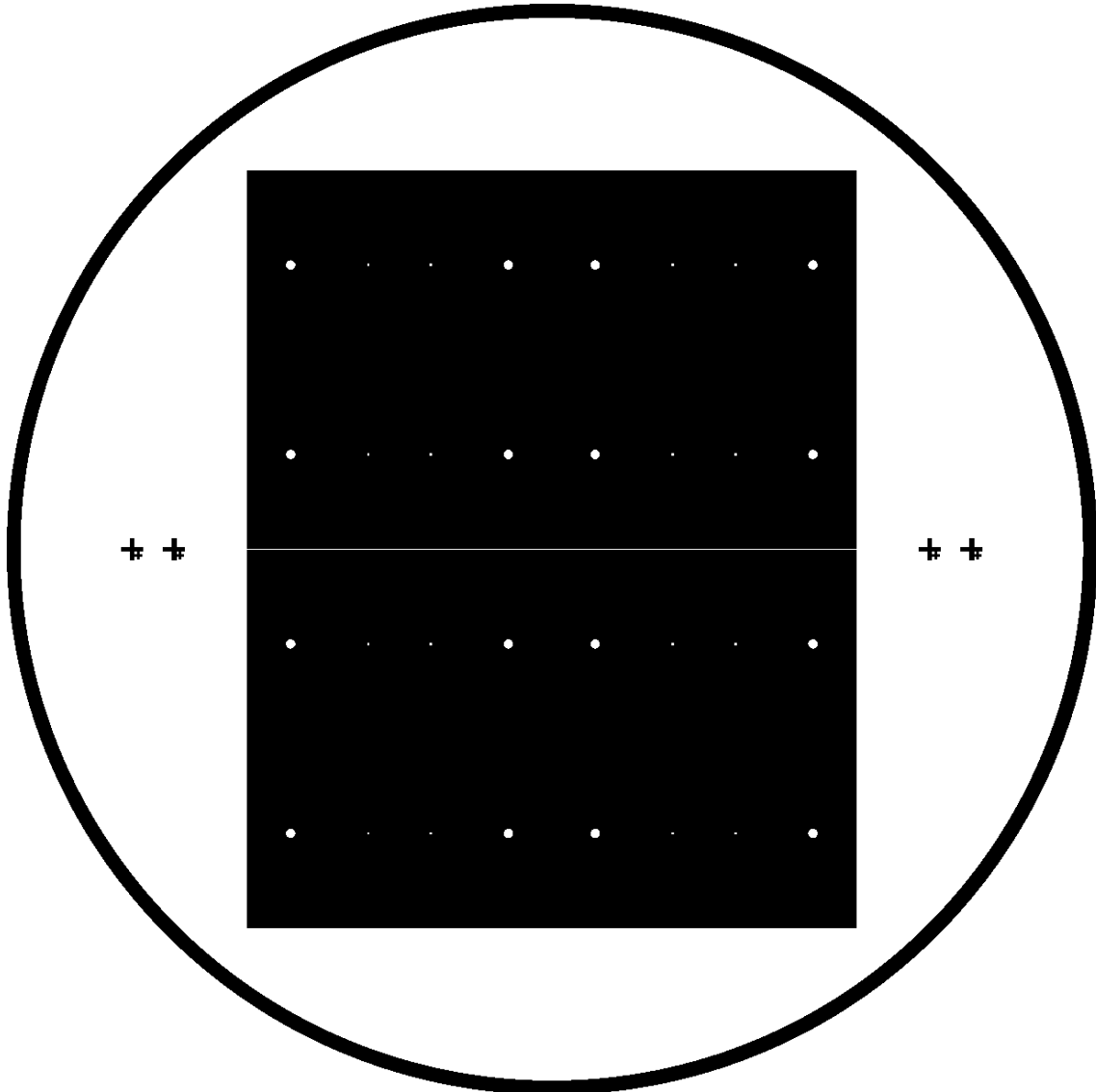
The global health challenge presented by the tenacity of bacterial biofilm infections has created a need for efficient *in vitro* tools and methods for accurately evaluating biofilms and their response to new treatments. This need was addressed in this dissertation through the development of microfluidic platforms for in-line evaluation of biofilm state as well as for controlled, high-throughput performance of assays on biofilms. The results generated show the promise of using microfluidics for biofilm

studies, especially as applied to drug development. These microfluidic platforms will serve as a foundation for developing *in vitro* biofilm models that may be used in the development and evaluation of drugs targeting persistent biofilm infections.

Appendix A: Masks Used

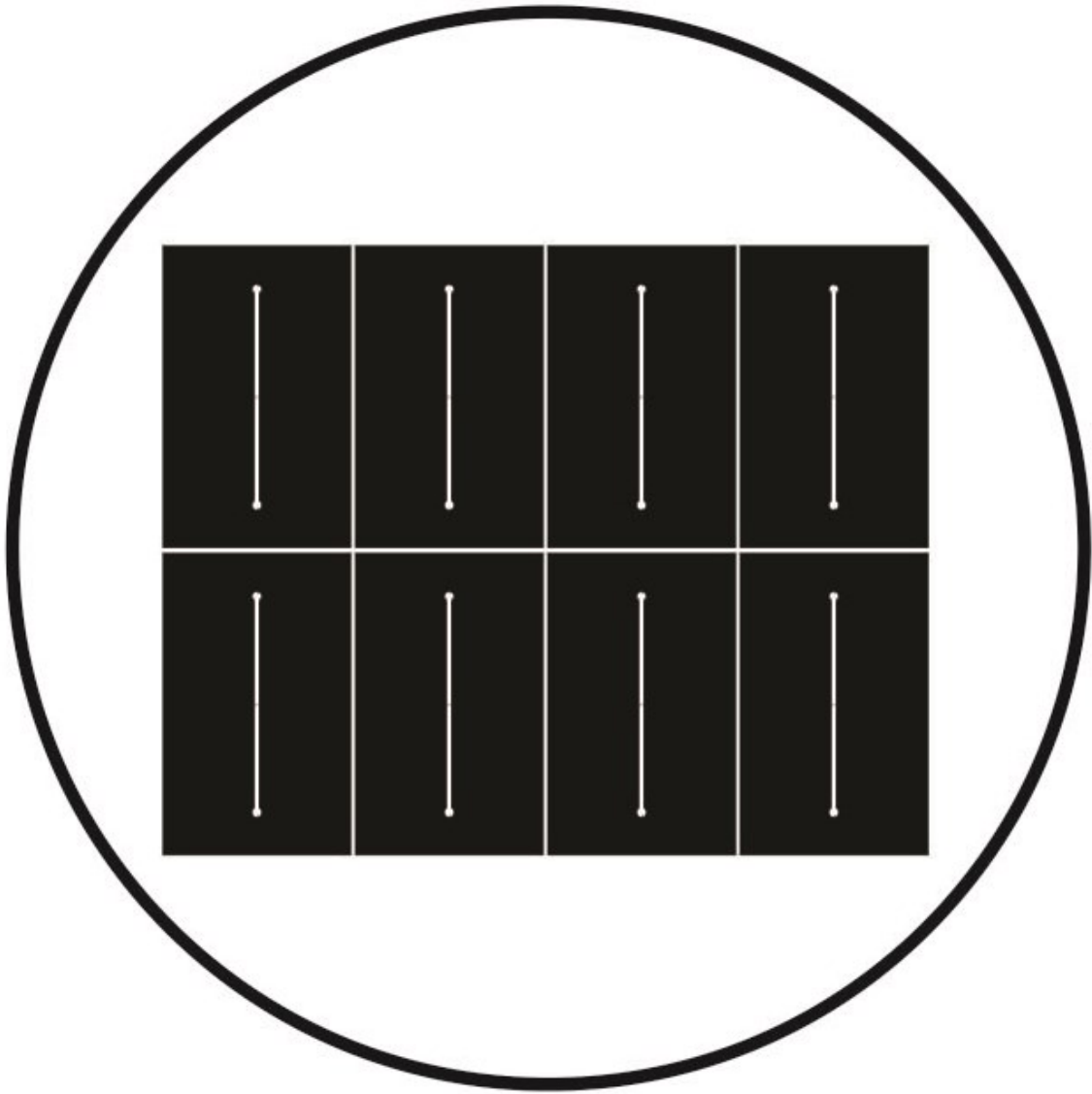
Mask #1

Observation window patterning in chrome for microfluidic biofilm optical density measurement platform



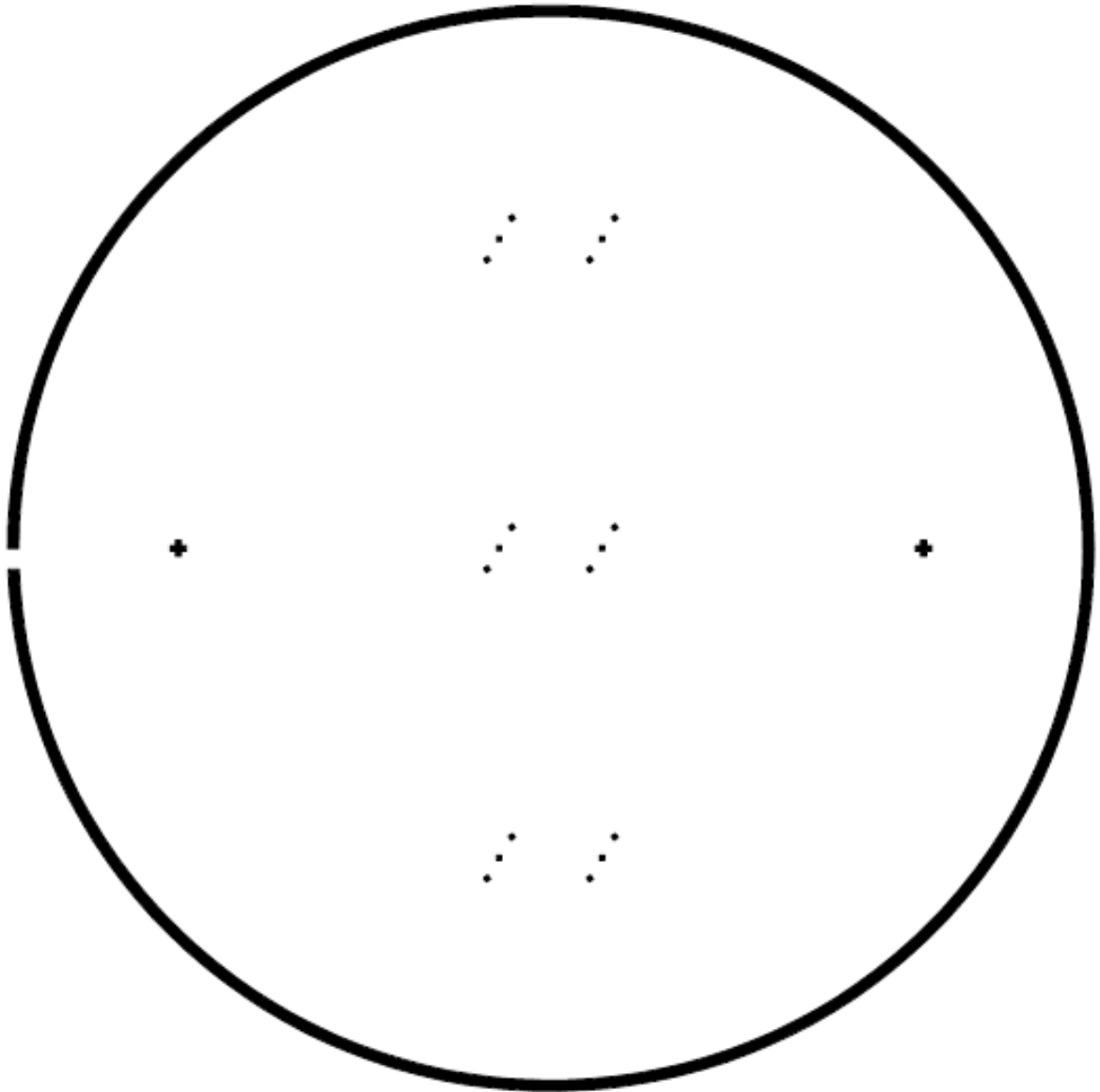
Mask #2

Mold for single microfluidic channel used in biofilm optical density measurement platform



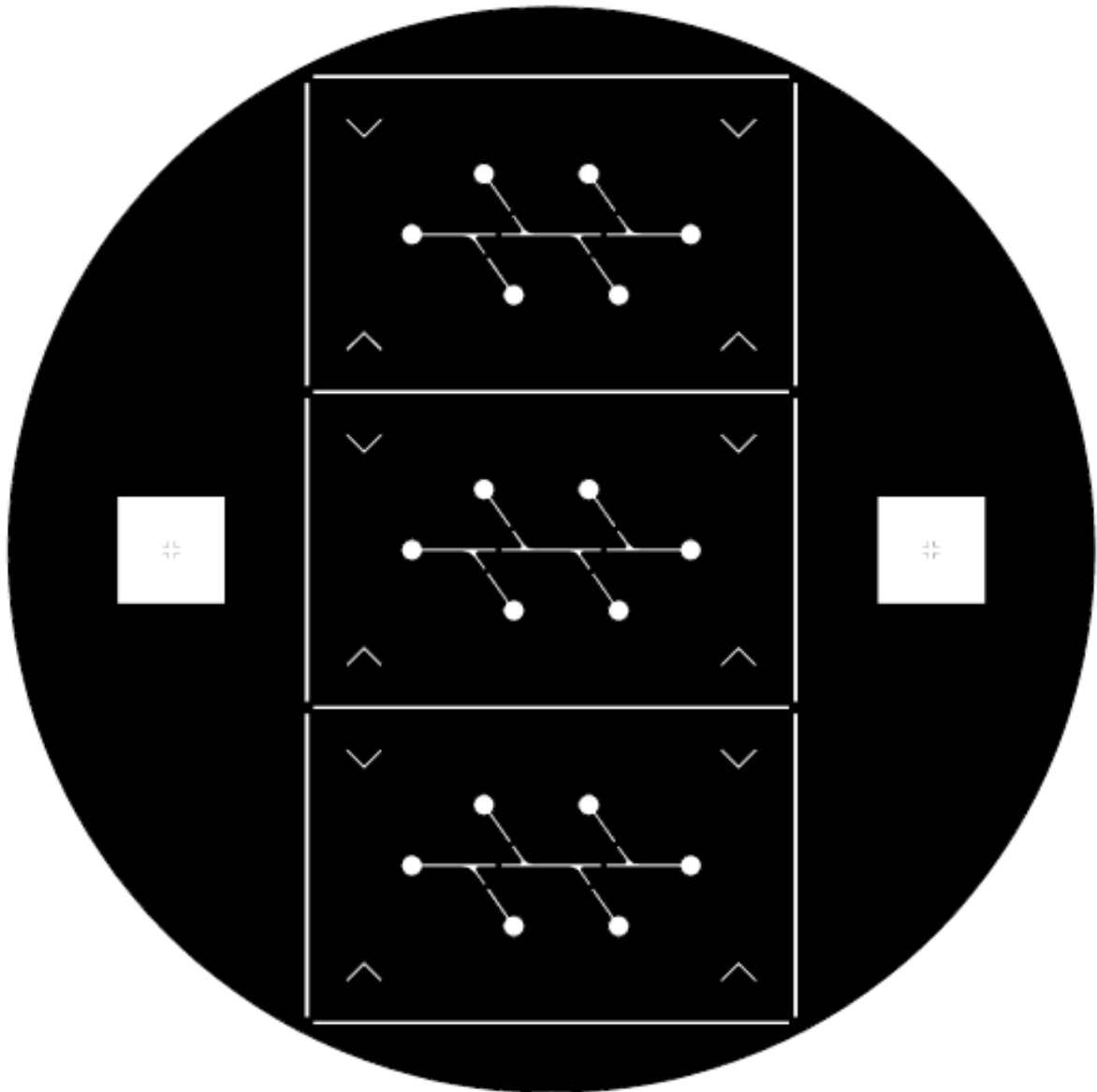
Mask #3

Pattern to form mold for valve areas of fluidic channel in the multi-depth microfluidic platform for biofilm formation and sectioning



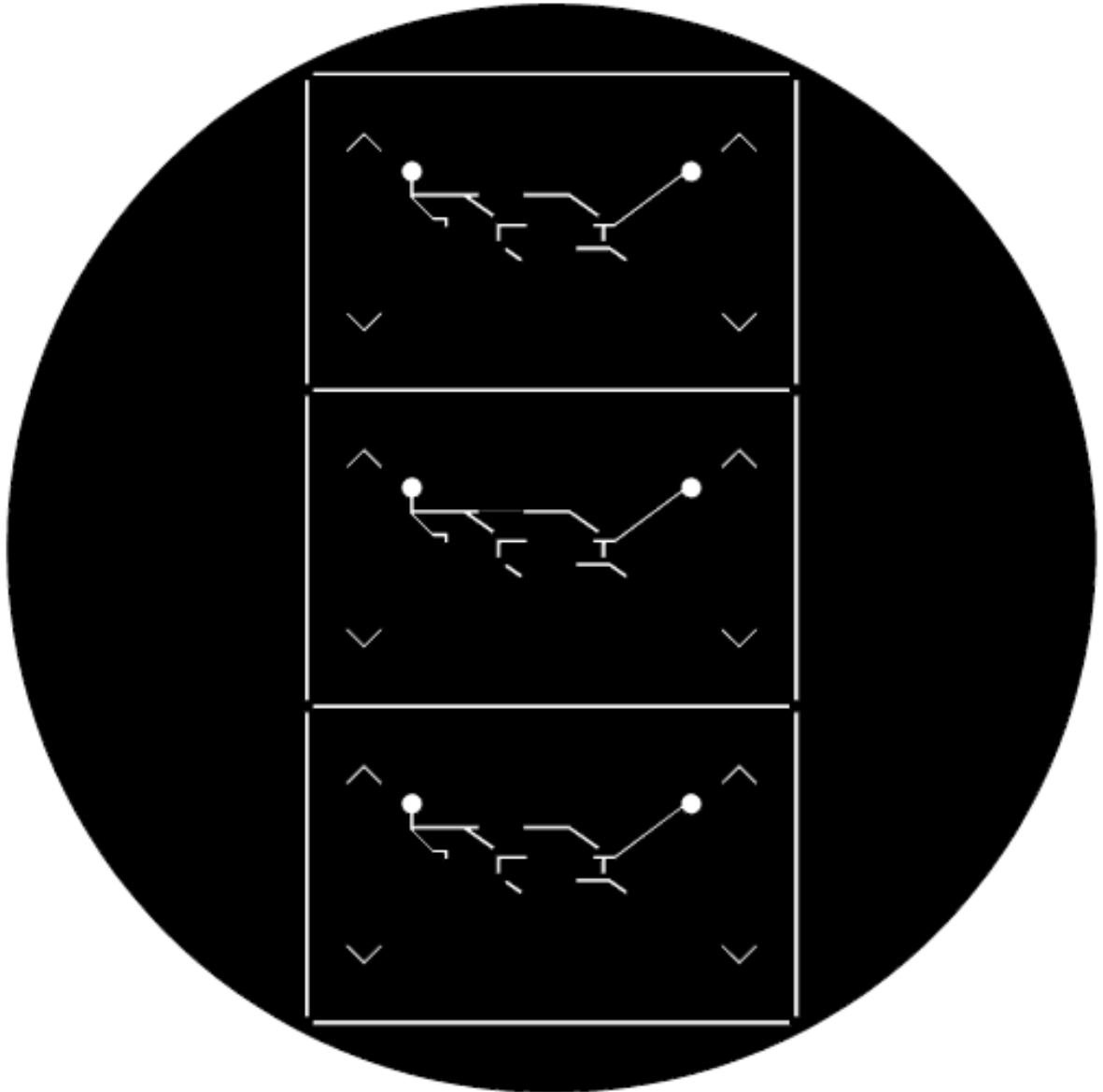
Mask #4

Pattern to form mold for deep areas in fluidic channel in the multi-depth microfluidic platform for biofilm formation and sectioning



Mask #5

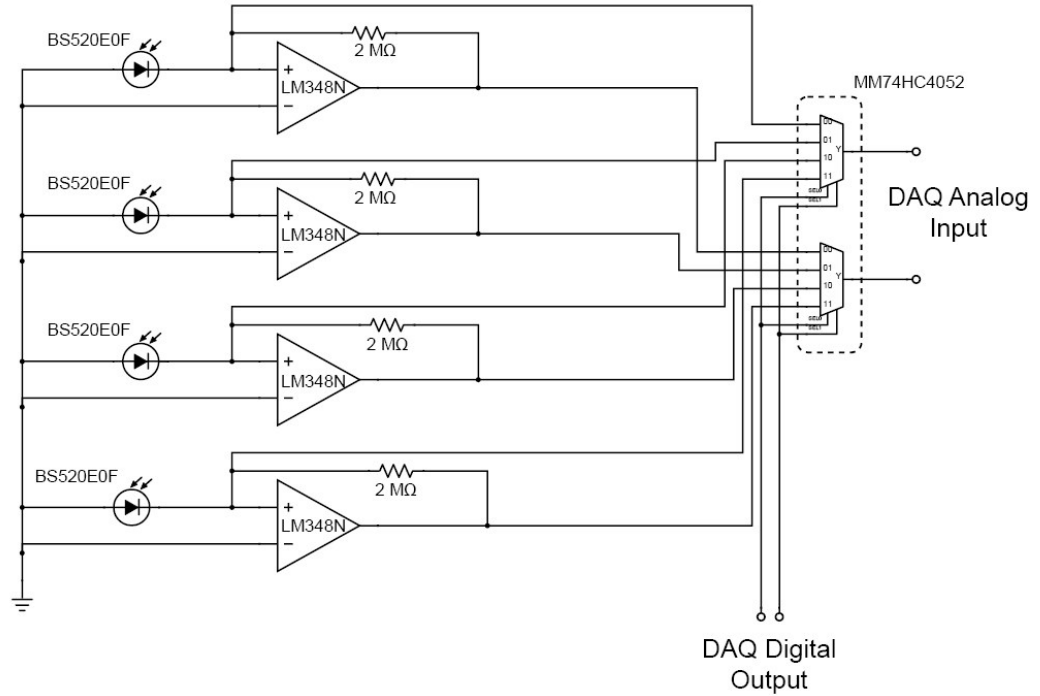
Pattern for control channel mold used to actuate valves in the multi-depth microfluidic platform for biofilm formation and sectioning



Appendix B: Circuit Diagrams

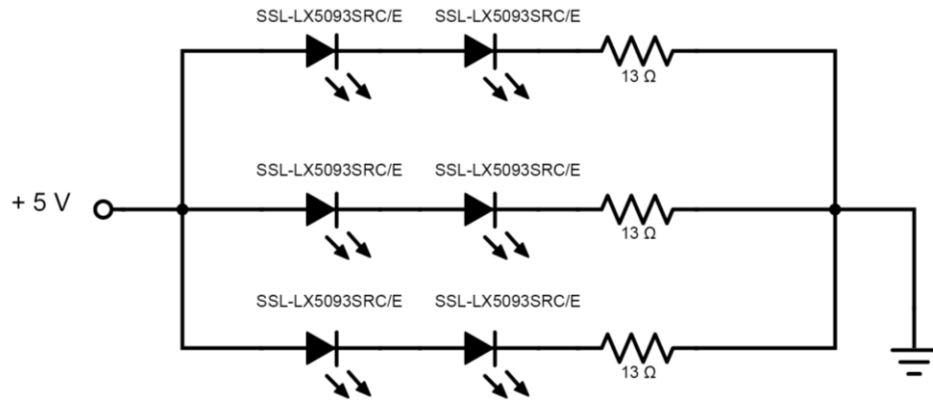
Photodiode Measurement

The circuit diagram for measuring the outputs of four photodiodes (corresponding to two microfluidic channels with two measurement windows each) using two analog input ports on the USB-6221 DAQ card is shown below.



LED Circuit

The circuit diagram for measuring the outputs of four photodiodes (corresponding to two microfluidic channels with two measurement windows each) using two analog input ports on the USB-6221 DAQ card is shown below. Not shown is the 8 V DC power supply connected to the 5 V voltage regulator (BA17085) providing the source voltage for the LED circuit.



Appendix C: Matlab Code

Basic OD Measurement

This program reads a series of files output by LabVIEW, each of which contains readings from photodiodes and from the multiplexer, along with a time stamp and the digital counter value (determining the multiplexer state). The program separates the multiplexer signal into signals from individual photodiodes, and converts these values into changes in optical density.

```
clc
clear all

R_1=(0.938+0.96)*10^6; %ohms
R_2=2*0.96e6; %ohms
R_3=2*0.938e6; %ohms
R_4=2*0.96e6; %ohms
R_5=2*0.96e6; %ohms
R_6=2*0.96e6; %ohms

%read in CSV file
filename = input('Enter the filename of the baseline file: ',
's');
baseline = csvread(filename);

time_s=baseline(:,1);
time_hr=time_s./3600;

% Sort
V_combined=baseline(:,2);
indicator = baseline(:,16);
L=length(V_combined);
j1=1;
j2=1;
j3=1;
j4=1;

for i=1:L
    if indicator(i)==0
        V1(j1)=V_combined(i);
        t1(j1)=time_s(i);
        j1=j1+1;
    elseif indicator(i)==1
        V2(j2)=V_combined(i);
        t2(j2)=time_s(i);
        j2=j2+1;
    elseif indicator(i)==2
```

```

        V3(j3)=V_combined(i);
        t3(j3)=time_s(i);
        j3=j3+1;
    elseif indicator(i)==3
        V4(j4)=V_combined(i);
        t4(j4)=time_s(i);
        j4=j4+1;
    end
end

V5=baseline(:,3);
V6=baseline(:,4);
V7=baseline(:,5);
V8=baseline(:,6);

%Take voltage from data and convert to current, then to
illuminance (I)
%Illuminance conversion approximated from photodiode datasheet,
BS520E0F

I1=(V1./(R_1*(5.5e-9))).^(1/0.869176);
I2=(V2./(R_2*(5.5e-9))).^(1/0.869176);
I3=(V3./(R_3*(5.5e-9))).^(1/0.869176);
I4=(V4./(R_4*(5.5e-9))).^(1/0.869176);
I5=(V5./(R_5*(5.5e-9))).^(1/0.869176);
I6=(V6./(R_6*(5.5e-9))).^(1/0.869176);
I7=(V7./(R_6*(5.5e-9))).^(1/0.869176);
I8=(V8./(R_6*(5.5e-9))).^(1/0.869176);

%Obtain illuminance values for baseline
I0_1=mean(I1(1:2000));
I0_2=mean(I2(1:2000));
I0_3=mean(I3(1:2000));
I0_4=mean(I4(1:2000));
I0_5=mean(I5(1:2000));
I0_6=mean(I6(1:2000));
I0_7=mean(I7(1:2000));
I0_8=mean(I8(1:2000));

%Calculate change in OD
abs_1=-log10(I1/I0_1);
abs_2=-log10(I2/I0_2);
abs_3=-log10(I3/I0_3);
abs_4=-log10(I4/I0_4);
abs_5=-log10(I5/I0_5);
abs_6=-log10(I6/I0_6);
abs_7=-log10(I7/I0_7);
abs_8=-log10(I8/I0_8);

% Filter the data
a=1;
b=ones(1,1000);
b=b.*(1/1000);
abs_1=filter(b,a,abs_1);
abs_2=filter(b,a,abs_2);
abs_3=filter(b,a,abs_3);

```

```
abs_4=filter(b,a,abs_4);  
abs_5=filter(b,a,abs_5);  
abs_6=filter(b,a,abs_6);  
abs_7=filter(b,a,abs_7);  
abs_8=filter(b,a,abs_8);
```

```
% Average the OD values obtained by photodiode pairs. These  
values can be plotted, or output to another program for further data  
processing.
```

```
abs_12=(abs_1+abs_2)./2;  
abs_34=(abs_3+abs_4)./2;  
abs_56=(abs_5+abs_6)./2;  
abs_78=(abs_7+abs_8)./2;
```

Data Fitting

This program smooths data in order to eliminate transient fluctuations in photodiode signals. This is accomplished by dividing the data into sections, each of which is fitted to a quadratic function. The program below has been shortened for fitting one data set (whereas it was used mostly for simultaneously smoothing multiple data sets, i.e. for channels operated in parallel).

```
clc
clear all

load data

x_w=time_wt; % Time
y_w=abs_wt; % Optical density

length = length(x_w);

% Use least-squares fit technique
% Split up the data into overlapping chunks; each chunk will be
1000 units long, overlap by 500. Values in the overlap will be
averaged

i=0; % This is a counter for keeping track of the overlaps
j=0;
increment=1000;
y_est_w=[0];
x_est_w=[0];

for j=1:increment/2:length-increment+1
    j;
    i=i+1;
    % Get a chunk of data
    y1=y_w(j:j+increment);
    x1=x_w(j:j+increment);

    % Get the fit for the chunk
    pcoeff_1=polyfit(x1, y1, 2);
    x_est_1=x2;
    y_est_1=polyval(pcoeff_1,x_est_1);

    % IF i>1, take the first (increment/2) values and average
    them with the last (increment/2) values in the main compilation vector.
    % Then, set the first (increment/2) values of the current
    chunk to this average. Later, this chunk will be added not at the end
    of the main compilation vector, but (increment/2) values before the
    start point of the chunk (j-increment/2).
```



```

        if i>1
            lc=size(y_est_w);
            lc=lc(1);
            lc_start=lc-increment/2+1;

y1_avg=0.5.*((y_est_1(1:increment/2))+y_est_w(lc_start:lc));
            y_est_1(1:increment/2)=y1_avg;

            y_est_w=[y_est_w(1:lc_start);y_est_1];
            x_est_w=[x_est_w(1:lc_start);x_est_1];

        else
            y_est_w=[y_est_w;y_est_1];
            x_est_w=[x_est_w;x_est_1];
        end

        % Now put the fit increment/2 from the end of the main
        compilation vector. Do this by letting compilation vector be
        y_est_w(1:lc_start), then tack on y_est_1 etc.

    end

    a=1;
    b=ones(1,400);
    b=b.*(1/400);

    y_est_w=filter(b,a,y_est_w);

```

6 References

- [1] C. Potera, "Microbiology - Forging a link between biofilms and disease," *Science*, vol. 283, pp. 1837-1839, Mar 1999.
- [2] C. A. Fux, P. Stoodley, M. Shirtliff, and J. W. Costerton, "The Functional Resistance of Bacterial Biofilms," in *Antimicrobial Drug Resistance*, D. L. Mayers, Ed., ed: Humana Press, 2009, pp. 121-131.
- [3] C. Bordi and S. de Bentzmann, "Hacking into bacterial biofilms: a new therapeutic challenge," *Annals of intensive care*, vol. 1, p. 19, Jun 2011.
- [4] J. J. Richards and C. Melander, "Controlling Bacterial Biofilms," *Chembiochem*, vol. 10, pp. 2287-2294, Sep 2009.
- [5] D. Davies, "Understanding biofilm resistance to antibacterial agents," *Nature Reviews Drug Discovery*, vol. 2, pp. 114-122, Feb 2003.
- [6] N. Hoiby, O. Ciofu, H. K. Johansen, Z. J. Song, C. Moser, P. O. Jensen, S. Molin, M. Givskov, T. Tolker-Nielsen, and T. Bjarnsholt, "The clinical impact of bacterial biofilms," *International Journal of Oral Science*, vol. 3, pp. 55-65, Apr 2011.
- [7] R. M. Donlan, "Biofilms: microbial life on surfaces," *Emerging infectious diseases*, vol. 8, pp. 881-90, 2002.
- [8] H. Ceri, M. E. Olson, C. Stremick, R. R. Read, D. Morck, and A. Buret, "The Calgary Biofilm Device: New technology for rapid determination of antibiotic susceptibilities of bacterial biofilms," *Journal of Clinical Microbiology*, vol. 37, pp. 1771-1776, Jun 1999.
- [9] S. A. Crusz, R. Popat, M. T. Rytke, M. Camara, M. Givskov, T. Tolker-Nielsen, S. P. Diggle, and P. Williams, "Bursting the bubble on bacterial biofilms: a flow cell methodology," *Biofouling*, vol. 28, pp. 835-842, 2012.
- [10] B. F. Gilmore, T. M. Hamill, D. S. Jones, and S. P. Gorman, "Validation of the CDC Biofilm Reactor as a Dynamic Model for Assessment of Encrustation Formation on Urological Device Materials," *Journal of Biomedical Materials Research Part B-Applied Biomaterials*, vol. 93B, pp. 128-140, Apr 2010.
- [11] A. Kharazmi, B. Giwercman, and N. Hoiby, "Robbins device in biofilm research," *Biofilms*, vol. 310, pp. 207-215, 1999.
- [12] A. Heydorn, B. K. Ersbøll, M. Hentzer, M. R. Parsek, M. Givskov, and S. Molin, "Experimental reproducibility in flow-chamber biofilms," *Microbiology*, vol. 146, pp. 2409-2415, October 1 2000.

- [13] G. Roeselers, B. Zippel, M. Staal, M. van Loosdrecht, and G. Muyzer, "On the reproducibility of microcosm experiments - different community composition in parallel phototrophic biofilm microcosms," *Fems Microbiology Ecology*, vol. 58, pp. 169-178, Nov 2006.
- [14] R. Bakke, R. Kommedal, and S. Kalvenes, "Quantification of biofilm accumulation by an optical approach," *Journal Of Microbiological Methods*, vol. 44, pp. 13-26, Feb 1 2001.
- [15] A. F. Gonzalez Barrios, R. Zuo, Y. Hashimoto, L. Yang, W. E. Bentley, and T. K. Wood, "Autoinducer 2 controls biofilm formation in *Escherichia coli* through a novel motility quorum-sensing regulator (MqsR, B3022)," *Journal of Bacteriology*, vol. 188, pp. 305-316, Jan 2006.
- [16] J. Li, C. Attila, L. Wang, T. K. Wood, J. J. Valdes, and W. E. Bentley, "Quorum sensing in *Escherichia coli* is signaled by AI-2/LsrR: effects on small RNA and biofilm architecture," *Journal of Bacteriology*, vol. 189, pp. 6011-6020, Aug 2007.
- [17] M. Herzberg, I. K. Kaye, W. Peti, and T. K. Wood, "YdgG (TqsA) controls biofilm formation in *Escherichia coli* K-12 through autoinducer 2 transport," *Journal of Bacteriology*, vol. 188, pp. 587-98, Jan 2006.
- [18] G. O'Toole, H. B. Kaplan, and R. Kolter, "Biofilm formation as microbial development " *Annual Reviews in Microbiology*, vol. 54, pp. 49-79, 2000.
- [19] L. A. Pratt and R. Kolter, "Genetic analysis of *Escherichia coli* biofilm formation: roles of flagella, motility, chemotaxis and type I pili," *Molecular Microbiology*, vol. 30, pp. 285-293, Oct 1998.
- [20] R. Dewanti and A. C. L. Wong, "Influence of culture conditions on biofilm formation by *Escherichia coli* O157:H7," *International Journal of Food Microbiology*, vol. 26, pp. 147-164, 1995.
- [21] M. E. Davey and G. A. O'toole, "Microbial Biofilms: from Ecology to Molecular Genetics," *Microbiology and Molecular Biology Reviews*, vol. 64, pp. 847-867, Dec 1 2000.
- [22] G. A. O'Toole and R. Kolter, "Flagellar and twitching motility are necessary for *Pseudomonas aeruginosa* biofilm development," *Molecular Microbiology*, vol. 30, pp. 295-304, 1998.
- [23] A. Ohashi and H. Harada, "Adhesion strength of biofilm developed in an attached-growth reactor," *Water Science and Technology*, vol. 29, pp. 281-288, 1994.

- [24] H.-C. Flemming and J. Wingender, "The biofilm matrix," *Nature Reviews Microbiology*, vol. 8, pp. 623-633, 2010.
- [25] C. Beloin, A. Roux, and J. M. Ghigo, "Escherichia coli biofilms," in *Bacterial Biofilms*. vol. 322, ed, 2008, pp. 249-289.
- [26] M. J. Schurr, "Which Bacterial Biofilm Exopolysaccharide Is Preferred, Psl or Alginate?," *Journal of Bacteriology*, vol. 195, pp. 1623-1626, April 15 2013.
- [27] P. S. Stewart and M. J. Franklin, "Physiological heterogeneity in biofilms," *Nature Reviews Microbiology*, vol. 6, pp. 199-210, 2008.
- [28] C. Beloin and J.-M. Ghigo, "Finding gene-expression patterns in bacterial biofilms," *Trends in Microbiology*, vol. 13, pp. 16-19, 2005.
- [29] D. Ren, L. A. Bedzyk, S. M. Thomas, R. W. Ye, and T. K. Wood, "Gene expression in Escherichia coli biofilms," *Applied Microbiology and Biotechnology*, vol. 64, pp. 515-524, May 2004.
- [30] C. Beloin, J. Valle, P. Latour-Lambert, P. Faure, M. Kzreminski, D. Balestrino, J. A. J. Haagensen, S. Molin, G. Prensier, B. Arbeille, and J.-M. Ghigo, "Global impact of mature biofilm lifestyle on Escherichia coli K-12 gene expression," *Molecular Microbiology*, vol. 51, pp. 659-674, 2004.
- [31] M. A. Schembri, K. Kjærsgaard, and P. Klemm, "Global gene expression in Escherichia coli biofilms," *Molecular Microbiology*, vol. 48, pp. 253-267, 2003.
- [32] V. Janakiraman, D. Englert, A. Jayaraman, and H. Baskaran, "Modeling Growth and Quorum Sensing in Biofilms Grown in Microfluidic Chambers," *Annals of Biomedical Engineering*, vol. 37, pp. 1206-1216, Jun 2009.
- [33] W. G. Characklis, "Bioengineering report: Fouling biofilm development: A process analysis," *Biotechnology and Bioengineering*, vol. 23, pp. 1923-1960, 1981.
- [34] M. G. Fagerlind, J. S. Webb, N. Barraud, D. McDougald, A. Jansson, P. Nilsson, M. Harlén, S. Kjelleberg, and S. A. Rice, "Dynamic modelling of cell death during biofilm development," *Journal of Theoretical Biology*, vol. 295, pp. 23-36, 2012.
- [35] H. Shao, R. J. Lamont, and D. R. Demuth, "Autoinducer 2 is required for Biofilm growth of *Aggregatibacter* (*Actinobacillus*) *actinomycetemcomitans*," *Infection And Immunity*, vol. 75, pp. 4211-4218, Sep 2007.
- [36] A. Rochex, J.-J. Godon, N. Bernet, and R. Escudie, "Role of shear stress on composition, diversity and dynamics of biofilm bacterial communities," *Water Research*, vol. 42, pp. 4915-4922, Dec 2008.

- [37] M. J. Chen, Z. Zhang, and T. R. Bott, "Direct measurement of the adhesive strength of biofilms in pipes by micromanipulation," *Biotechnology Techniques*, vol. 12, pp. 875-880, Dec 1998.
- [38] T. F. C. Mah and G. A. O'Toole, "Mechanisms of biofilm resistance to antimicrobial agents," *Trends in Microbiology*, vol. 9, pp. 34-39, Jan 2001.
- [39] H. Kumon, K. Tomochika, T. Matunaga, M. Ogawa, and H. Ohmori, "A sandwich cup method for the penetration assay of antimicrobial agents through *Pseudomonas* exopolysaccharides," *Microbiology and Immunology*, vol. 38, pp. 615-619, 1994.
- [40] S. Bose and A. K. Ghosh, "Biofilms: A Challenge To Medical Science," *Journal of Clinical and Diagnostic Research*, vol. 5, pp. 127-130, July 2012.
- [41] M. C. Walters, F. Roe, A. Bugnicourt, M. J. Franklin, and P. S. Stewart, "Contributions of antibiotic penetration, oxygen limitation, and low metabolic activity to tolerance of *Pseudomonas aeruginosa* biofilms to ciprofloxacin and tobramycin," *Antimicrobial Agents and Chemotherapy*, vol. 47, pp. 317-323, Jan 2003.
- [42] C. Chan, L. L. Burrows, and C. M. Deber, "Alginate as an auxiliary bacterial membrane: binding of membrane-active peptides by polysaccharides*," *The Journal of Peptide Research*, vol. 65, pp. 343-351, 2005.
- [43] J. N. Anderl, M. J. Franklin, and P. S. Stewart, "Role of antibiotic penetration limitation in *Klebsiella pneumoniae* biofilm resistance to ampicillin and ciprofloxacin," *Antimicrobial Agents and Chemotherapy*, vol. 44, pp. 1818-1824, 2000.
- [44] G. G. Anderson and G. A. O'Toole, "Innate and induced resistance mechanisms of bacterial biofilms," *Current Topics in Microbiology and Immunology*, vol. 322, pp. 85-105, 2008.
- [45] G. Stone, P. Wood, L. Dixon, M. Keyhan, and A. Matin, "Tetracycline Rapidly Reaches All the Constituent Cells of Uropathogenic *Escherichia coli* Biofilms," *Antimicrobial Agents and Chemotherapy*, vol. 46, pp. 2458-2461, Aug 1 2002.
- [46] T. C. Zhang and P. L. Bishop, "Evaluation of substrate and pH effects in a nitrifying biofilm," *Water Environment Research*, vol. 68, pp. 1107-1115, 1996.
- [47] W. M. Dunne, "Bacterial Adhesion: Seen Any Good Biofilms Lately?," *Clinical Microbiology Reviews*, vol. 15, pp. 155-166, April 1 2002.

- [48] P. S. Stewart and J. W. Costerton, "Antibiotic resistance of bacteria in biofilms," *Lancet*, vol. 358, pp. 135-138, Jul 14 2001.
- [49] S. Molin and T. Tolker-Nielsen, "Gene transfer occurs with enhanced efficiency in biofilms and induces enhanced stabilisation of the biofilm structure," *Current Opinion in Biotechnology*, vol. 14, pp. 255-261, 2003.
- [50] M. Hausner and S. Wuertz, "High Rates of Conjugation in Bacterial Biofilms as Determined by Quantitative In Situ Analysis," *Applied and Environmental Microbiology*, vol. 65, pp. 3710-3713, Aug 1999.
- [51] S. Wuertz, S. Okabe, and M. Hausner, "Microbial communities and their interactions in biofilm systems: an overview," *Water Science & Technology*, vol. 49, pp. 327-336, 2004.
- [52] J.-M. Ghigo, "Natural conjugative plasmids induce bacterial biofilm development," *Nature*, vol. 412, pp. 442-445, 2001.
- [53] I. Keren, N. Kaldalu, A. Spoering, Y. Wang, and K. Lewis, "Persister cells and tolerance to antimicrobials," *FEMS Microbiology Letters*, vol. 230, pp. 13-18, Jan 15 2004.
- [54] K. Lewis, "Persister cells," *Annual Review of Microbiology*, vol. 64, pp. 357-372, 2010.
- [55] J. Nesper, C. M. Lauriano, K. E. Klose, D. Kapfhammer, A. Kraiss, and J. Reidl, "Characterization of *Vibrio cholerae* O1 El Tor galU and galE mutants: Influence on lipopolysaccharide structure, colonization, and biofilm formation," *Infection and Immunity*, vol. 69, pp. 435-445, Jan 2001.
- [56] D. G. Davies, M. R. Parsek, J. P. Pearson, B. H. Iglewski, J. W. Costerton, and E. P. Greenberg, "The involvement of cell-to-cell signals in the development of a bacterial biofilm," *Science*, vol. 280, pp. 295-298, Apr 10 1998.
- [57] G. A. O'Toole, L. A. Pratt, P. I. Watnick, D. K. Newman, V. B. Weaver, and R. Kolter, "Genetic approaches to study of biofilms," in *Methods in Enzymology*. vol. 310, J. D. Ron, Ed., ed: Academic Press, 1999, pp. 91-109.
- [58] A. Vendeville, K. Winzer, K. Heurlier, C. M. Tang, and K. R. Hardie, "Making 'sense' of metabolism: Autoinducer-2, LuxS and pathogenic bacteria," *Nature Reviews Microbiology*, vol. 3, pp. 383-396, May 2005.
- [59] V. Roy, B. L. Adams, and W. E. Bentley, "Developing next generation antimicrobials by intercepting AI-2 mediated quorum sensing," *Enzyme Microb Technol*, vol. 49, pp. 113-23, Jul 10 2011.

- [60] J. Sun, R. Daniel, I. Wagner-Dobler, and A. P. Zeng, "Is autoinducer-2 a universal signal for interspecies communication: a comparative genomic and phylogenetic analysis of the synthesis and signal transduction pathways," *BMC Evolutionary Biology*, vol. 4, p. 36, Sep 29 2004.
- [61] S. Hooshangi and W. E. Bentley, "From unicellular properties to multicellular behavior: bacteria quorum sensing circuitry and applications," *Current Opinion in Biotechnology*, vol. 19, pp. 550-555, Dec 2008.
- [62] L. Wang, Y. Hashimoto, C. Y. Tsao, J. J. Valdes, and W. E. Bentley, "Cyclic AMP (cAMP) and cAMP receptor protein influence both synthesis and uptake of extracellular autoinducer 2 in *Escherichia coli*," *Journal Of Bacteriology*, vol. 187, pp. 2066-2076, Mar 2005.
- [63] K. B. Xavier and B. L. Bassler, "Regulation of uptake and processing of the quorum-sensing autoinducer AI-2 in *Escherichia coli*," *Journal Of Bacteriology*, vol. 187, pp. 238-248, Jan 2005.
- [64] Y. Irie and M. Parsek, "Quorum sensing and microbial biofilms," in *Bacterial Biofilms*, ed: Springer, 2008, pp. 67-84.
- [65] J. Pan and D. Ren, "Quorum sensing inhibitors: a patent overview," *Expert Opinion on Therapeutic Patents*, vol. 19, pp. 1581-1601, Nov 2009.
- [66] K. M. Duan, C. Dammel, J. Stein, H. Rabin, and M. G. Surette, "Modulation of *Pseudomonas aeruginosa* gene expression by host microflora through interspecies communication," *Molecular Microbiology*, vol. 50, pp. 1477-1491, Dec 2003.
- [67] M. Guo, S. Gamby, Y. Zheng, and H. Sintim, "Small Molecule Inhibitors of AI-2 Signaling in Bacteria: State-of-the-Art and Future Perspectives for Anti-Quorum Sensing Agents," *International Journal of Molecular Sciences*, vol. 14, pp. 17694-17728, 2013.
- [68] T. B. Rasmussen and M. Givskov, "Quorum sensing inhibitors: a bargain of effects," *Microbiology*, vol. 152, pp. 895-904, Apr 2006.
- [69] T. B. Rasmussen and M. Givskov, "Quorum-sensing inhibitors as anti-pathogenic drugs," *International Journal of Medical Microbiology*, vol. 296, pp. 149-161, Apr 2006.
- [70] N. Wellman, S. M. Fortun, and B. R. McLeod, "Bacterial biofilms and the bioelectric effect," *Antimicrobial Agents and Chemotherapy*, vol. 40, pp. 2012-2014, 1996.
- [71] J. W. Costerton, B. Ellis, K. Lam, F. Johnson, and A. E. Khoury, "Mechanism of electrical enhancement of efficacy of antibiotics in

- killing biofilm bacteria," *Antimicrobial Agents and Chemotherapy*, vol. 38, pp. 2803-2809, Dec. 1994.
- [72] P. Stoodley, D. deBeer, and H. M. Lappin-Scott, "Influence of electric fields and pH on biofilm structure as related to the bioelectric effect," *Antimicrobial Agents and Chemotherapy*, vol. 41, pp. 1876-1879, Sep. 1997.
- [73] A. E. Khoury, K. Lam, B. Ellis, and J. W. Costerton, "Prevention and Control of Bacterial Infections Associated with Medical Devices," *ASAIO Journal*, vol. 38, pp. M174-M178, 1992.
- [74] P. S. Stewart, W. Wattanakaroon, L. Goodrum, S. M. Fortun, and B. R. McLeod, "Electrolytic Generation of Oxygen Partially Explains Electrical Enhancement of Tobramycin Efficacy against *Pseudomonas aeruginosa* Biofilm," *Antimicrobial Agents and Chemotherapy*, vol. 43, pp. 292-296, 1999.
- [75] Y. Kim, H. Ben-Yoav, H. Wu, D. Quan, K. Carter, M. Meyer, W. Bentley, and R. Ghodssi, "An Enhanced Bacterial Biofilm Treatment Using Superpositioned Electric Field," in *Proc. International Conference on Microtechnologies in Medicine and Biology 2013*, pp. 102-103.
- [76] Y. W. Kim, M. P. Mosteller, M. T. Meyer, H. Ben-Yoav, W. E. Bentley, and R. Ghodssi, "Microfluidic Biofilm Observation, Analysis, and Treatment (Micro-BOAT) Platform," in *Solid-State Sensors, Actuators and Microsystems Workshop (Hilton Head Workshop 2012)*, Hilton Head, SC, USA, 2012, pp. 233-236.
- [77] G. D. Geske, R. J. Wezeman, A. P. Siegel, and H. E. Blackwell, "Small molecule inhibitors of bacterial quorum sensing and biofilm formation," *Journal of the American Chemical Society*, vol. 127, pp. 12762-12763, Sep 21 2005.
- [78] L. M. Junker and J. Clardy, "High-Throughput Screens for Small-Molecule Inhibitors of *Pseudomonas aeruginosa* Biofilm Development," *Antimicrobial Agents and Chemotherapy*, vol. 51, pp. 3582-3590, Oct. 2007.
- [79] G. Brackman, P. Cos, L. Maes, H. J. Nelis, and T. Coenye, "Quorum sensing inhibitors increase the susceptibility of bacterial biofilms to antibiotics in vitro and in vivo," *Antimicrobial Agents and Chemotherapy*, vol. 55, pp. 2655-2661, Jun 2011.
- [80] L. D. Christensen, M. van Gennip, T. H. Jakobsen, M. Alhede, H. P. Hougen, N. Hoiby, T. Bjarnsholt, and M. Givskov, "Synergistic antibacterial efficacy of early combination treatment with tobramycin and quorum-sensing inhibitors against *Pseudomonas aeruginosa* in an

- intraperitoneal foreign-body infection mouse model," *Journal of Antimicrobial Chemotherapy*, vol. 67, pp. 1198-1206, May 2012.
- [81] C. A. Lowery, T. Abe, J. Park, L. M. Eubanks, D. Sawada, G. F. Kaufmann, and K. D. Janda, "Revisiting AI-2 quorum sensing inhibitors: direct comparison of alkyl-DPD analogues and a natural product fimbrolide," *Journal of the American Chemical Society*, vol. 131, pp. 15584-15585, Nov 4 2009.
- [82] C. A. Lowery, J. Park, G. F. Kaufmann, and K. D. Janda, "An unexpected switch in the modulation of AI-2-based quorum sensing discovered through synthetic 4,5-dihydroxy-2,3-pentanedione analogues," *Journal of the American Chemical Society*, vol. 130, pp. 9200-9201, Jul 23 2008.
- [83] J. A. Smith, J. Wang, S. M. Nguyen-Mau, V. Lee, and H. O. Sintim, "Biological screening of a diverse set of AI-2 analogues in *Vibrio harveyi* suggests that receptors which are involved in synergistic agonism of AI-2 and analogues are promiscuous," *Chemical Communications*, pp. 7033-7035, Dec 7 2009.
- [84] V. Roy, J. A. I. Smith, J. Wang, J. E. Stewart, W. E. Bentley, and H. O. Sintim, "Synthetic Analogs Tailor Native AI-2 Signaling Across Bacterial Species," *Journal of the American Chemical Society*, vol. 132, pp. 11141-11150, Aug 18 2010.
- [85] S. Gamby, V. Roy, M. Guo, J. A. Smith, J. Wang, J. E. Stewart, X. Wang, W. E. Bentley, and H. O. Sintim, "Altering the Communication Networks of Multispecies Microbial Systems Using a Diverse Toolbox of AI-2 Analogues," *ACS Chemical Biology*, vol. 7, pp. 1023-1030, Jun 15 2012.
- [86] C. Sternberg and T. Tolker-Nielsen, "Growing and analyzing biofilms in flow cells," in *Current Protocols in Microbiology*, ed: John Wiley & Sons, Inc., 2006.
- [87] B. Pitts, M. A. Hamilton, N. Zilver, and P. S. Stewart, "A microtiter-plate screening method for biofilm disinfection and removal," *Journal of Microbiological Methods*, vol. 54, pp. 269-276, 2003.
- [88] E. Peeters, H. J. Nelis, and T. Coenye, "Comparison of multiple methods for quantification of microbial biofilms grown in microtiter plates," *Journal of Microbiological Methods*, vol. 72, pp. 157-165, 2008.
- [89] J. H. Merritt, D. E. Kadouri, and G. A. O'Toole, "Growing and Analyzing Static Biofilms," in *Current Protocols in Microbiology*, ed: John Wiley & Sons, Inc., 2005.

- [90] K. L. Swope and M. C. Flicklinger, "The use of confocal scanning laser microscopy and other tools to characterize *Escherichia coli* in a high-cell-density synthetic biofilm," *Biotechnology and Bioengineering*, vol. 52, pp. 340-356, Oct 1996.
- [91] D. Andes, J. Nett, P. Oschel, R. Albrecht, K. Marchillo, and A. Pitula, "Development and characterization of an in vivo central venous catheter *Candida albicans* biofilm model," *Infection and Immunity*, vol. 72, pp. 6023-6031, Oct 2004.
- [92] L. Ganderton, J. Chawla, C. Winters, J. Wimpenny, and D. Stickler, "Scanning Electron-Microscopy Of Bacterial Biofilms On Indwelling Bladder Catheters," *European Journal Of Clinical Microbiology & Infectious Diseases*, vol. 11, pp. 789-796, Sep 1992.
- [93] R. J. Palmer Jr and C. Sternberg, "Modern microscopy in biofilm research: confocal microscopy and other approaches," *Current Opinion in Biotechnology*, vol. 10, pp. 263-268, 1999.
- [94] D. G. Allison and M. A. Sattenstall, "The influence of green fluorescent protein incorporation on bacterial physiology: a note of caution," *Journal of Applied Microbiology*, vol. 103, pp. 318-324, 2007.
- [95] A. Heydorn, A. T. Nielsen, M. Hentzer, C. Sternberg, M. Givskov, B. K. Ersboll, and S. Molin, "Quantification of biofilm structures by the novel computer program COMSTAT," *Microbiology*, vol. 146 (Pt 10), pp. 2395-2407, Oct 2000.
- [96] A. Bridier, T. Meylheuc, and R. Briandet, "Realistic representation of *Bacillus subtilis* biofilms architecture using combined microscopy (CLSM, ESEM and FESEM)," *Micron*, vol. 48, pp. 65-69, 2013.
- [97] P. Janknecht and L. Melo, "Online Biofilm Monitoring," *Reviews in Environmental Science and Biotechnology*, vol. 2, pp. 269-283, June 1 2003.
- [98] H. Ben-Yoav, A. Freeman, M. Sternheim, and Y. Shacham-Diamand, "An electrochemical impedance model for integrated bacterial biofilms," *Electrochimica Acta*, vol. 56, pp. 7780-7786, 2011.
- [99] J. Paredes, S. Becerro, F. Arizti, A. Aguinaga, J. L. Del Pozo, and S. Arana, "Interdigitated microelectrode biosensor for bacterial biofilm growth monitoring by impedance spectroscopy technique in 96-well microtiter plates," *Sensors and Actuators B: Chemical*, vol. 178, pp. 663-670, 2013.
- [100] S. B. Prakash and P. Abshire, "On-chip capacitance sensing for cell monitoring applications," *Sensors Journal, IEEE*, vol. 7, pp. 440-447, 2007.

- [101] J. Klahre and H. C. Flemming, "Monitoring of biofouling in papermill process waters," *Water Research*, vol. 34, pp. 3657-3665, 2000.
- [102] A. Tamachkiarow and H. Flemming, "On-line monitoring of biofilm formation in a brewery water pipeline system with a fibre optical device," *Water Science & Technology*, vol. 47, pp. 19-24, 2003.
- [103] G. S. Jing, A. Polaczyk, D. B. Oerther, and I. Papautsky, "Development of a microfluidic biosensor for detection of environmental mycobacteria," *Sensors And Actuators B-Chemical*, vol. 123, pp. 614-621, Apr 2007.
- [104] L. Richter, C. Stepper, A. Mak, A. Reinthaler, R. Heer, M. Kast, H. Bruckl, and P. Ertl, "Development of a microfluidic biochip for online monitoring of fungal biofilm dynamics," *Lab on a Chip*, vol. 7, pp. 1723-1731, 2007.
- [105] J. Khandurina, T. E. McKnight, S. C. Jacobson, L. C. Waters, R. S. Foote, and J. M. Ramsey, "Integrated system for rapid PCR-based DNA analysis in microfluidic devices," *Analytical Chemistry*, vol. 72, pp. 2995-3000, Jul 2000.
- [106] T. Yamamoto, T. Nojima, and T. Fujii, "PDMS-glass hybrid microreactor array with embedded temperature control device. Application to cell-free protein synthesis," *Lab on a Chip*, vol. 2, pp. 197-202, 2002.
- [107] S. Elizabeth Hulme, S. S. Shevkoplyas, and G. M. Whitesides, "Incorporation of prefabricated screw, pneumatic, and solenoid valves into microfluidic devices," *Lab on a Chip*, vol. 9, pp. 79-86, 2009.
- [108] J. Melin and S. R. Quake, "Microfluidic large-scale integration: the evolution of design rules for biological automation," *Annual Review of Biophysics and Biomolecular Structure*, vol. 36, pp. 213-231, 2007.
- [109] T. Thorsen, S. J. Maerkl, and S. R. Quake, "Microfluidic large-scale integration," *Science*, vol. 298, pp. 580-584, Oct 2002.
- [110] V. Studer, G. Hang, A. Pandolfi, M. Ortiz, W. F. Anderson, and S. R. Quake, "Scaling properties of a low-actuation pressure microfluidic valve," *Journal of Applied Physics*, vol. 95, pp. 393-398, Jan 2004.
- [111] J. Kim, M. Hegde, S. H. Kim, T. K. Wood, and A. Jayaraman, "A microfluidic device for high throughput bacterial biofilm studies," *Lab on a Chip*, vol. 12, pp. 1157-1163, 2012.
- [112] E. Berkenpas, P. Millard, and M. P. da Cunha, "Detection of *Escherichia coli* O157 : H7 with langasite pure shear horizontal surface acoustic wave sensors," *Biosensors & Bioelectronics*, vol. 21, pp. 2255-2262, Jun 15 2006.

- [113] Y. W. Kim, S. E. Sardari, M. T. Meyer, A. A. Iliadis, H. C. Wu, W. E. Bentley, and R. Ghodssi, "An ALD aluminum oxide passivated Surface Acoustic Wave sensor for early biofilm detection," *Sensors and Actuators B: Chemical*, vol. 163, pp. 136-145, 2012.
- [114] M. Nordström, S. Keller, M. Lillemose, A. Johansson, S. Dohn, D. Haefliger, G. Blagoi, M. Havsteen-Jakobsen, and A. Boisen, "SU-8 cantilevers for bio/chemical sensing; fabrication, characterisation and development of novel read-out methods," *Sensors*, vol. 8, pp. 1595-1612, 2008.
- [115] S. T. Koev, W. E. Bentley, and R. Ghodssi, "Interferometric readout of multiple cantilever sensors in liquid samples," *Sensors and Actuators B: Chemical*, vol. 146, pp. 245-252, 2010.
- [116] J. Kim, H.-S. Kim, S. Han, J.-Y. Lee, J.-E. Oh, S. Chung, and H.-D. Park, "Hydrodynamic effects on bacterial biofilm development in a microfluidic environment," *Lab on a Chip*, vol. 13, pp. 1846-1849, 2013.
- [117] A. P. Mosier, A. E. Kaloyeros, and N. C. Cady, "A novel microfluidic device for the in situ optical and mechanical analysis of bacterial biofilms," *Journal of Microbiological Methods*, vol. 91, pp. 198-204, Oct 2012.
- [118] M. T. Meyer, V. Roy, W. E. Bentley, and R. Ghodssi, "Development and validation of a microfluidic reactor for biofilm monitoring via optical methods," *Journal Of Micromechanics And Microengineering*, vol. 21, May 2011.
- [119] V. Roy, M. Meyer, J. I. Smith, S. Gamby, H. Sintim, R. Ghodssi, and W. Bentley, "AI-2 analogs and antibiotics: a synergistic approach to reduce bacterial biofilms," *Applied Microbiology and Biotechnology*, vol. 97, pp. 2627-2638, Mar 1 2013.
- [120] S. H. Hong, M. Hegde, J. Kim, X. Wang, A. Jayaraman, and T. K. Wood, "Synthetic quorum-sensing circuit to control consortial biofilm formation and dispersal in a microfluidic device," *Nature Communications*, vol. 3, p. 613, 2012.
- [121] K. P. Kim, Y. G. Kim, C. H. Choi, H. E. Kim, S. H. Lee, W. S. Chang, and C. S. Lee, "In situ monitoring of antibiotic susceptibility of bacterial biofilms in a microfluidic device," *Lab on a Chip*, vol. 10, pp. 3296-3299, Dec 7 2010.
- [122] J. Kim, H. D. Park, and S. Chung, "Microfluidic Approaches to Bacterial Biofilm Formation," *Molecules*, vol. 17, pp. 9818-9834, Aug 2012.

- [123] M. Skolimowski, M. W. Nielsen, J. Emneus, S. Molin, R. Taboryski, C. Sternberg, M. Dufva, and O. Geschke, "Microfluidic dissolved oxygen gradient generator biochip as a useful tool in bacterial biofilm studies," *Lab on a Chip*, vol. 10, pp. 2162-2169, 2010.
- [124] J. Kim, M. Hegde, and A. Jayaraman, "Co-culture of epithelial cells and bacteria for investigating host-pathogen interactions," *Lab on a Chip*, vol. 10, pp. 43-50, Jan 7 2010.
- [125] J. El-Ali, P. K. Sorger, and K. F. Jensen, "Cells on chips," *Nature*, vol. 442, pp. 403-411, Jul 2006.
- [126] M. Mosteller, "An Optical Density Detection Platform with Integrated Microfluidics for In Situ Growth, Monitoring, and Treatment of Bacterial Biofilms," Master's Thesis, Systems Engineering, University of Maryland, College Park, MD, 2012.
- [127] S. R. Gallagher and P. R. Desjardins, "Quantitation of DNA and RNA with absorption and fluorescence spectroscopy," *Current Protocols in Molecular Biology*, pp. A-3D.
- [128] M. P. DeLisa, J. J. Valdes, and W. E. Bentley, "Mapping stress-induced changes in autoinducer AI-2 production in chemostat-cultivated *Escherichia coli* K-12," *Journal of Bacteriology*, vol. 183, pp. 2918-2928, May 2001.
- [129] S. Nakamura, Y. Higashiyama, K. Izumikawa, M. Seki, H. Kakeya, Y. Yamamoto, K. Yanagihara, Y. Miyazaki, Y. Mizuta, and S. Kohno, "The roles of the quorum-sensing system in the release of extracellular DNA, lipopolysaccharide, and membrane vesicles from *Pseudomonas aeruginosa*," *Japanese Journal of Infectious Diseases*, vol. 61, pp. 375-378, Sep 2008.
- [130] V. Roy, R. Fernandes, C.-Y. Tsao, and W. E. Bentley, "Cross Species Quorum Quenching Using a Native AI-2 Processing Enzyme," *ACS Chem Biol*, vol. 5, pp. 223-232, Feb 19 2009.
- [131] M. H. Zwietering, I. Jongenburger, F. M. Rombouts, and K. van 't Riet, "Modeling of the Bacterial Growth Curve," *Applied and Environmental Microbiology*, vol. 56, pp. 1875-1881, June 1, 1990
- [132] J. P. Holman, "Experimental Methods for Engineers," ed New York: McGraw-Hill, 1994, pp. 49-56.
- [133] H. O. Sintim, J. A. I. Smith, J. Wang, S. Nakayama, and L. Yan, "Paradigm shift in discovering next-generation anti-infective agents: targeting quorum sensing, c-di-GMP signaling and biofilm formation in bacteria with small molecules," *Future Medicinal Chemistry*, vol. 2, pp. 1005-1035, June 1 2010.

- [134] M. A. Hamon and B. A. Lazazzera, "The sporulation transcription factor Spo0A is required for biofilm development in *Bacillus subtilis*," *Molecular Microbiology*, vol. 42, pp. 1199-1209, Dec 2001.
- [135] S. W. Churchill and R. Usagi, "A general expression for the correlation of rates of transfer and other phenomena," *AIChE J.*, vol. 18, pp. 1121-1128, 1972.
- [136] P. K. Singh, A. L. Schaefer, M. R. Parsek, T. O. Moninger, M. J. Welsh, and E. P. Greenberg, "Quorum-sensing signals indicate that cystic fibrosis lungs are infected with bacterial biofilms," *Nature*, vol. 407, pp. 762-764, Oct 12 2000.
- [137] S. L. Mawer and D. Greenwood, "Specific and Nonspecific Resistance to Aminoglycosides in *Escherichia-Coli*," *Journal of Clinical Pathology*, vol. 31, pp. 12-15, 1978.
- [138] J. L. Kadurugamuwa, A. J. Clarke, and T. J. Beveridge, "Surface action of gentamicin on *Pseudomonas aeruginosa*," *Journal of Bacteriology*, vol. 175, pp. 5798-5805, Sep 1993.
- [139] J. C. Nickel, I. Ruseska, J. B. Wright, and J. W. Costerton, "Tobramycin Resistance of *Pseudomonas-Aeruginosa* Cells Growing as a Biofilm on Urinary Catheter Material," *Antimicrobial Agents and Chemotherapy*, vol. 27, pp. 619-624, 1985.
- [140] M. Berney, F. Hammes, F. Bosshard, H.-U. Weilenmann, and T. Egli, "Assessment and Interpretation of Bacterial Viability by Using the LIVE/DEAD BacLight Kit in Combination with Flow Cytometry," *Applied and Environmental Microbiology*, vol. 73, pp. 3283-3290, May 15, 2007 2007.
- [141] B. L. Roth, M. Poot, S. T. Yue, and P. J. Millard, "Bacterial viability and antibiotic susceptibility testing with SYTOX green nucleic acid stain," *Applied and Environmental Microbiology*, vol. 63, pp. 2421-31, June 1, 1997 1997.
- [142] M. A. Swartz and M. E. Fleury, "Interstitial flow and its effects in soft tissues," *Annual Review of Biomedical Engineering*, vol. 9, pp. 229-256, 2007.
- [143] A. Vertes, V. Hitchins, and K. S. Phillips, "Analytical Challenges of Microbial Biofilms on Medical Devices," *Analytical Chemistry*, vol. 84, pp. 3858-3866, May 2012.
- [144] A. Al-Ahmad, A. Wunder, T. M. Auschill, M. Follo, G. Braun, E. Hellwig, and N. B. Arweiler, "The in vivo dynamics of *Streptococcus* spp., *Actinomyces naeslundii*, *Fusobacterium nucleatum* and *Veillonella* spp. in dental plaque biofilm as analysed by five-colour

- multiplex fluorescence in situ hybridization," *Journal of Medical Microbiology*, vol. 56, pp. 681-687, May 2007.
- [145] L. Ganderton, J. Chawla, C. Winters, J. Wimpenny, and D. Stickler, "Scanning electron microscopy of bacterial biofilms on indwelling bladder catheters," *European Journal of Clinical Microbiology and Infectious Diseases*, vol. 11, pp. 789-796, Sep 1992.
- [146] J. A. Schaber, W. J. Triffo, S. J. Suh, J. W. Oliver, M. C. Hastert, J. A. Griswold, M. Auer, A. N. Hamood, and K. P. Rumbaugh, "*Pseudomonas aeruginosa* forms biofilms in acute infection independent of cell-to-cell signaling," *Infection and Immunity*, vol. 75, pp. 3715-3721, Aug 2007.
- [147] K. P. Rumbaugh, J. A. Griswold, B. H. Iglewski, and A. N. Hamood, "Contribution of quorum sensing to the virulence of *Pseudomonas aeruginosa* in burn wound infections," *Infection and Immunity*, vol. 67, pp. 5854-5862, Nov 1999.
- [148] Y. Kim and T. K. Wood, "Toxins Hha and CspD and small RNA regulator Hfq are involved in persister cell formation through MqsR in *Escherichia coli*," *Biochemical and Biophysical Research Communications*, vol. 391, pp. 209-213, 2010.
- [149] J. Pan, A. A. Bahar, H. Syed, and D. Ren, "Reverting Antibiotic Tolerance of *Pseudomonas aeruginosa* PAO1 Persister Cells by (Z)-4-bromo-5-(bromomethylene)-3-methylfuran-2(5H)-one," *PLoS ONE*, vol. 7, p. e45778, 2012.
- [150] G. Sezonov, D. Joseleau-Petit, and R. D'Ari, "*Escherichia coli* Physiology in Luria-Bertani Broth," *Journal of Bacteriology*, vol. 189, pp. 8746-8749, December 1, 2007 2007.
- [151] H. W. Blanch and D. S. Clark, "Transport Processes," in *Biochemical Engineering*, ed New York: CRC Press, 1997, pp. 358-360.
- [152] T. C. Merkel, V. I. Bondar, K. Nagai, B. D. Freeman, and I. Pinnau, "Gas sorption, diffusion, and permeation in poly(dimethylsiloxane)," *Journal of Polymer Science Part B: Polymer Physics*, vol. 38, pp. 415-434, 2000.
- [153] M. Zahorodny-Burke, B. Nearingburg, and A. L. Elias, "Finite element analysis of oxygen transport in microfluidic cell culture devices with varying channel architectures, perfusion rates, and materials," *Chemical Engineering Science*, vol. 66, pp. 6244-6253, 2011.
- [154] T. Saito, C.-C. Wu, H. Shiku, T. Yasukawa, M. Yokoo, T. Ito-Sasaki, H. Abe, H. Hoshi, and T. Matsue, "Oxygen consumption of cell suspension in a poly(dimethylsiloxane) (PDMS) microchannel

- estimated by scanning electrochemical microscopy," *Analyst*, vol. 131, pp. 1006-1011, 2006.
- [155] S. Hansen, I. Hariskos, B. Luchterhand, and J. Buchs, "Development of a modified Respiration Activity Monitoring System for accurate and highly resolved measurement of respiration activity in shake flask fermentations," *Journal of Biological Engineering*, vol. 6, p. 11, 2012.
- [156] S. P. Forry and L. E. Locascio, "On-chip CO₂ control for microfluidic cell culture," *Lab on a Chip*, vol. 11, pp. 4041-4046, 2011.
- [157] P. H. Dykstra, "A Microfluidic Programmable Array for Label-free Detection of Biomolecules," Ph.D. Dissertation, Electrical and Computer Engineering, University of Maryland, College Park, MD, 2011.
- [158] R. Allen, M. Foster, and Y. T. Yen, "Deep U.V. Hardening of Positive Photoresist Patterns," *Journal of The Electrochemical Society*, vol. 129, pp. 1379-1381, June 1 1982.
- [159] M. Hatzakis, B. J. Canavello, and J. M. Shaw, "Single-step optical lift-off process," *IBM Journal of Research and Development*, vol. 24, pp. 452-460, 1980.
- [160] C. Chung and M. Allen, "Uncrosslinked SU-8 as a sacrificial material," *Journal Of Micromechanics And Microengineering*, vol. 15, p. N1, 2005.
- [161] D. A. Chang-Yen, R. K. Eich, and B. K. Gale, "A monolithic PDMS waveguide system fabricated using soft-lithography techniques," *Journal of Lightwave Technology*, vol. 23, pp. 2088-2093, 2005.
- [162] M. A. Unger, H.-P. Chou, T. Thorsen, A. Scherer, and S. R. Quake, "Monolithic Microfabricated Valves and Pumps by Multilayer Soft Lithography," *Science*, vol. 288, pp. 113-116, April 7 2000.
- [163] M. Knez, K. Niesch, and L. Niinistö, "Synthesis and surface engineering of complex nanostructures by atomic layer deposition," *Advanced Materials*, vol. 19, pp. 3425-3438, Nov 5 2007.
- [164] S. M. George, "Atomic Layer Deposition: An Overview," *Chemical Reviews*, vol. 110, pp. 111-131, Jan 2010.
- [165] J.-H. Lee, H. Wang, J. B. Kaplan, and W. Y. Lee, "Microfluidic Approach to Create Three-Dimensional Tissue Models for Biofilm-Related Infection of Orthopaedic Implants," *Tissue Engineering Part C-Methods*, vol. 17, pp. 39-48, Jan 2011.
- [166] W. J. Polacheck, R. Li, S. G. Uzel, and R. D. Kamm, "Microfluidic platforms for mechanobiology," *Lab on a Chip*, vol. 13, pp. 2252-2267, Jun 21 2013.

- [167] H. Ben-Yoav, P. H. Dykstra, W. E. Bentley, and R. Ghodssi, "A microfluidic-based electrochemical biochip for label-free diffusion-restricted DNA hybridization analysis," *Biosensors & Bioelectronics*, vol. 38, pp. 114-120, Oct-Dec 2012.
- [168] C.-X. Liu and J.-W. Choi, "Patterning conductive PDMS nanocomposite in an elastomer using microcontact printing," *Journal Of Micromechanics And Microengineering*, vol. 19, p. 085019, 2009.
- [169] L. Li, S. Molin, L. Yang, and S. Ndoni, "Sodium Dodecyl Sulfate (SDS)-Loaded Nanoporous Polymer as Anti-Biofilm Surface Coating Material," *International Journal of Molecular Sciences*, vol. 14, pp. 3050-3064, Feb 2013.
- [170] F. Pantanella, P. Valenti, T. Natalizi, D. Passeri, and F. Berlutti, "Analytical techniques to study microbial biofilm on abiotic surfaces: pros and cons of the main techniques currently in use," *Annali di igiene : medicina preventiva e di comunita*, vol. 25, pp. 31-42, 2013.
- [171] W.-Y. Wu, X. Zhong, W. Wang, Q. Miao, and J.-J. Zhu, "Flexible PDMS-based three-electrode sensor," *Electrochemistry Communications*, vol. 12, pp. 1600-1604, 2010.
- [172] M. Paranjape, J. Garra, S. Brida, T. Schneider, R. White, and J. Currie, "A PDMS dermal patch for non-intrusive transdermal glucose sensing," *Sensors and Actuators A: Physical*, vol. 104, pp. 195-204, 2003.
- [173] N. Lu, C. Lu, S. Yang, and J. Rogers, "Highly Sensitive Skin-Mountable Strain Gauges Based Entirely on Elastomers," *Advanced Functional Materials*, vol. 22, pp. 4044-4050, 2012.
- [174] A. Reina, H. Son, L. Jiao, B. Fan, M. S. Dresselhaus, Z. Liu, and J. Kong, "Transferring and Identification of Single- and Few-Layer Graphene on Arbitrary Substrates," *The Journal of Physical Chemistry C*, vol. 112, pp. 17741-17744, Nov 2008.
- [175] D. A. Ateya, J. S. Erickson, P. B. Howell, L. R. Hilliard, J. P. Golden, and F. S. Ligler, "The good, the bad, and the tiny: a review of microflow cytometry," *Analytical and Bioanalytical Chemistry*, vol. 391, pp. 1485-1498, Jul 2008.
- [176] B. Purevdorj, J. W. Costerton, and P. Stoodley, "Influence of hydrodynamics and cell signaling on the structure and behavior of *Pseudomonas aeruginosa* biofilms," *Applied and Environmental Microbiology*, vol. 68, pp. 4457-4464, Sep 2002.
- [177] A. Reisner, K. A. Krogfelt, B. M. Klein, E. L. Zechner, and S. Molin, "In vitro biofilm formation of commensal and pathogenic *Escherichia*

coli strains: impact of environmental and genetic factors," *Journal of Bacteriology*, vol. 188, pp. 3572-3581, May 2006.